

Thermal history of the Junggar Alatau  
(SE Kazakhstan, NW China): insights  
from apatite fission track  
thermochronology

Thesis submitted in accordance with the requirements of the University of  
Adelaide for an Honours Degree in Geology

Alexander Otasevic  
October 2018



## **THERMAL HISTORY OF THE JUNGGAR ALATAU (SE KAZAKHSTAN, NW CHINA): INSIGHTS FROM APATITE FISSION TRACK THERMOCHRONOLOGY**

### **RUNNING TITLE**

Thermal history of the Junggar Alatau

### **ABSTRACT**

The Junggar Alatau is located along the border of SE Kazakhstan and NW China, representing the western extent of the northern Chinese Tian Shan within the Central Asian Orogenic Belt. This study applies apatite U–Pb and low temperature thermochronology to constrain the exhumation history of the Junggar Alatau through the Meso-Cenozoic period. Apatite U–Pb results record Ordovician–Permian ages, reflecting the post-magmatic cooling of granitoids that intruded during the progressive closure of the Palaeo-Asian Ocean. Apatite fission track data obtained from Palaeozoic basement and (meta)sedimentary samples record (partial) preservation of post-magmatic cooling ages and suggests at least two subsequent cooling periods during the Late Triassic (~230–210 Ma) and Early Cretaceous (~150–120 Ma). Permian-Triassic cooling signals are preserved in low-relief areas distal to major NW-SE orientated shear zones, reflecting post-magmatic cooling during the Palaeo-Asian Ocean closure and regional exhumation in response to the Qiangtang collision. The Early Cretaceous rapid cooling signal is localised for samples taken along the Central Kazakhstan Fault Zone (CKFZ). The record of younger signals localised in the CKFZ suggests the reactivation of faulting during the Early Cretaceous, which can be linked to a phase of slab-rollback and associated extension in the distant Tethys Ocean. Cretaceous exhumation is thought to have induced rapid cooling in the exhuming footwalls with respect to subsiding hanging walls of the CKFZ. Additionally, few samples from higher relief areas record Late Cretaceous cooling, although there is no consensus on the cause. The results obtained in this study indicate that the extent of Cenozoic exhumation within Central Asia has not propagated to the Junggar Alatau. Results obtained in this work fit with those obtained from samples along other major NW-SE orientated shear zones in the vicinity of the study area, improving the overall understanding of strain propagation through Central Asia.

### **KEYWORDS**

Junggar Alatau, Central Asia, Mesozoic, thermal history, AFT, thermochronology, fault reactivation

## TABLE OF CONTENTS

Abstract .....	i
List of figures and tables .....	2
1. Introduction.....	3
2. Geological setting.....	5
3. Methods .....	10
3.1. Laboratory processing .....	10
3.2. Apatite fission track and U–Pb method.....	10
3.3. Apatite fission track analysis .....	11
3.4. Apatite U–Pb analysis .....	12
3.5. Low-temperature thermal history modelling .....	12
4. Results .....	14
4.1. Samples.....	14
4.2. Apatite fission track results.....	17
4.2.1. Data accuracy .....	18
4.2.2. Group 1 .....	18
4.2.3. Group 2 .....	21
4.2.4. Group 3 .....	24
4.2.5. Pooled study area.....	26
4.3. Apatite U–Pb results.....	27
4.3.1. Data accuracy .....	29
4.3.2. Tera-Wasserburg Concordia plots.....	30
4.4. Thermal history modelling.....	34
4.4.1. Group 1 .....	34
4.4.2. Group 2 .....	35
4.4.3. Group 3 .....	36
5. Discussion.....	38
5.1. AU–Pb age interpretations.....	38
5.2. AFT age interpretations and comparison with AU–Pb age constraints .....	39
5.3. Boomerang plot.....	41
5.4. Geographical distribution of cooling events and cooling mechanism .....	43
5.5. Geographical age disparities .....	45
5.5.1. DZ-15 and DZ-16.....	45
5.5.2. DZ-22 and DZ-23.....	46
5.5.3. DZ-06 and DZ-07.....	46
5.6. Summary for the thermo-tectonic history of the Junggar Alatau.....	47

5.6.1. Early Permian – Early Triassic .....	47
5.6.2. Late Triassic – Early Jurassic reactivation .....	48
5.6.3. Latest Jurassic – Early Cretaceous reactivation .....	49
5.6.4. Late Cretaceous reactivation.....	49
6. Conclusions.....	50
7. Acknowledgments.....	51
8. References.....	51
9. Appendix A: Extended methods .....	56
10. Appendix B: AFT data table .....	61
11. Appendix C: AU–Pb data table.....	79

## LIST OF FIGURES AND TABLES

Figure 1 – Topographic map of the Tian Shan and Junggar Alatau study area .....	5
Figure 2 – Topographic map of the Junggar Alatau and sample groups.....	9
Figure 3 – Topographic map of the Junggar Alatau and apatite fission track results.....	16
Figure 4 – Weighted average apatite fission track age for Durango apatite. ....	18
Figure 5 – Radial plots for Group 1 .....	21
Figure 6 – Radial plots for Group 2 .....	24
Figure 7 – Radial plots for Group 3 .....	26
Figure 8 – Radial plot for all samples from the Junggar Alatau.....	27
Figure 9 – Weighted average apatite U–Pb ages for Durango apatite and McClure apatite ....	29
Figure 10 – Tera-Wasserburg Concordia plots for all Junggar Alatau samples.....	33
Figure 11 – Combined thermal history model for Group 1 .....	35
Figure 12 – Combined thermal history model for Group 2.....	36
Figure 13 – Combined thermal history model for Group 3.....	38
Figure 14 – Apatite U–Pb vs apatite fission track plot .....	41
Figure 15 – ‘Boomerang plot’ based on the relationship between mean track length and apatite fission track age .....	43
Figure 16 – Radial plots for DZ-15 and DZ-16 age disparity .....	45
Figure 17 – Radial plots for DZ-22 and DZ-23 age disparity .....	46
Figure 18 – Radial plots for DZ-06 and DZ-07 age disparity .....	47
Table 1 – Analytical details for the LA-ICP-MS.....	13
Table 2 – Sample locations and lithology details .....	14
Table 3 – Summary of apatite fission track results .....	17
Table 4 – Summary of apatite U–Pb results .....	28

## 1. INTRODUCTION

The Junggar Alatau represents the western extent of the northern Chinese Tian Shan that is located within the larger Central Asian Orogenic Belt (CAOB) (Figure 1). The CAOB represents a huge accretionary orogen that was formed during the Palaeozoic (Choulet et al., 2012; Windley, Alexeiev, Xiao, Kroener, & Badarach, 2007) and became reactivated in response to distant tectonic activity during the Meso-Cenozoic (e.g. Glorie & De Grave, 2016). Unlike the extensively studied Tian Shan, thermochronological data for the extremities of the mountain ranges are often lacking such as for the Junggar Alatau (Figure 1). Studying these areas is important as it is likely that they record less Cenozoic deformation overprint, thus more likely preserving an archive of Mesozoic thermo-tectonic events. Previous studies across Central Asia have shown that major NW-SE orientated shear zones (Talas-Fergana and Irtysh) record thermal histories of rapid cooling during the Cretaceous (e.g. Glorie et al., 2012; Nachtergael et al., 2018). This study tests whether the shear zone that dissects the Junggar Alatau, and which runs parallel to the Irtysh and Talas-Fergana shear zones, records a similar history of Cretaceous deformation (Figure 1). If the latter is the case, Cretaceous fault reactivation can be regarded as a more widespread event than previously anticipated (e.g. Glorie & De Grave, 2016).

Throughout the Meso-Cenozoic period, Central Asia has experienced intracontinental deformation associated with convergent (e.g. Bullen, Burbank, Garver, & Abdurakhmatov, 2001; De Grave, Buslov, & Van den Haute, 2007; Dumitru et al., 2001; Gillespie et al., 2017b; Jolivet et al., 2010; Sobel, Chen, & Heermance, 2006) and potentially extensional tectonic events in the distant Tethys (Zahirovic et al., 2016) and Mongol-Okhotsk (Metelkin, Vernikovsky, Kazansky, & Wingate, 2010) oceans. Stress-fields as a result of these distal tectonic events propagated through the inherited Palaeozoic structures of the CAOB resulting in the progressive and punctuated exhumation and mountain building events that shaped the

Central Asian landscape that is seen today (Glorie et al., 2011; Jolivet et al., 2010; Macaulay, Sobel, Mikolaichuk, Kohn, & Stuart, 2014).

Located at the intersection of the Tian Shan and Altai Sayan, the Junggar Alatau is a key region in linking the deformation histories of the orogens. Although thermochronological data in the Junggar Alatau is largely lacking, limited previous work by De Pelsmaeker et al. (2015) in the core of the Junggar Alatau, revealed mostly Late Cretaceous apatite fission-track (AFT) cooling ages. In comparison to previous studies, this work uses samples taken in vicinity to the main shear zone that dissects the study area (the Central Kazakhstan Fault Zone or CKFZ), aiming to constrain the timing of fault reactivation in relation to the regional exhumation (Figure 2). With the use of the newly collected data from the Junggar Alatau, integrated with the published data, a more complete picture of the reactivation history of the Junggar Alatau in response to distal tectonic events at the Mesozoic southern Eurasian plate margin can be created. Furthermore, understanding whether the region has experienced Cenozoic deformation or preserves Mesozoic deformation is key to understanding the propagation of strain through crustal architecture of Central Asia.

The overall aim of this study is to constrain the low-temperature cooling history of the Junggar Alatau in relation to deformation of a major fault zone (the CKFZ) and to correlate the cooling events with the Meso-Cenozoic tectonic history at the southern Eurasian margin that may have induced intracontinental reactivation. Thermochronological data are presented for twenty-five samples, sixteen from SE Kazakhstan and nine from NW China, that were analysed by AFT and apatite U–Pb (AU–Pb) methods. In addition, thermal history models were produced for most samples (with high-quality data) to constrain the cooling history of the Junggar Alatau and to identify the timing of fault reactivation across its structural architecture.

## 2. GEOLOGICAL SETTING

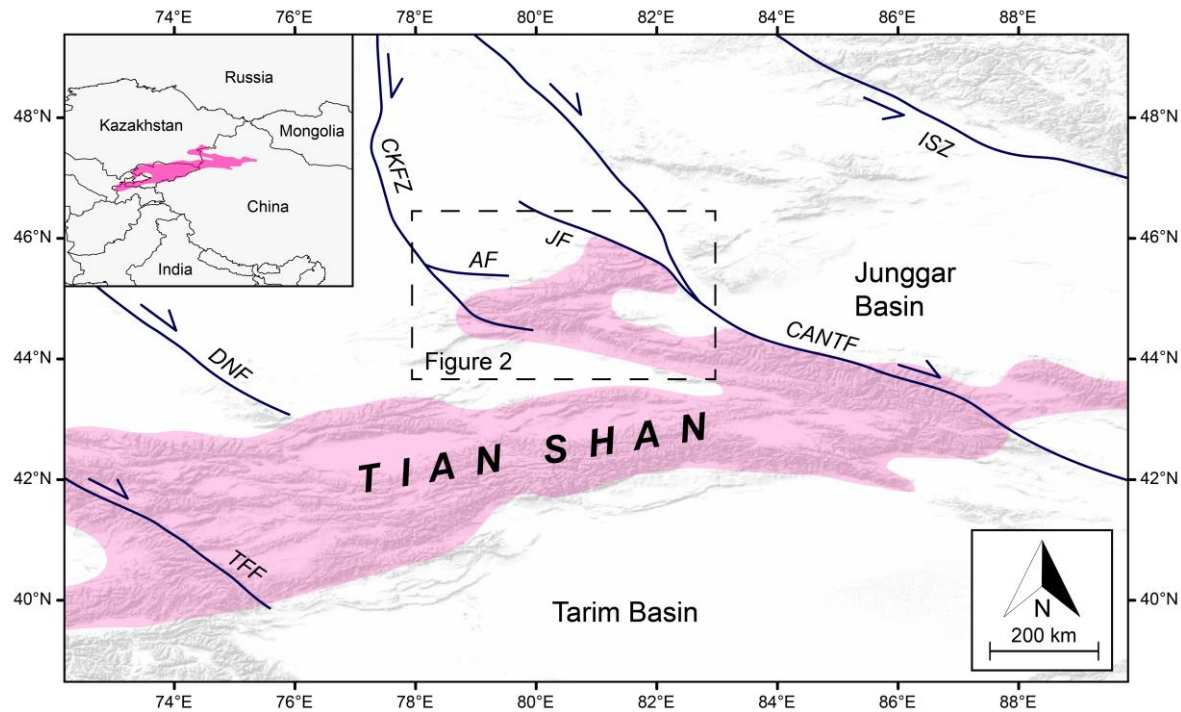


**Figure 1 – Topographic map of the Tian Shan (highlighted in pink) and Junggar Alatau study area (dashed square detailed in Figure 2). Inset of the Tian Shan's location within Central Asia highlighted in pink. Major NW-SE orientated shear zones bisecting Central Asia are indicated by a solid line and an arrow indicating the direction of strike slip movement. Main faults after Choulet et al. (2012), De Pelsmaeker et al. (2015) and Li et al. (2018). AF = Aktas Fault, CANTF = Chingiz-Alakol-North Tian Shan Fault, CKFZ = Central Kazakhstan Fault Zone, DNF = Dzhalaire-Naiman Fault, ISZ = Irtysh Shear Zone, JF = Junggar Fault, TFF = Talas-Fergana Fault.**

The Junggar Alatau is primarily comprised of Palaeozoic granitic plutons and Precambrian to Palaeozoic strata (e.g. Han & Zhao, 2017; Korobkin & Buslov, 2011; Kröner et al., 2017; Li et al., 2018; Petrov, Pospelov, Shokalsky, Tolmacheva, & Kashubin, 2016), forming the southwestern boundary of the Junggar Basin. Lithologies range between granitoids, ophiolites, metamorphosed units and glacial to alluvial strata (e.g. Huang et al., 2017; Li et al., 2018; Zhao & He, 2013; Zhu et al., 2018).

Amalgamation of the CAOB began ca. 1000 Ma with its eventual completion at ca. 250 Ma following the closure of the Palaeo-Asian Ocean (PAO) (De Grave et al., 2007; Windley et al., 2007; Xiao et al., 2017). Palaeozoic structures which formed as a result of the amalgamation process, have experienced episodic reactivation events post-closure of the

PAO (De Grave et al., 2007; Glorie et al., 2011; Nachtergael et al., 2018). Crustal shortening in response to distant Meso-Cenozoic tectonic events along the Eurasian margin is thought to be the main driver for the intracontinental deformation that shaped the mountain ranges that dominate the present-day Central Asian topography (Choulet et al., 2013; De Pelsmaeker et al., 2015; Jolivet et al., 2010).

The reactivation of these inherited Palaeozoic structures throughout the Meso-Cenozoic period have been attributed to the Cimmerian orogeny during the closure of the Palaeo-Tethys Ocean, the Mongol-Okhotsk orogeny during closure of the Mongol-Okhotsk Ocean, and the India-Eurasia collision during the closure of the Neo-Tethys Ocean (e.g. De Pelsmaeker et al., 2015; Gillespie et al., 2017a; Glorie & De Grave, 2016). Punctuated accretion of Gondwana derived Cimmerian blocks led to the Cimmerian orogeny at the Mesozoic southern Eurasian margin. The Cimmerian terranes involved include the Qiangtang Block, which accreted during the Late Triassic-Early Jurassic, the Lhasa Block, which accreted during the latest Jurassic-Early Cretaceous, and the Karakoram Block and Kohistan-Dras island arc, which finalised the Cimmerian orogeny during the Late Cretaceous (e.g. Aitchison, Ali, & Davis, 2007; Nachtergael et al., 2018; Zhang, Zhu, Zheng, Zheng, & Yang, 2016).

In south-eastern Siberia, the diachronous oceanic closure between Mongolia-North China and Siberia resulted in the formation of the Mongol-Okhotsk Orogenic Belt (MOOB) (Jolivet et al., 2009). A ‘scissors-like’ closure model, supported by palaeomagnetic data, has been proposed by Metelkin et al. (2010) suggesting a west-to-east closure of the Mongol-Okhotsk Ocean during the Late Jurassic-Early Cretaceous due to the clockwise rotation of the Siberian craton (Metelkin, Vernikovsky, & Kazansky, 2012).

A recent plate-tectonic reconstruction (Zahirovic et al., 2016) suggests that slab-rollback is thought to have initiated back-arc extension in the Tethys Ocean during the late Early

Cretaceous, swiftly following the Lhasa collision and Mongol-Okhotsk orogeny. Although this period of extension has hitherto received little attention, it is likely that it may have caused fault-reactivation within Central Asia at that time. At the same time, basins along southern Central Asia (e.g. Fergana and Tarim basins) experienced marine incursions of the Para-Tethys Ocean (De Pelsmaeker et al., 2018; Sobel & Dumitru, 1997), further suggesting that parts of Central Asia were subsiding during a period of intracontinental extension. Following the Mesozoic reactivation events, Greater India (Van Hinsbergen et al., 2012) collided along the southern Eurasian margin in the Palaeocene-Eocene resulting in the start of the Cenozoic India-Eurasia collision (e.g. Macaulay et al., 2014; Nachtergael et al., 2018; Sobel & Dumitru, 1997). Associated deformation in the southern CAOB increased from the late Oligocene-Miocene (e.g. Bullen et al., 2001; Hendrix, Dumitru, & Graham, 1994; Sobel et al., 2006). A model proposed by Van Hinsbergen et al. (2012) explains the intensification of deformation by suggesting that the India-Eurasia collision transitioned from a ‘soft’ collision at ~50 Ma to a ‘hard’ collision at ~25 Ma.

Thermochronological results for the Junggar Alatau are scant. Samples in a study by De Pelsmaeker et al. (2015) located within the core of the complex yielded Late Cretaceous AFT ages that are modelled to reflect both rapid and slow cooling at that time. These results were interpreted to be recording the collision of the Lhasa Block along the southern Eurasian margin, but the far-field effects of the MOOB were not discounted. Potential links with back-arc extension in the Tethys were not discussed. Other AFT thermochronological studies at major NW-SE orientated shear zones, bisecting Central Asia, have mostly recorded Mesozoic thermal histories revealing rapid Triassic or Cretaceous cooling. Along the Irtysh and Talas-Fergana shear zones, located to the north and south of the Junggar Alatau respectively, studies by Glorie et al. (2012) and Nachtergael et al. (2018) reported samples yielding Cretaceous AFT ages that were modelled to reflect fast cooling at that time. Results along the

Irtysh shear zone were interpreted as a possible response to the far-field effects of the MOOB while results along the Talas-Fergana shear zone were interpreted as a response to the Lhasa collision.

Sedimentary records of surrounding basins record periodic deposition of sediments in response to deformation during the Meso-Cenozoic period. The Junggar and Tarim basins record the deposition of conglomerates and coarse clastic alluvial sediments during the Late Triassic-Early Jurassic, Early Cretaceous, Late Cretaceous-Palaeocene, and Neogene (Choulet et al., 2013; Dumitru et al., 2001; Hendrix et al., 1992; Jolivet et al., 2010). These punctuated sequences of coarse strata are interpreted to be a result of the Cimmerian and India-Eurasia collisions with a possible influence from the MOOB.

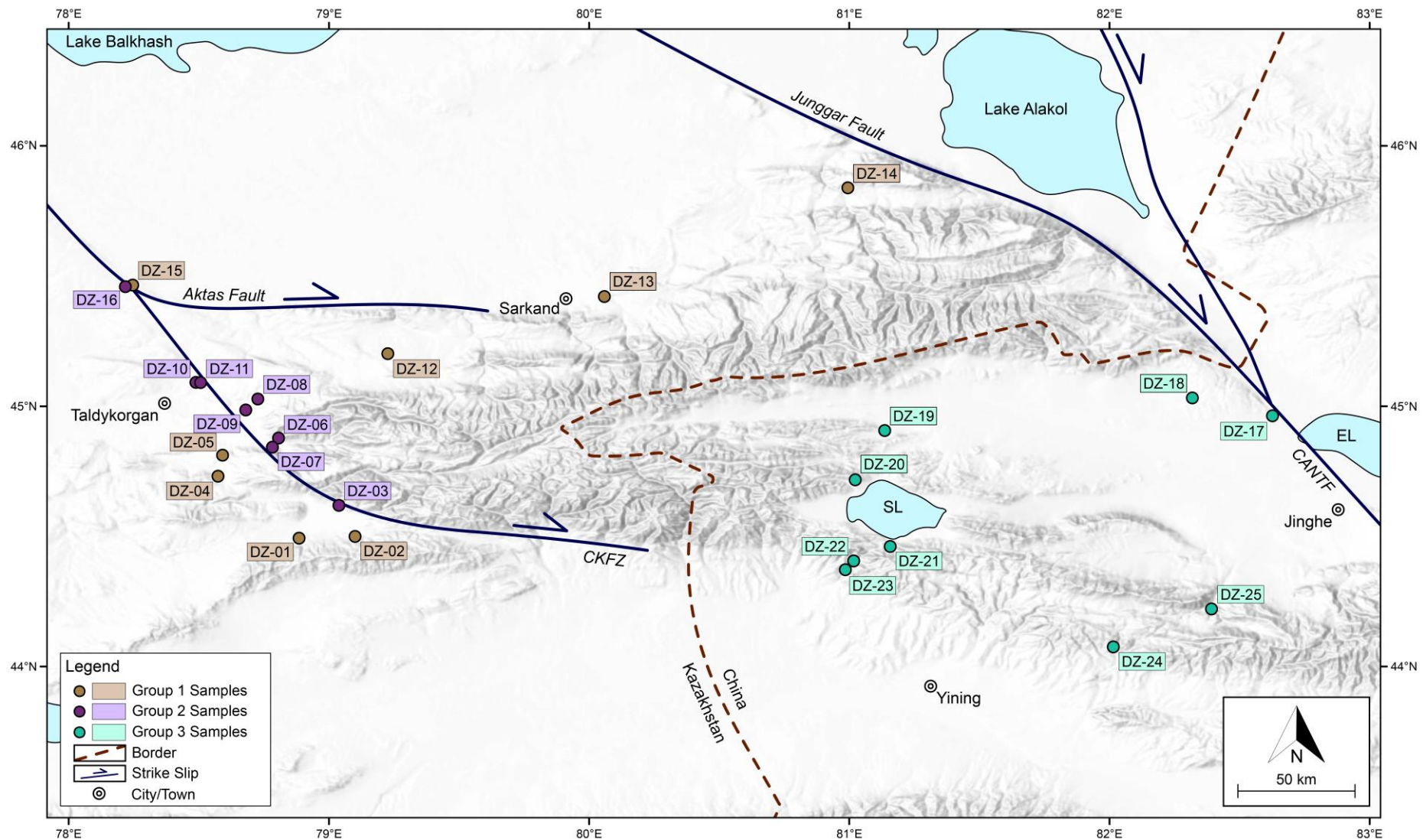


Figure 2 – Topographic map of the Junggar Alatau and surroundings. Samples locations are indicated by coloured dots associated with their groups, brown = Group 1, purple = Group 2 and teal = Group 3, while cities are indicated by ringed dots. The border shared by Kazakhstan and China is indicated by the dashed line. Strike slip faults are indicated by a solid line and an arrow indicating the direction of movement. Main faults after Choulet et al. (2012), De Pelsmaeker et al. (2015) and Li et al. (2018). CANTF = Chingiz-Alakol-North Tian Shan Fault, CKFZ = Central Kazakhstan Fault Zone, EL = Ebi Lake, SL = Sayram Lake.

### 3. METHODS

#### 3.1. Laboratory processing

Samples were collected in the Junggar Alatau by ATLaS (Adelaide Thermochronology Laboratory and Service) PhD students (Jack Gillespie and Gilby Jepson) and prepared by crushing, sieving and mineral separation using standard methods at the Institute of Geology and Geophysics, Chinese Academy of Sciences (IGGCAS). At the University of Adelaide, the apatite grains were mounted in EpoxyCure resin onto thin section slides and then ground and polished to expose the grains (See Appendix A for complete process outline). Etching of the samples was completed in a solution of 5M HNO<sub>3</sub> for 20±0.5 seconds at 20±0.5°C to reveal the natural fission tracks.

#### 3.2. Apatite fission track and U–Pb method

Imaging of individual grains from each sample was conducted on a Zeiss AXIO Imager M2m Autoscan System with a magnification of x1000. Following imaging, fission track densities and confined track lengths in the individual grains were measured using FastTracks software. Measuring of <sup>238</sup>U concentrations in individual grains was conducted through 30µm spot analysis using laser ablation inductively coupled plasma mass spectrometry (LA-ICP-MS) on a solid state New Wave-213 laser coupled with an Agilent 7900x mass spectrometer. Iolite software was used for the process of data reduction (Paton, Hellstrom, Paul, Woodhead, & Hergt, 2011) with Madagascar apatite used as the primary standard in U–Pb analysis and NIST 610 as the primary standard in AFT analysis. Secondary standards of Durango and McClure apatite were both used to test the accuracy of the analysed data (see results section for details).

### 3.3. Apatite fission track analysis

AFT ages record the thermal history of apatite grains while travelling through the apatite partial annealing zone (APAZ) that occurs between temperatures of ~60-120°C (Wagner et al., 1989). As  $^{238}\text{U}$  decays, fission products are propelled through the apatite crystal lattice creating linear fission tracks (Gleadow, Duddy, Green, & Lovering, 1986b). These fission tracks will anneal (shorten) when the samples pass through the APAZ, reducing their lengths and density. The extent of this annealing process is proportional to the timing and rate of cooling (Chew & Spikings, 2015; Wagner et al., 1989). Confined fission track length measurements are used to infer the cooling history through the APAZ, where a higher population of short track lengths indicate more time spent in the APAZ and thus a slower cooling rate (Gleadow, Duddy, Green, & Hegarty, 1986a).

Central AFT ages of samples were calculated from the ages of individual grains using RadialPlotter software (Vermeesch, 2009, 2017). Samples that pass the chi-squared ( $\chi^2$ ) test with a value  $>0.05$  (O'Sullivan & Parrish, 1995) and display a single-grain age dispersion of  $<25\%$  are regarded as a single population. Samples that fail the  $\chi^2$  test or have a dispersion of  $>25\%$  are considered to display heterogeneity (Galbraith & Laslett, 1993) in single-grain ages and could contain multiple populations. The automatic mixture model in RadialPlotter was used for samples that were considered to contain multiple populations to statistically define the age populations. These populations are correlated with variations in the apatite chemical compositions (using Cl and U) to verify if the statistically derived population are potentially meaningful. Elevated Cl concentrations are known to reduce fission track annealing (Green, Duddy, Gleadow, Tingate, & Laslett, 1986), while U has been proposed to enhance annealing (Hendriks & Redfield, 2005), and therefore, different compositions could reflect different degrees of annealing within a single sample. The apatite chemistry (Cl in this study) was introduced as a kinetic parameter in subsequent thermal history modelling.

### 3.4. Apatite U–Pb analysis

Apatite uranium-lead (AU–Pb) ages record cooling ages between temperatures of ~350–550°C (Chew, Petrus, & Kamber, 2014; Chew & Spikings, 2015). The specific closure temperature and the rate of which Pb is lost are dependent on the chemical composition (Chew & Spikings, 2015). Because of the significant presence of common-Pb in apatite, a population of grains are required to calculate an AU–Pb age. Applying an isochron linear regression through single-grain  $^{238}\text{U}/^{206}\text{Pb}$  and  $^{207}\text{Pb}/^{206}\text{Pb}$  ratios (using a Tera-Wasserburg Concordia plot) gives the AU–Pb age through the lower intercept (Chew et al., 2014). In this work, the AU–Pb ages are mostly used as high-temperature references and compared against their respective AFT age to constrain whether the samples have experienced low-temperature (partial) resetting.

### 3.5. Low-temperature thermal history modelling

Using QTQt software version 5.6.0 (Gallagher, 2012), thermal history models were constructed for samples using individual grain AFT ages and confined track lengths. When available, other constraints (e.g. AU–Pb and depositional age) were added to resolve the thermal history. The temperature at the timing of deposition for the sedimentary samples has been set at  $22.5 \pm 2.5^\circ\text{C}$ . For basement samples, AU–Pb ages were introduced into the modelling, reflecting temperatures of  $400 \pm 50^\circ\text{C}$ .

The modelling procedure involved running 10,000 possible models as a test run to gauge the plausibility of thermal history models. Models deemed as statistically acceptable were further refined by running an extra 200,000 possible models. QTQt software generates four different models: maximum likelihood, maximum posterior, maximum mode, and expected. In further discussion, the ‘expected’ models were used for each sample as these models returned the best match with the input data.

**Table 1 – Analytical details for the LA-ICP-MS as used in AFT and AU–Pb dating.**

Laser	
Type	Nd:YAG
Brand and Model	ESI NWR213
Wavelength	213nm
Pulse Duration	~4ns
Spot Size	30µm
Repetition Rate	5Hz
Laser Fluence	~4J cm <sup>-2</sup>
ICP-MS	
Brand and Model	Agilent 7900x
Forward Power	1350W
Torch Depth	4.5mm
Gas Flow (L min <sup>-1</sup> )	
Carrier (He)	0.7
Sample (Ar)	0.88
Data Acquisition Parameters	
Data Acquisition Protocol	Time-resolved analysis
Scanned Masses	<sup>29</sup> Si, <sup>35</sup> Cl, <sup>43</sup> Ca, <sup>55</sup> Mn, <sup>88</sup> Sr, <sup>89</sup> Y, <sup>202</sup> Hg, <sup>204</sup> Pb, <sup>206</sup> Pb, <sup>207</sup> Pb, <sup>208</sup> Pb, <sup>232</sup> U, <sup>238</sup> U
Detector Mode	Peak hopping, pulse and analog counting
Background Collection	30 seconds
Ablation for Age Calculation	30 seconds
Washout	20 seconds
Standards	
Primary Standards	Madagascar apatite, NIST 610
Secondary Standards	Durango apatite, McClure apatite

## 4. RESULTS

### 4.1. Samples

**Table 2 – Sample locations and lithology details. Crystallisation and depositional (indicated by asterisks) ages from Petrov et al. (2016).**

Sample	Latitude (N)	Longitude (E)	Altitude (m)	Crystallisation/Depositional Ages	Lithology
DZ-01	44.49281	78.89156	1440	Carboniferous	Granite
DZ-02	44.49974	79.10671	1776	Carboniferous	Granodiorite
DZ-03	44.61891	79.04423	1521	Carboniferous	Granodiorite
DZ-04	44.73114	78.57965	1011	Carboniferous	Granite
DZ-05	44.81153	78.59735	1038	Carboniferous	Granite
DZ-06	44.87727	78.81242	1114	Carboniferous	Granodiorite
DZ-07	44.84244	78.7892	1260	Carboniferous	Granite
DZ-08	45.02715	78.73286	1141	Carboniferous	Granodiorite
DZ-09	44.98546	78.68664	960	Carboniferous	Granodiorite
DZ-10	45.0916	78.49511	628	Carboniferous	Granitic Gneiss
DZ-11	45.09101	78.5129	648	Carboniferous	Granodiorite
DZ-12	45.20145	79.23236	1253	Permian	Granodiorite
DZ-13	45.42118	80.06469	1024	Permian	Granite
DZ-14	45.83873	81.00055	1042	Permian	Granodiorite
DZ-15	45.46473	78.25181	489	Permian	Granite
DZ-16	45.45921	78.22339	508	Permian	Granodiorite
DZ-17	44.96321	82.6329	208	Permian	Kspar Granite
DZ-18	45.03172	82.32456	668	Permian	Granite
DZ-19	44.90617	81.14242	1404	Silurian	Kspar Granite/Leucogranite
DZ-20	44.7169	81.02879	2576	Carboniferous*	Fine Lithic Wacke
DZ-21	44.46077	81.1632	1856	Neoproterozoic*	Schist
DZ-22	44.40522	81.02278	1368	Carboniferous	Diorite
DZ-23	44.37169	80.99087	1228	Carboniferous	Altered Porphyritic Granite
DZ-24	44.07527	82.02129	1295	Permian	Kspar Granite
DZ-25	44.22109	82.39847	1453	Devonian	Granite

A total of twenty-five samples were collected (Figure 2). All samples were analysed using the AFT method and twenty-four samples were analysed using the AU–Pb method (one sample was excluded due to the relative absence of sufficient radiogenic-Pb). Major NW-SE orientated shear zones were targeted to constrain the reactivation of this structural architecture. Sample locations and rock descriptions are detailed in Table 2 and locations shown in Figure 2. Twenty-three samples were sourced from Palaeozoic basement rocks of

granitic to dioritic composition, in some cases showing alteration or gneissic metamorphism.

DZ-20 was sourced from the Dongtujinhe Formation (~313–300 Ma) and DZ-21 from a metamorphosed sedimentary outcrop with an unknown age. Samples are grouped by their proximity to shear zones, AFT age, and/or location to provide insights into the differential exhumation experienced in the study area (Figures 2-3).

- Group 1 consists of eight samples DZ-01, DZ-02, DZ-04, DZ-05, DZ-12, DZ-13, DZ-14 and DZ-15. The samples were predominately taken distal to major shear zones and record AFT ages spanning the early Permian-Early Jurassic. All these samples have source locations within Kazakhstan.
- Group 2 consists of eight samples DZ-03, DZ-06, DZ-07, DZ-08, DZ-09, DZ-10, DZ-11 and DZ-16 that were taken in vicinity to the CKFZ and record AFT ages spanning the Middle Jurassic-Late Cretaceous. Similar to Group 1, all these samples were taken within Kazakhstan.
- Group 3 consists of nine samples DZ-17, DZ-18, DZ-19, DZ-20, DZ-21, DZ-22, DZ-23, DZ-24 and DZ-25. The samples are predominantly distal to major shear zones and record AFT ages spanning the middle Permian-Late Jurassic. All Group 3 samples were sourced from within China.

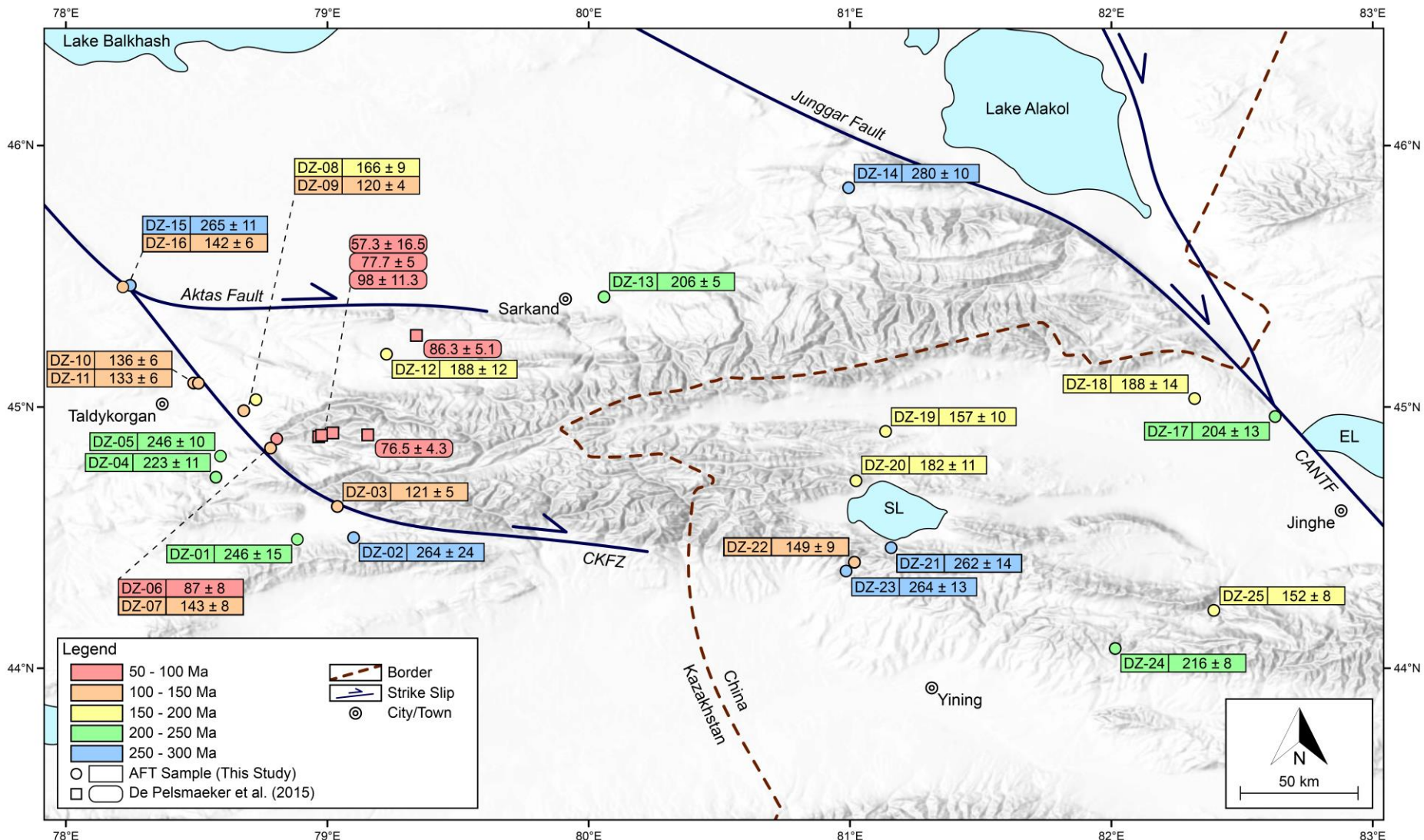


Figure 3 – Topographic map of the Junggar Alatau and surroundings. Dots indicate sample locations with AFT ages from this study and square symbols show the locations for previous results reported by De Pelsmaeker et al. (2015). AFT ages are colour coded at 50 Ma increments. The border shared by Kazakhstan and China is indicated by the dashed line. Strike slip faults are indicated by a solid line and an arrow indicating the direction of movement. Cities and towns are represented by ringed dots. Main faults after Choulet et al. (2012), De Pelsmaeker et al. (2015) and Li et al. (2018). CANTF = Chingiz-Alakol-North Tian Shan Fault, CKFZ = Central Kazakhstan Fault Zone, EL = Ebi Lake, SL = Sayram Lake

## 4.2. Apatite fission track results

**Table 3 – Summary AFT table organised by sample group.**  $\rho_s$  represents the average density of spontaneous fission tracks. Ns represents the number of tracks counted across all grains. n represents the number of grains analysed.  $^{35}\text{Cl}$  and  $^{238}\text{U}$  represent the average concentrations in grains analysed with  $1\sigma$  as the reported uncertainty. t represents the central AFT age calculated with RadialPlotter (Vermeesch, 2009) with  $1\sigma$  as the reported uncertainty. nl represents the number of confined fission tracks measured from all grains in the sample. MTL represents the mean track length of the measured confined fission tracks with SD as the  $1\sigma$  standard deviation of distribution. Disp represents the level of dispersion among single-grain AFT ages with  $P(\chi^2)$  representing the probability that the analysed grains are of a single population, calculated with RadialPlotter.

Sample	$\rho_s$ ( $\times 10^5/\text{cm}^2$ )	Ns	n	$^{35}\text{Cl}$ (ppm)	$1\sigma$ (ppm)	$^{238}\text{U}$ (ppm)	$1\sigma$ (ppm)	t (Ma)	$1\sigma$ (Ma)	nl	MTL ( $\mu\text{m}$ )	SD ( $\mu\text{m}$ )	Disp (%)	$P(\chi^2)$
Group 1														
DZ-01	8.2	494	37	18288	3353	7.80	0.68	246	15	84	12.12	2.08	19	0.09
DZ-02	4.0	139	24	35730	9988	3.36	0.38	264	24	54	12.53	2.00	0	1.00
DZ-04	7.1	447	32	2046	691	7.13	0.50	223	11	45	11.11	1.93	0	0.68
DZ-05	10.7	1067	32	10253	1137	9.37	0.67	246	10	55	12.68	1.61	13	0.07
DZ-12	12.2	507	23	21483	3731	13.48	0.94	188	12	62	12.45	2.14	16	0.11
DZ-13	36.9	2799	43	2204	923	37.46	2.28	206	5	174	12.99	1.34	8.4	0.07
DZ-14	12.1	1510	40	25489	3734	8.95	0.61	280	10	100	13.60	1.26	12	0.05
DZ-15	5.7	801	36	531	201	4.81	0.30	265	11	94	12.95	1.60	9.9	0.12
Group 2														
DZ-03	9.9	1147	39	573	225	17.69	1.12	121	5	100	13.03	1.33	13	0.06
DZ-06	7.0	244	18	2901	584	17.83	1.20	87	8	38	11.28	1.83	22	0.06
DZ-07	12.7	534	27	27419	3956	20.07	1.61	143	8	93	11.90	2.17	14	0.09
DZ-08	6.9	592	31	6277	4806	9.36	0.86	166	9	72	12.79	1.80	16	0.11
DZ-09	15.7	1334	39	10454	2384	28.08	1.83	120	4	100	12.58	1.83	10	0.06
DZ-10	5.0	884	40	4548	644	8.16	0.51	136	6	100	12.76	1.59	15	0.07
DZ-11	9.3	933	32	4774	911	14.03	1.15	133	6	80	12.69	1.54	15	0.05
DZ-16	10.8	1027	35	766	168	16.64	1.19	142	6	100	12.92	1.46	14	0.05
Group 3														
DZ-17	8.9	313	18	19252	5366	9.64	0.86	204	13	34	12.83	1.43	5.6	0.38
DZ-18	8.6	336	23	15434	3066	9.53	0.76	188	14	100	12.04	1.60	19	0.13
DZ-19	6.8	268	25	1588	440	8.88	0.59	157	10	38	11.85	2.07	5	0.84
DZ-20	5.0	427	31	4095	776	6.16	0.43	182	11	82	13.33	1.59	15	0.33
DZ-21	9.5	588	31	26699	4656	8.07	0.54	262	14	82	12.09	1.89	17	0.06
DZ-22	7.3	438	29	4853	1094	10.79	0.78	149	9	79	12.10	1.74	17	0.07
DZ-23	12.6	714	31	10926	1259	10.06	0.81	264	13	100	12.69	1.71	14	0.08
DZ-24	12.7	1323	42	2026	389	12.82	0.89	216	8	100	11.91	1.73	14	0.05
DZ-25	18.6	817	27	73096	12444	28.13	2.26	152	8	100	12.36	1.61	16	0.07

#### 4.2.1. DATA ACCURACY

Durango apatite was used for zeta calibration (Vermeesch, 2017) of single-grain AFT ages for unknown apatite samples. The weighted average AFT age yielded by Durango apatite in this work was  $30.1 \pm 1.2$  Ma (Figure 4). This is within the error of the published  $^{40}\text{Ar}/^{39}\text{Ar}$  age of  $31.44 \pm 0.18$  Ma (McDowell, McIntosh, & Farley, 2005), suggesting reliable fission track results.

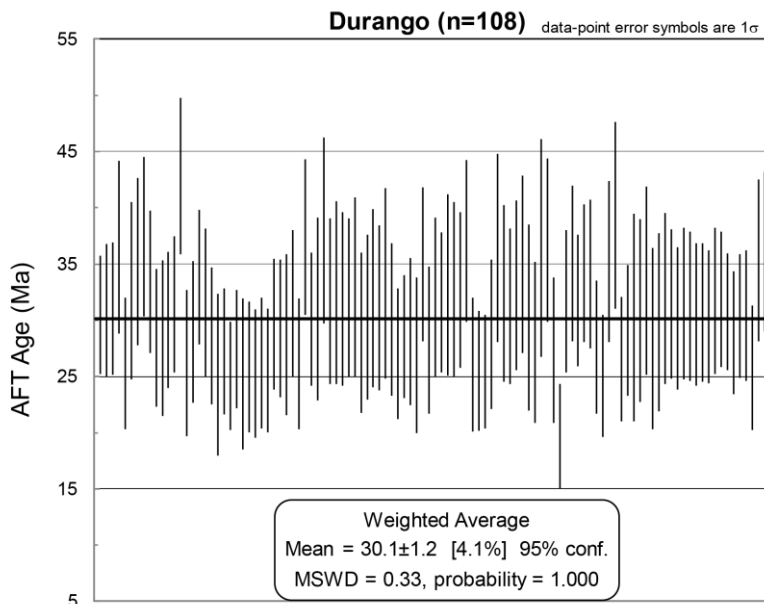
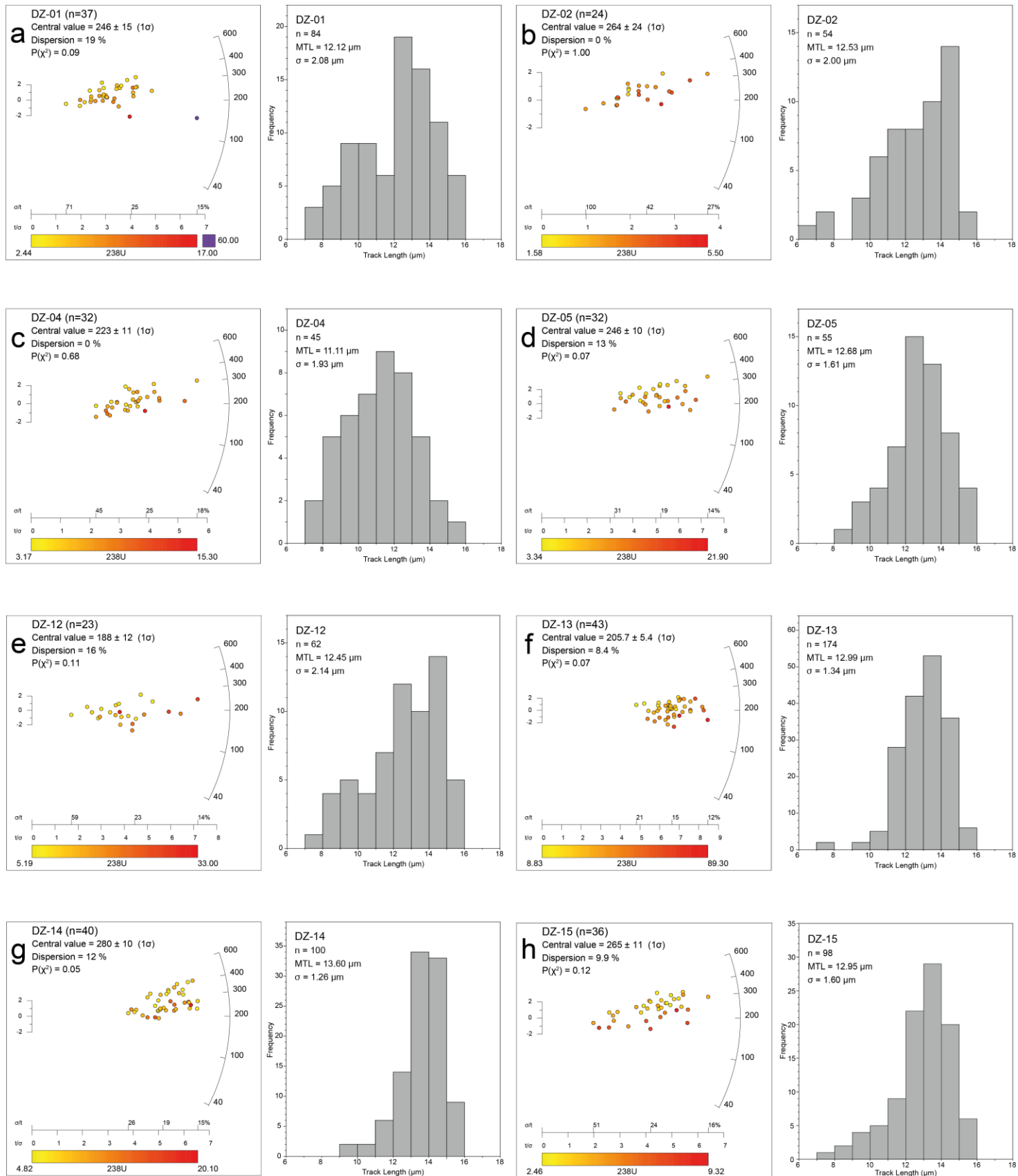


Figure 4 – AFT weighted average age for analysed secondary standard Durango apatite.

#### 4.2.2. GROUP 1

Group 1 is characterised by the oldest central AFT ages in the study region. Central AFT ages range from  $280 \pm 10$  Ma to  $188 \pm 12$  Ma (Figure 5). In more detail, samples DZ-14, DZ-15, DZ-02, DZ-01, DZ-05, DZ-04, DZ-13 and DZ-12 yield central AFT ages of  $280 \pm 10$  Ma,  $265 \pm 11$  Ma,  $264 \pm 24$  Ma,  $246 \pm 15$  Ma,  $246 \pm 10$  Ma,  $223 \pm 11$  Ma,  $206 \pm 5$  Ma and  $188 \pm 12$  Ma respectively. All samples passed the  $\chi^2$  test and yield single-grain age dispersions of  $<25\%$ , suggesting each sample records a single-grain age population. Sufficient number of confined fission tracks ( $\geq 30$ ) were measured in all samples,

producing mean track lengths (MTLs) of  $13.60\mu\text{m}$ ,  $12.95\mu\text{m}$ ,  $12.53\mu\text{m}$ ,  $12.12\mu\text{m}$ ,  $12.68\mu\text{m}$ ,  $11.11\mu\text{m}$ ,  $12.99\mu\text{m}$  and  $12.45\mu\text{m}$  respectively (Table 3, Figure 5). The pooled radial plot for Group 1 yields a central AFT age of  $236\pm4$  Ma and yields two statistically defined age peaks with a P1 (peak 1) AFT age of  $201\pm9$  Ma and a P2 (peak 2) AFT age of  $277\pm13$  Ma (Figure 5).



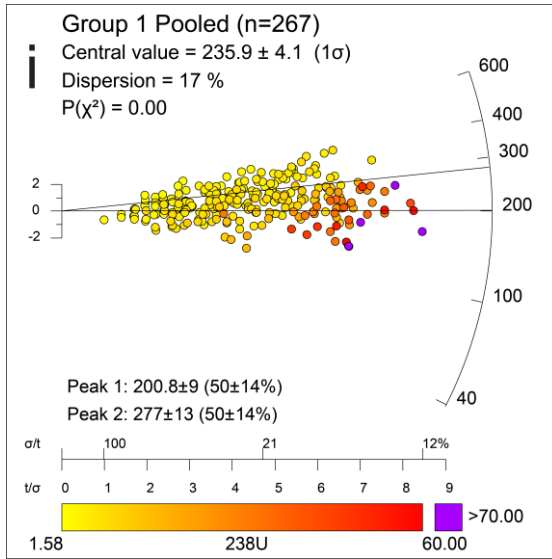
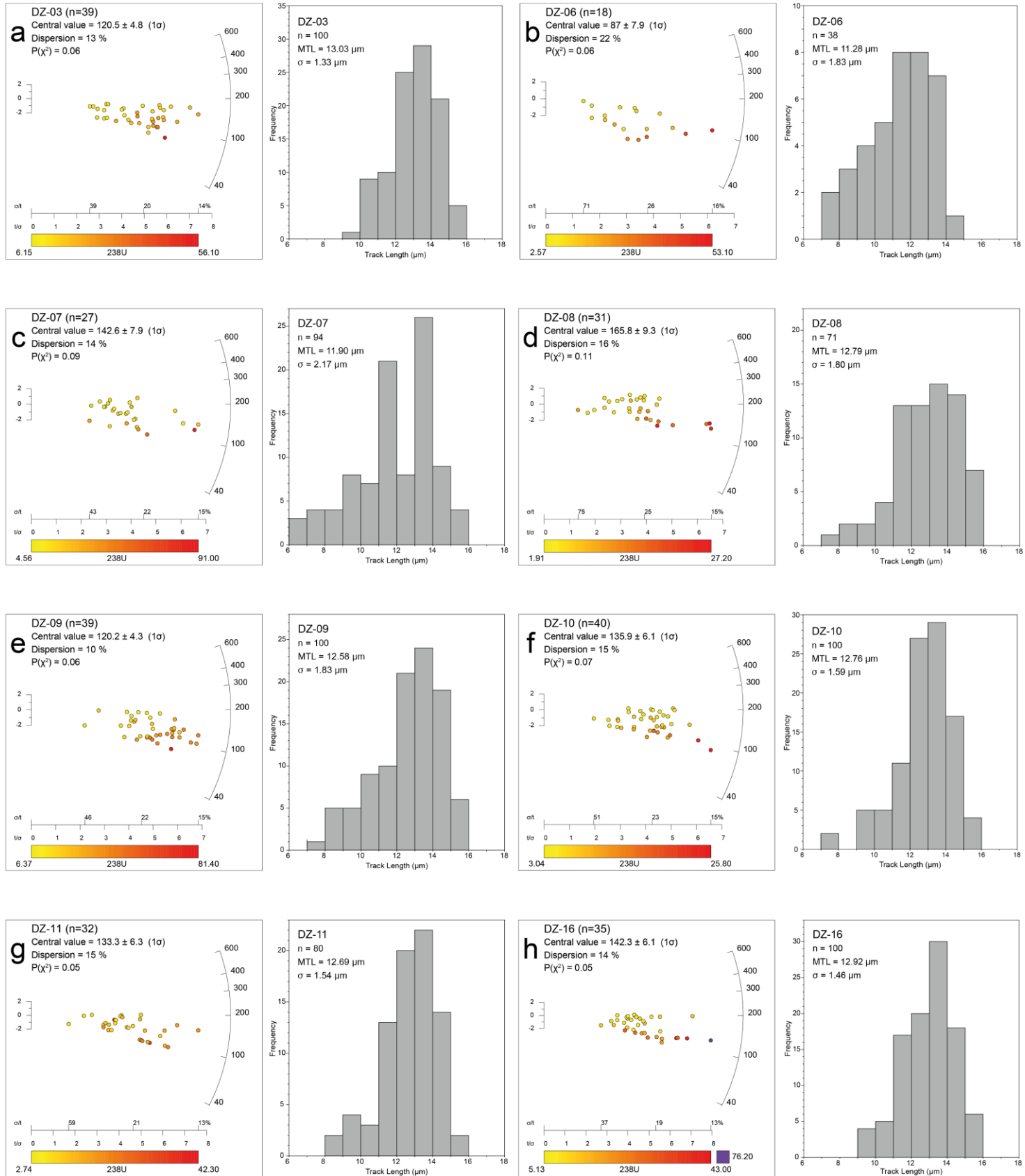


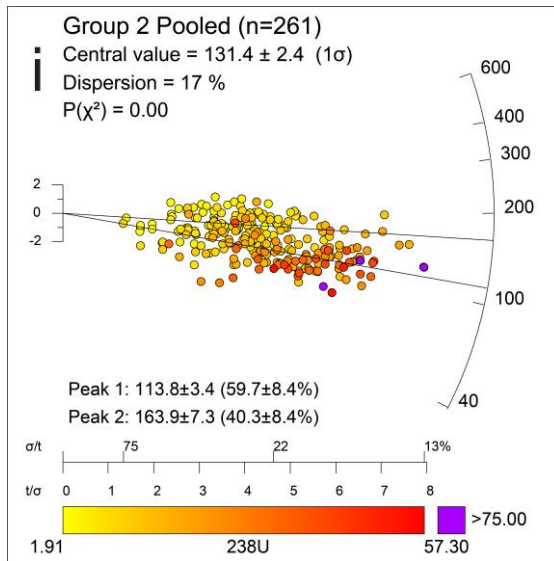
**Figure 5 – Radial plots of calculated AFT ages for samples associated with Group 1 (a-h) and a pooled sample radial plot (i) with all analysed grains in Group 1.** Central age values and age-peak discriminations using an automatic mixture model were calculated with RadialPlotter software (Vermeesch, 2009). The percentage of data contained within the peaks are bracketed next to the associated ages. The coloured scale indicates the concentration of  $^{238}\text{U}$  in ppm within the analysed grains. The x-axis indicates the level of uncertainty in the single-grain ages and decreases from left to right. The curved y-axis to the right shows increasing age in Ma with the y-axis to the left representing  $2\sigma$  from the central age value. Frequency plots depict the distribution of confined fission track lengths in a sample. n indicates the number of tracks measured, MTL the mean track length, and  $\sigma$  the standard deviation of measured track lengths.

#### 4.2.3. GROUP 2

Group 2 is characterised by the youngest central AFT ages in the study region. Central AFT ages range from  $166 \pm 9$  Ma to  $87 \pm 8$  Ma (Figure 6). Samples DZ-08, DZ-07, DZ-16, DZ-10, DZ-11, DZ-03, DZ-09 and DZ-06 yield central AFT ages of  $165 \pm 9$  Ma,  $143 \pm 8$  Ma,  $142 \pm 6$  Ma,  $136 \pm 6$  Ma,  $133 \pm 6$  Ma,  $121 \pm 5$  Ma,  $120 \pm 4$  Ma and  $87 \pm 8$  Ma respectively. All basement samples passed the  $\chi^2$  test and yield single-grain age dispersions of  $<25\%$ , suggesting each sample records a single-grain age population. Sufficient number of confined fission tracks were measured in all samples with MTLs of  $12.79 \mu\text{m}$ ,  $11.90 \mu\text{m}$ ,  $12.92 \mu\text{m}$ ,  $12.76 \mu\text{m}$ ,  $12.69 \mu\text{m}$ ,  $13.03 \mu\text{m}$ ,  $12.58 \mu\text{m}$  and  $11.28 \mu\text{m}$  respectively (Table 3, Figure 6). The pooled radial plot for Group 2 yields a central AFT age of  $131 \pm 2$  Ma and yields two statistically defined age peaks with a P1 AFT age of

$114\pm3$  Ma and a P2 AFT age of  $164\pm7$  Ma (Figure 6). High uranium concentrations are associated with P1, which yields a younger AFT age than P2.

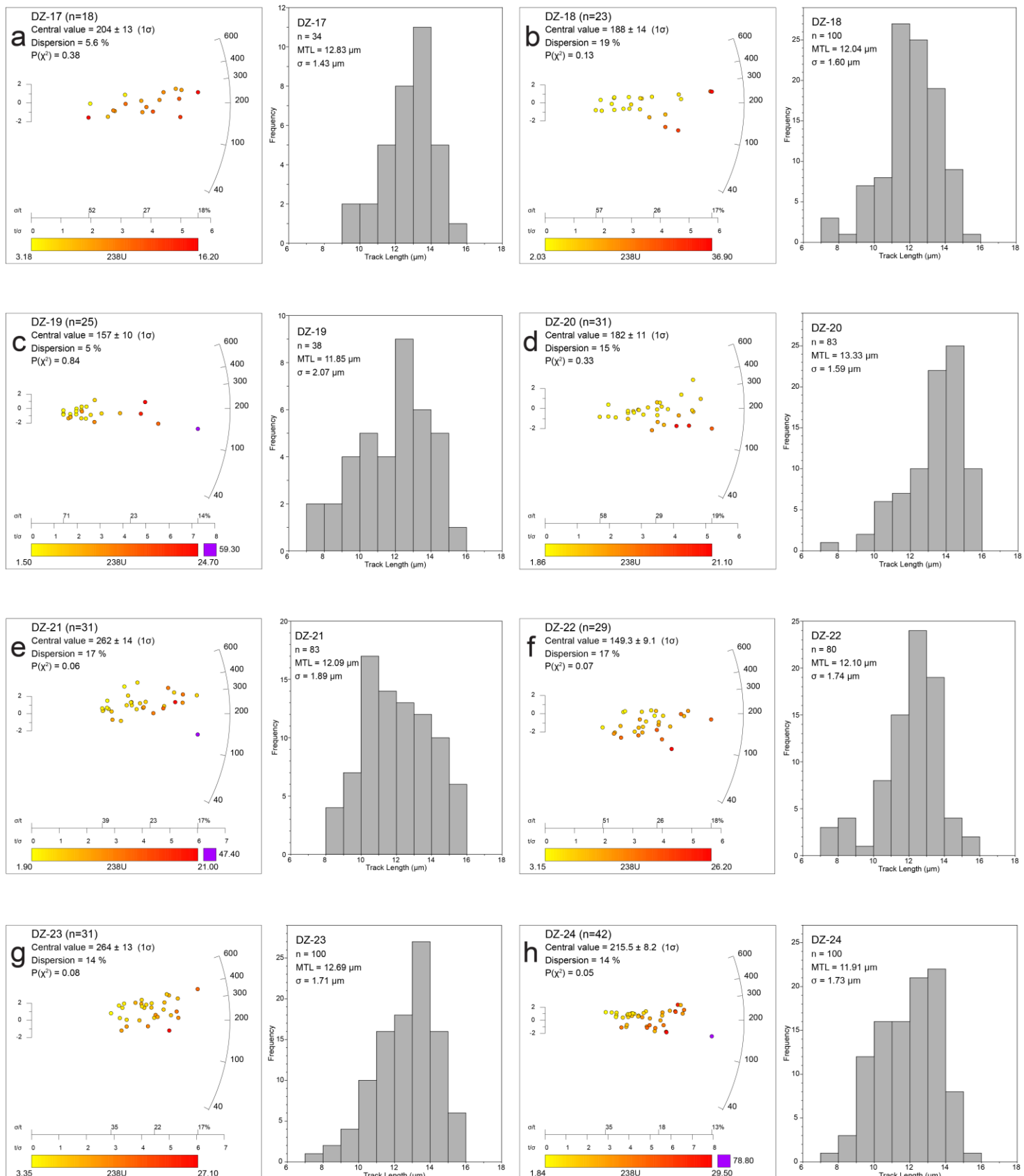




**Figure 6 – Radial plots of calculated AFT ages for samples associated with Group 2 (a-h) and a pooled sample radial plot (i) with all analysed grains in Group 2 (caption as in Figure 5).**

#### 4.2.4. GROUP 3

Group 3 is characterised by samples located on the Chinese slopes of the Junggar Alatau. Central AFT ages range from  $264 \pm 13$  Ma to  $149 \pm 9$  Ma (Figure 7). Samples DZ-23, DZ-21, DZ-24, DZ-17, DZ-18, DZ-20, DZ-19, DZ-25 and DZ-22 yield central AFT ages of  $264 \pm 13$  Ma,  $262 \pm 14$  Ma,  $216 \pm 8$  Ma,  $204 \pm 13$  Ma,  $188 \pm 14$  Ma,  $182 \pm 11$  Ma,  $157 \pm 10$  Ma,  $152 \pm 8$  Ma and  $149 \pm 9$  Ma respectively. All samples (including the sedimentary samples) passed the  $\chi^2$  test and yield single-grain age dispersions of  $< 25\%$ , suggesting each sample records a single-grain age population. Sufficient number of confined fission tracks were measured in all samples with MTLs of  $12.69 \mu\text{m}$ ,  $12.09 \mu\text{m}$ ,  $11.91 \mu\text{m}$ ,  $12.83 \mu\text{m}$ ,  $12.04 \mu\text{m}$ ,  $13.33 \mu\text{m}$ ,  $11.85 \mu\text{m}$ ,  $12.36 \mu\text{m}$  and  $12.10 \mu\text{m}$  respectively (Table 3, Figure 7). The pooled radial plot for Group 3 yields a central AFT age of  $199 \pm 4$  Ma and yields two statistically defined age peaks with a P1 AFT age of  $145 \pm 6$  Ma and a P2 AFT age of  $241 \pm 7$  Ma (Figure 7).



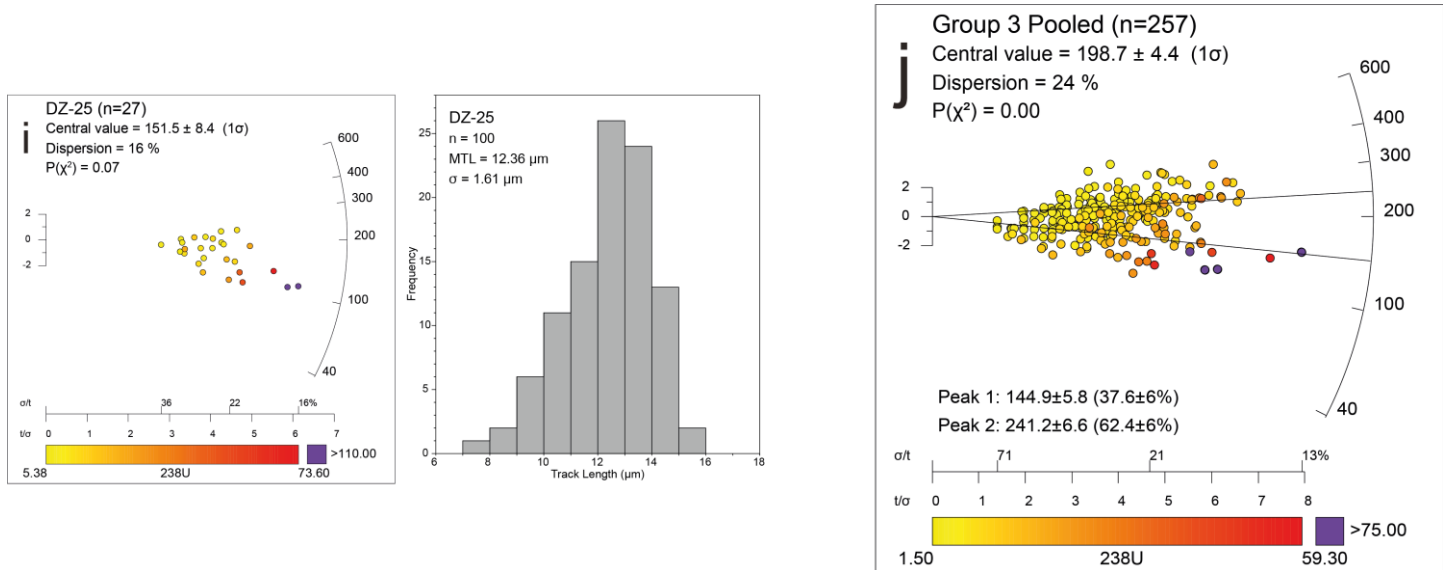


**Figure 7 – Radial plots of calculated AFT ages for samples associated with Group 3 (a-i) and a pooled sample radial plot (j) with all analysed grains in Group 3 (caption as in Figure 5).**

#### 4.2.5. POOLED STUDY AREA

The pooled radial plot for all samples yields a central AFT age of  $183 \pm 3$  Ma and yields three statistically defined age peaks with a P1 AFT age of  $123 \pm 3$  Ma, a P2 AFT age of  $211 \pm 10$  Ma and a P3 AFT age of  $290 \pm 23$  Ma (Figure 8). The different peaks in this pooled plot correspond with the range of AFT ages defined for the different sample groups. Group 1 yields AFT ages in the late Palaeozoic-early Mesozoic, Group 2 yields AFT ages in the early Mesozoic, and Group 3 yields AFT ages in the mid to late Mesozoic. Grains with higher uranium are mostly (but not conclusively) associated with the youngest age peak.

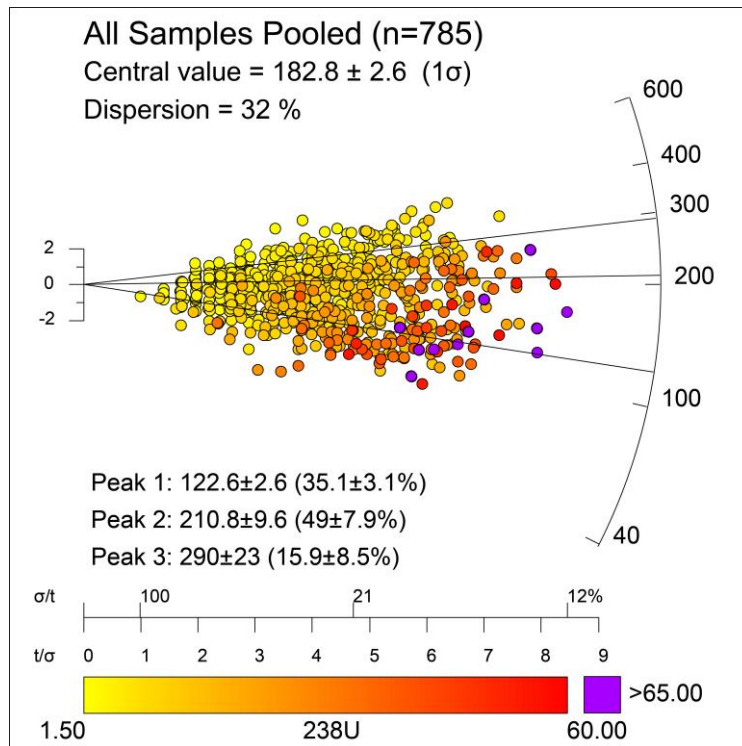


Figure 8 – Calculated AFT ages of all samples in a single pooled radial plot (caption as in Figure 5).

#### 4.3. Apatite U-Pb results

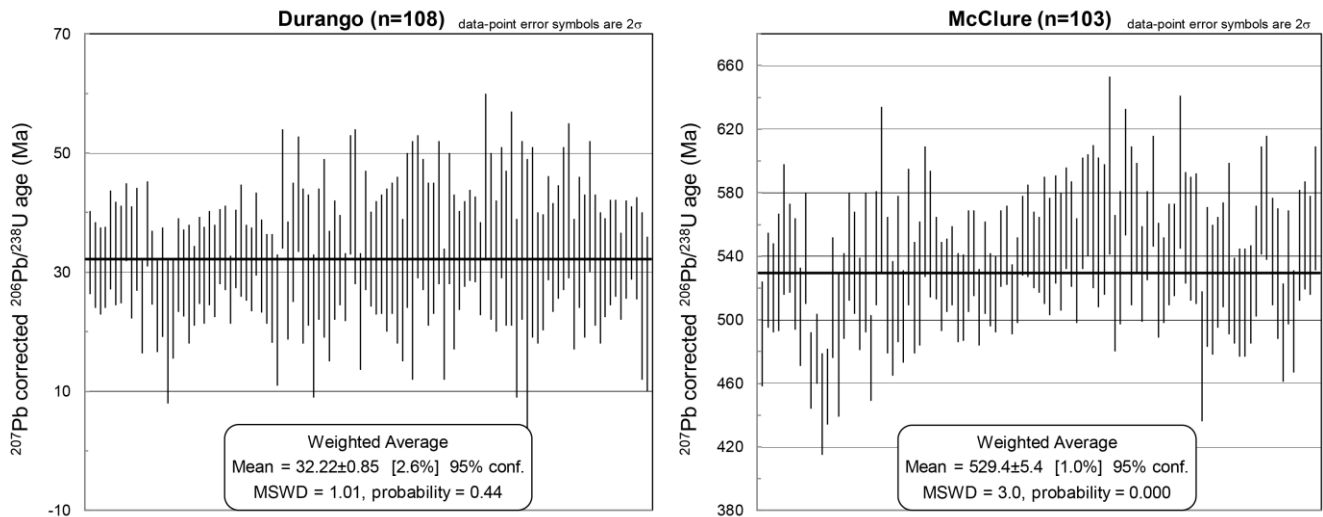
Twenty-four samples yield meaningful AU–Pb ages. Lower intercept ages range from the Late Ordovician ( $447 \pm 20$  Ma) to the early Permian ( $281 \pm 25$  Ma). AU–Pb ages are detailed in Table 4, where they are compared with the central AFT ages and (where available) with published zircon U–Pb (ZU–Pb) ages. Grains that experienced analytical problems (such as obvious down-hole zonation) were treated as outliers and were removed from the age calculations. In addition, inverse concordant grains (plotting to the left side of the Concordia curve) have too high common-Pb ratios and were therefore excluded as well (Figure 10).

**Table 4 – Summary AU–Pb age table with AFT and ZU–Pb age comparisons organised by sample number.** n represents the number of grains used in AU–Pb analysis. MSWD represents the mean square weighted deviation of AU–Pb data. AU–Pb Age is given by the lower intercept age of the Tera-Wasserburg Concordia plot with 95% confidence uncertainty. AFT Age represents the central AFT age calculated with RadialPlotter (Vermeesch, 2009) with  $1\sigma$  as the reported uncertainty. ZU–Pb Age is the crystallisation/depositional age from published data reported by De Pelsmaeker et al. (2015), Huang et al. (2017), Wang et al. (2018) and references therein. Samples with no published ZU–Pb data use mapped ages reported by Petrov et al. (2016) and are referred to by geologic age. Asterisks indicate the youngest zircon age from a detrital population.

Sample	Lithology	n	MSWD	AU–Pb Age (Ma)	$2\sigma$ (Ma)	AFT Age (Ma)	$1\sigma$ (Ma)	Published ZU–Pb Ages (Ma)
DZ-01	Granite	25	1.7	335	21	246	15	341
DZ-02	Granodiorite	-	-	-	-	264	24	341
DZ-03	Granodiorite	43	1.6	379	14	121	5	341
DZ-04	Granite	19	1.2	304	24	223	11	341
DZ-05	Granite	28	1.5	397	24	246	10	341
DZ-06	Granodiorite	19	1.5	310	13	87	8	341
DZ-07	Granite	28	1.8	380	17	143	8	341
DZ-08	Granodiorite	25	1.7	376	20	166	9	341
DZ-09	Granodiorite	37	1.2	362	8	120	4	341
DZ-10	Granitic Gneiss	34	0.7	434	20	136	6	341
DZ-11	Granodiorite	34	1.5	410	30	133	6	341
DZ-12	Granodiorite	19	1.4	280	29	188	12	298–260
DZ-13	Granite	36	1.4	283	10	206	5	298–260
DZ-14	Granodiorite	35	1.2	330	29	280	10	298–260
DZ-15	Granite	36	0.7	431	58	265	11	298–260
DZ-16	Granodiorite	33	1.2	290	11	142	6	298–260
DZ-17	Kspar Granite	15	0.8	297	18	204	13	306–292
DZ-18	Granite	20	1.1	281	25	188	14	306–292
DZ-19	Kspar Granite /Leucogranite	15	1.7	414	23	157	10	Silurian
DZ-20	Fine Lithic Wacke	32	1.5	353	13	182	11	313*
DZ-21	Schist	29	0.9	447	20	262	14	Neoproterozoic
DZ-22	Diorite	28	1.3	373	13	149	9	Carboniferous
DZ-23	Altered Porphyritic Granite	34	1.1	387	14	264	13	Carboniferous
DZ-24	Kspar Granite	43	1.2	351	6	216	8	Permian
DZ-25	Granite	22	1.5	391	10	152	8	Devonian

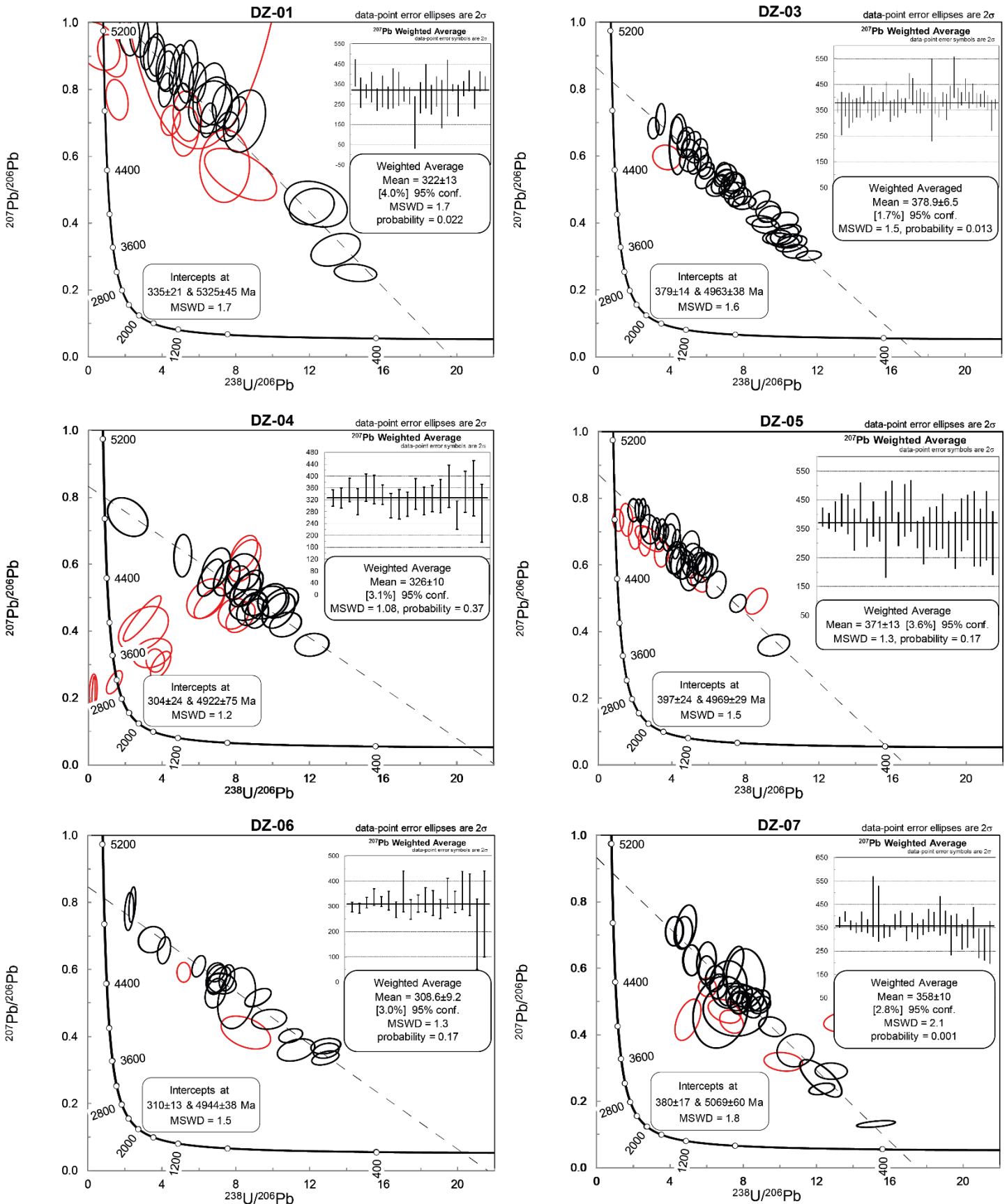
#### 4.3.1. DATA ACCURACY

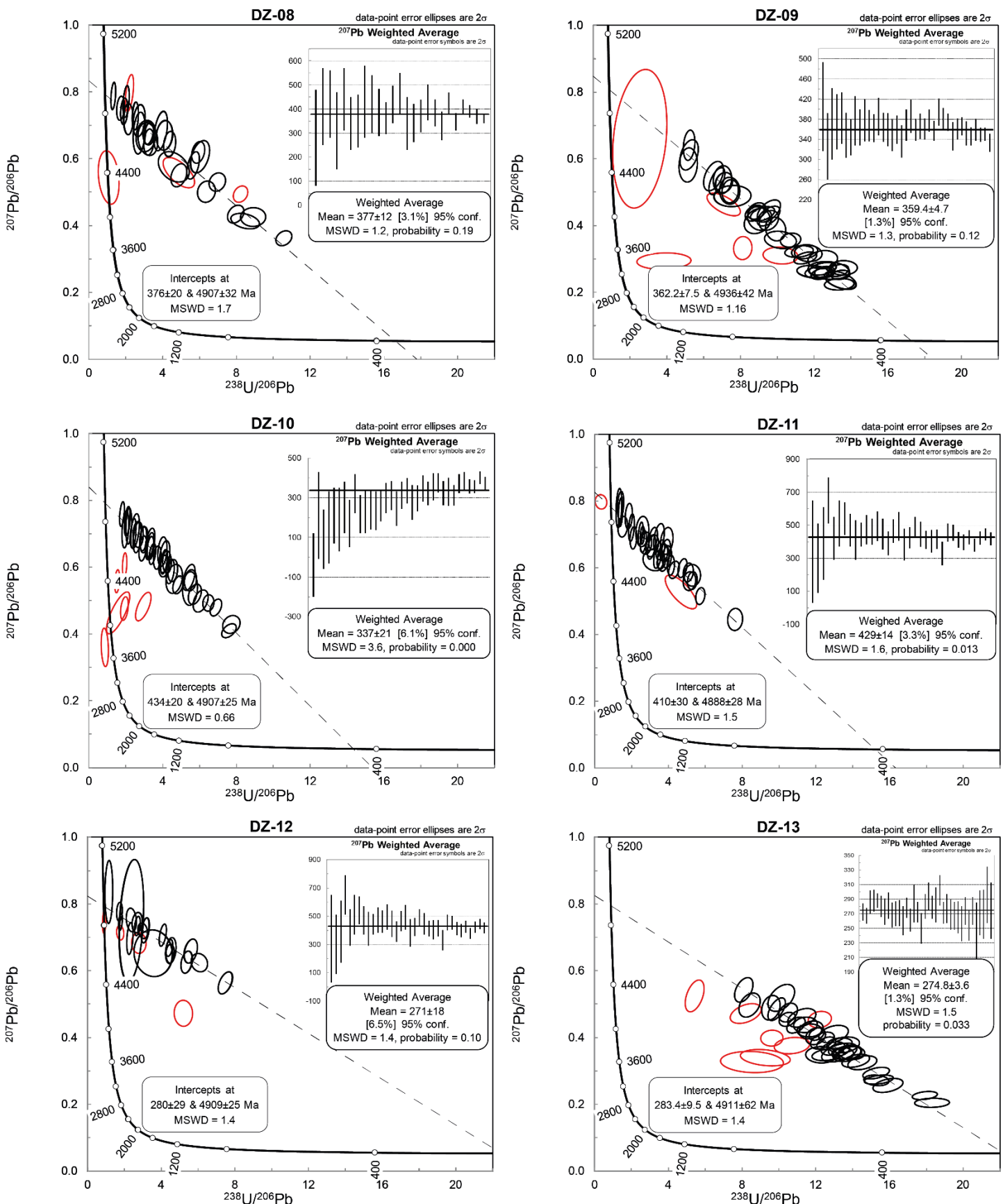
Durango and McClure apatites were used as accuracy checks for the U-Pb age of unknown apatite samples. Durango apatite yielded a  $^{207}\text{Pb}$  corrected weighted average  $^{206}\text{Pb}/^{238}\text{U}$  age of  $32.22 \pm 0.85$  Ma and McClure apatite yielded an age of  $529.4 \pm 5.4$  Ma (Figure 9). These values are in good agreement to the published  $^{40}\text{Ar}/^{39}\text{Ar}$  age for Durango apatite at  $31.44 \pm 0.18$  Ma (McDowell et al., 2005) and the published AU–Pb age of McClure apatite at  $524.6 \pm 3.2$  Ma (Chew et al., 2014). The AU–Pb age data for the analysed samples can thus be treated as being reliable.

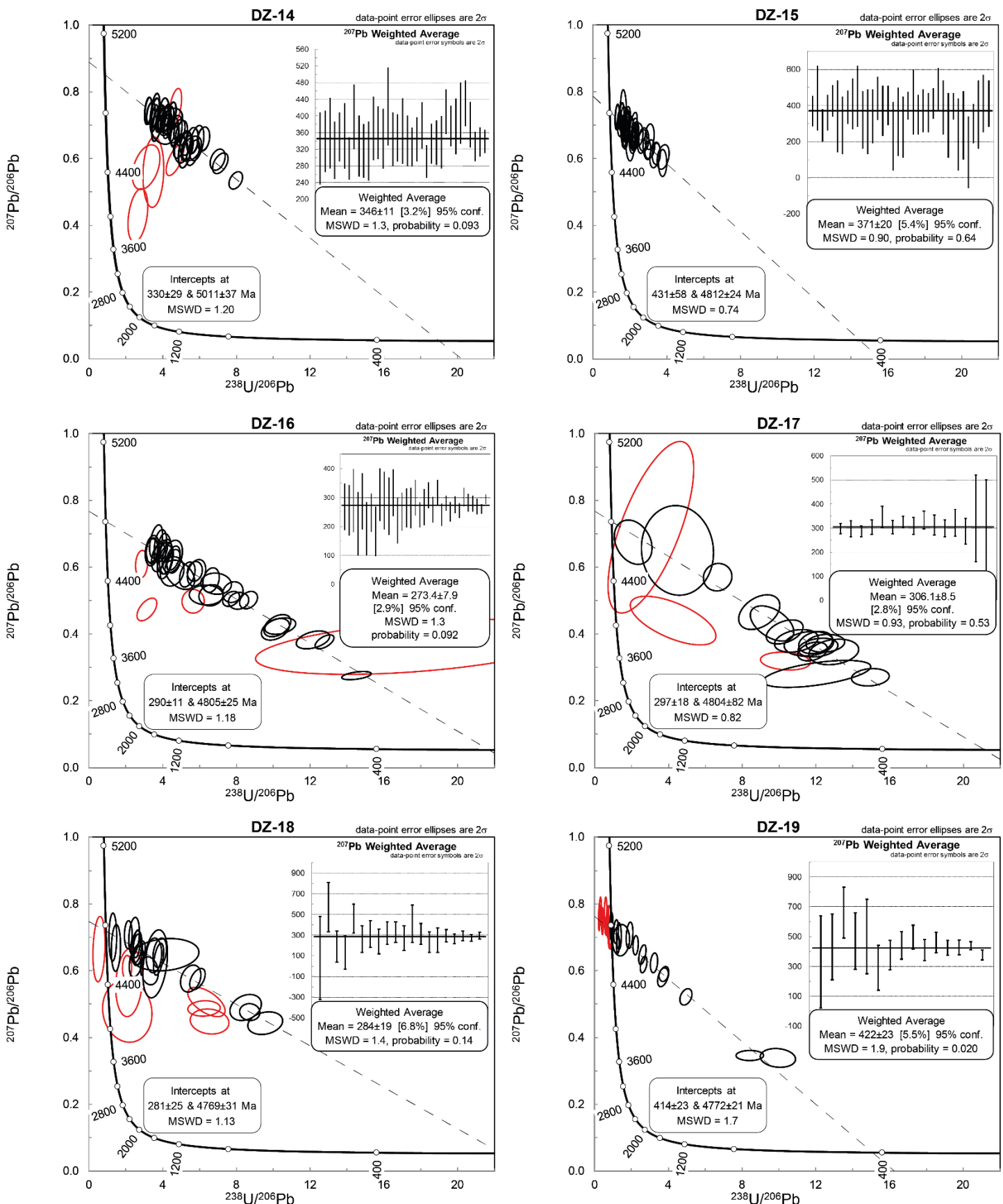


**Figure 9 –  $^{207}\text{Pb}$  corrected weighted average  $^{206}\text{Pb}/^{238}\text{U}$  ages for analysed secondary standards: Durango apatite and McClure apatite.**

#### 4.3.2. TERA-WASSERBURG CONCORDIA PLOTS







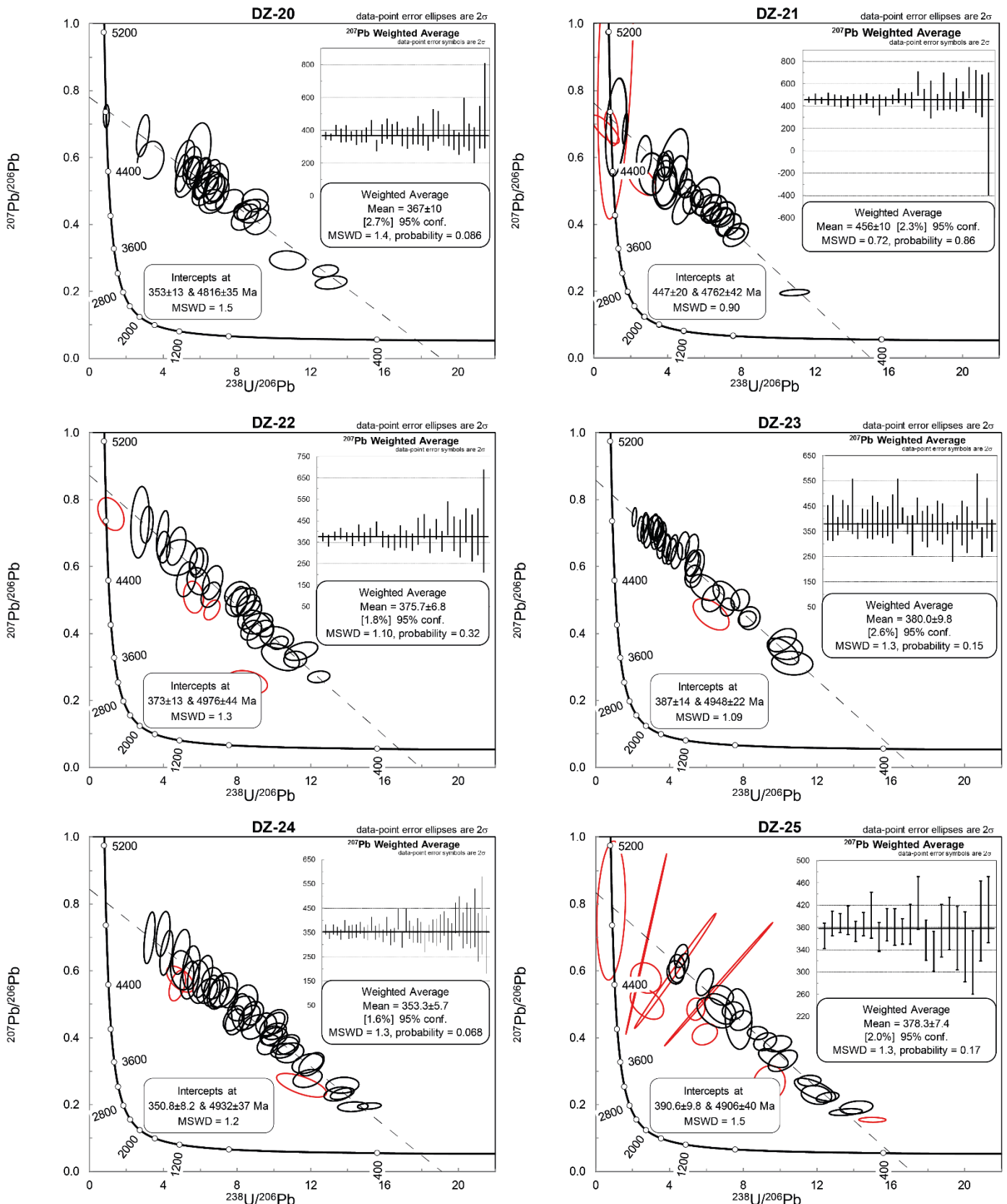


Figure 10 – Tera-Wasserburg Concordia plots for all samples excluding DZ-02 in the Junggar Alatau. Red ellipses indicate grains that were considered as outliers and/or experienced analytical problems and were removed from final calculations. Black ellipses indicate grains used to produce the common-Pb line. Each ellipse represents a  $2\sigma$  uncertainty for  $^{207}\text{Pb}/^{206}\text{Pb}$  and  $^{238}\text{U}/^{206}\text{Pb}$ .  $^{207}\text{Pb}$  corrected weighted average  $^{206}\text{Pb}/^{238}\text{U}$  age plots are inset for all samples.

#### 4.4. Thermal history modelling

##### 4.4.1. GROUP 1

Thermal history models for Group 1 (Figure 11) record cooling through the APAZ since ~300–280 Ma with DZ-04 and DZ-14 demonstrating rapid cooling through the APAZ at ~270–260 Ma. Sample DZ-04 records a moderate re-entry into the APAZ between ~210 Ma and ~40 Ma. The models for other samples (DZ-01, DZ-02, DZ-05 and DZ-15) record prolonged APAZ residence (slow cooling) between ~310 Ma and ~110 Ma (Figure 11). A second cooling event is evident in thermal history models for DZ-12 and DZ-13, starting at ~230 Ma. DZ-12 experienced a decrease in cooling rate at ~220 Ma and cooled to present day temperatures leaving the APAZ at ~100 Ma. DZ-13 experienced rapid cooling leaving the APAZ at ~210 Ma. As a consequence of high presence of common-Pb and some analytical problems, no AU–Pb age could be obtained for DZ-02. Using DZ-01’s AU–Pb age, DZ-02 was constrained below the APAZ, assuming DZ-01 and DZ-02 were sourced from the same Carboniferous pluton as suggested by mapped crystallisation ages (De Pelsmaeker et al., 2015; Petrov et al., 2016).

In summary, the thermal history models for Group 1 record evidence for rapid cooling at ~270–260 Ma and at ~230–210 Ma with slow cooling between these two time periods.

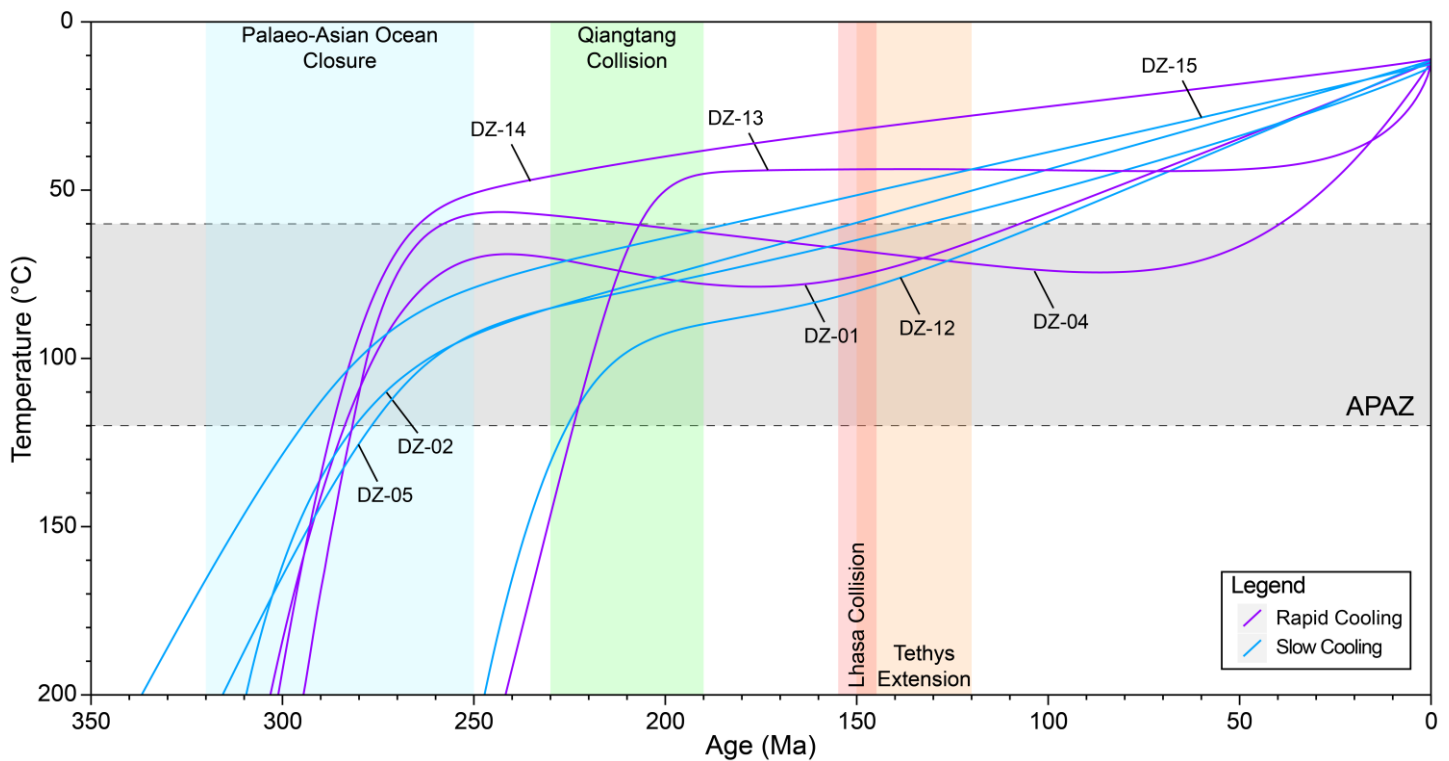


**Figure 11 – Combined thermal history model for samples associated with Group 1.** The grey zone represents the apatite partial annealing zone (APAZ) between ~60–120°C (Wagner, Gleadow, & Fitzgerald, 1989). The timing of regional tectonic events are represented by coloured zones, blue zone = Palaeo-Asian Ocean closure (320–250 Ma), green zone = Qiangtang collision (230–190 Ma), red zone = Lhasa collision (~150 Ma) and the orange zone = Tethys extension (150–120 Ma). Rapid cooling is indicated by solid purple lines and slower cooling with solid blue lines. DZ-02 was constrained below the APAZ with the AU–Pb age of DZ-01.

#### 4.4.2. GROUP 2

Thermal history models for Group 2 (Figure 12) record cooling through the APAZ since ~200–120 Ma with DZ-03, DZ-09, DZ-10, DZ-11 and DZ-16 demonstrating more rapid cooling through the APAZ at ~170–150 Ma. The models for DZ-07 and DZ-08 record prolonged APAZ residence between ~200–60 Ma. Sample DZ-06 enters the APAZ later at ~120 Ma. The models for DZ-06 and DZ-07 reveal a decrease in cooling rate at ~90 Ma and ~170 Ma respectively, followed by DZ-06 recording an increase in cooling rate at ~30 Ma.

In summary, the thermal history models for Group 2 record evidence for rapid cooling through the APAZ at  $\sim$ 170–150 Ma and mostly slow cooling before and after this time period.

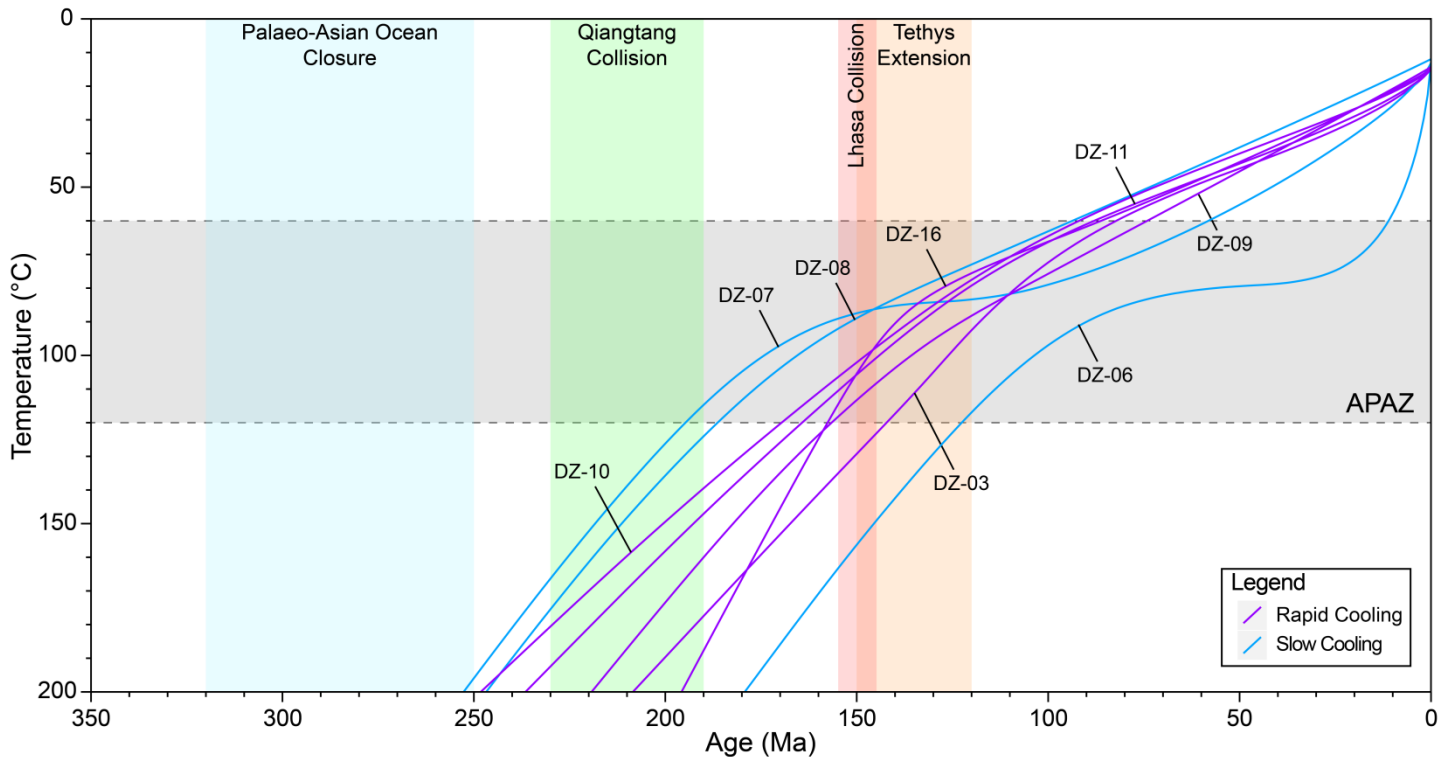


**Figure 12 – Combined thermal history model for samples associated with Group 2 (caption as in Figure 11).**

#### 4.4.3. GROUP 3

Thermal history models for Group 3 (Figure 13) preserve a cooling history, starting since  $\sim$ 300–260 Ma (samples DZ-23 and DZ-24). Sample DZ-23 records slow cooling between  $\sim$ 300–140 Ma while DZ-24 records rapid cooling initially followed by APAZ residence between  $\sim$ 260–50 Ma. Evidence for a second thermal event is recorded at  $\sim$ 220–180 Ma (samples DZ-17, DZ-18, DZ-19, DZ-20, DZ-22 and DZ-25). DZ-17 and DZ-18 record rapid cooling through the APAZ between  $\sim$ 220–210 Ma, followed by slow cooling after that time period. Samples DZ-19, DZ-22 and DZ-25 record more

prolonged APAZ residence with a slower rate of cooling, leaving the APAZ at ~90–70 Ma.

Sample DZ-20 was constrained using the depositional age of the Dongtujinhe Formation, which is interpreted to range from ca. 313–300 Ma (Huang et al., 2017). The thermal history model indicates heating throughout the late Palaeozoic and early Mesozoic, followed by relatively slow cooling since ~220 Ma. DZ-21 was constrained to present day temperatures with a depositional age of  $770.5 \pm 229.5$  Ma. Information on the sourced outcrop was insufficient to determine the true depositional age. Therefore, an age constraint spanning the Neoproterozoic was used as the sample is located amongst the Qingbaikou and Nanhua-Sinian systems, which were deposited in the Neoproterozoic (Gao et al., 2008; Jian et al., 2003; Zhu et al., 2018). Furthermore, an age constraint for the metamorphism event was not used as the degree of metamorphism nor the timing are known. The model for DZ-21 records slow cooling since ~300 Ma, followed by prolonged shallow APAZ residence between ~230–90 Ma. Note that given the rather poor modelling constraints, this model is likely inaccurate.

In summary, the thermal history models for Group 3 record rapid cooling at ~300–260 Ma and at ~230–220 Ma. DZ-20 records heating to ~120°C between these time periods.

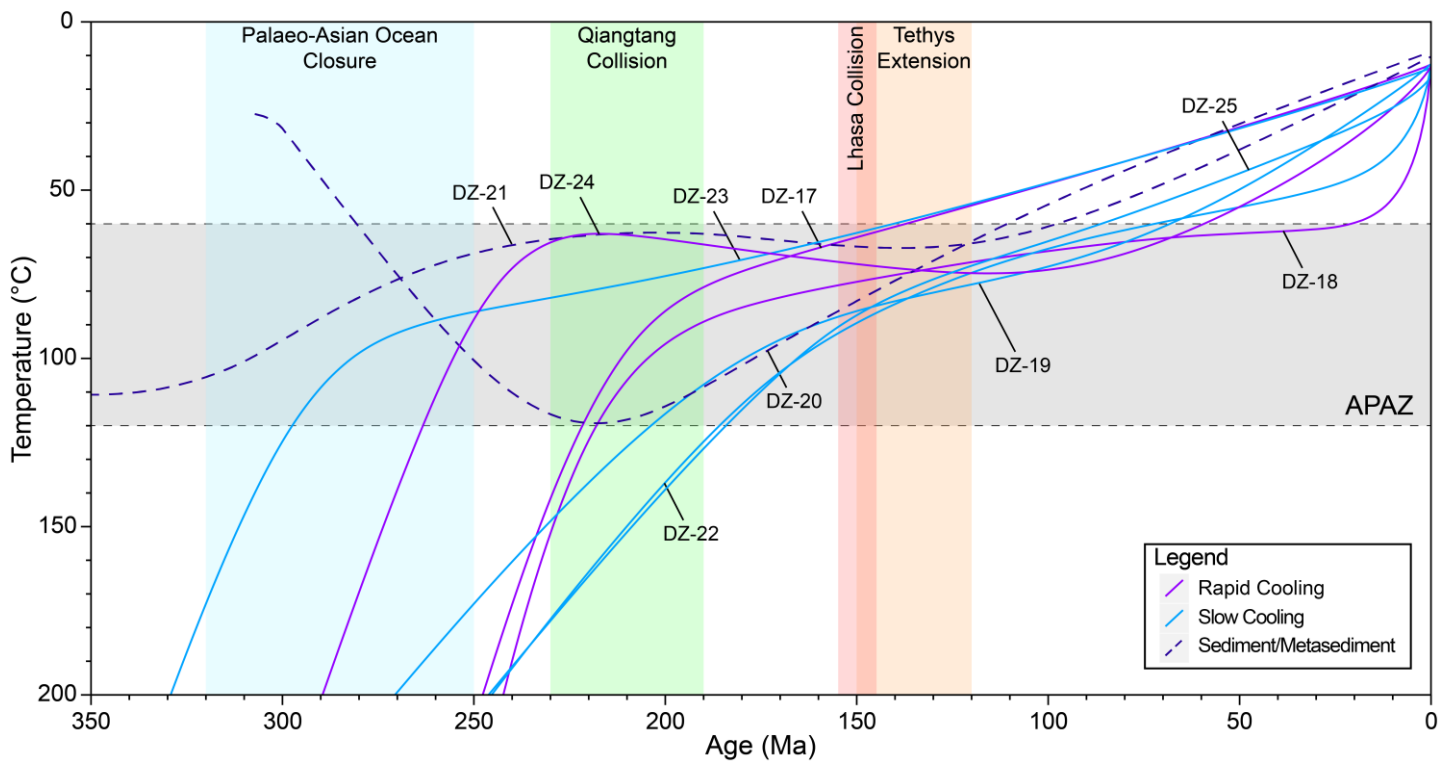


**Figure 13 – Combined thermal history model for samples associated with Group 3.** The grey zone represents the apatite partial annealing zone (APAZ) found between ~60-120°C (Wagner et al., 1989). The timing of regional tectonic events are represented by coloured zones, blue zone = Palaeo-Asian Ocean closure (320-250 Ma), green zone = Qiangtang collision (230-190 Ma), red zone = Lhasa collision (~150 Ma) and the orange zone = Tethys extension (150-120 Ma). Rapid cooling is indicated by solid purple lines, slower cooling with solid blue lines, and sediment/metasediments with dashed navy lines. DZ-20 was constrained to the surface with an approximate depositional age of  $306.5 \pm 6.5$  Ma at present day temperatures of  $22.5 \pm 2.5^\circ\text{C}$ , while DZ-21 was constrained with an age of  $770.5 \pm 229.5$  Ma.

## 5. DISCUSSION

### 5.1. AU-Pb age interpretations

AU-Pb ages are compared to published ZU-Pb data (or mapped crystallisation ages if data is not available) (De Pelsmaeker et al., 2015; Huang et al., 2017; Petrov et al., 2016; Wang et al., 2018) to identify which AU-Pb ages can be attributed to post-magmatic cooling (i.e. when AU-Pb ages are within uncertainty to or just post-date the ZU-Pb ages). In this regard, the AU-Pb ages for samples DZ-01, DZ-04, DZ-06, DZ-12, DZ-13, DZ-14, DZ-16, DZ-17, DZ-18, DZ-19 and DZ-25 are attributed to post-magmatic cooling. The AU-Pb ages for other samples (DZ-03, DZ-05, DZ-07, DZ-08,

DZ-09, DZ-10, DZ-11, DZ-15, DZ-22, DZ-23 and DZ-24) record AU–Pb ages that are (slightly) older than the reported ZU–Pb or mapped ages. This difference should not be possible due to zircon having a greater U–Pb closure temperature in excess of 900°C (Lee, Williams, & Ellis, 1997). This age discrepancy is likely a result of poor crystallisation age constraints, rather than reflecting an analytical issue with the AU–Pb age data.

## 5.2. AFT age interpretations and comparison with AU–Pb age constraints

The thermal history models across the Junggar Alatau display different thermal histories, preserving fast cooling signals during (1) the late Carboniferous-early Permian, (2) the Late Triassic and (3) the Early Cretaceous (Figures 11-13). These fast cooling events can be correlated with a number of thermo-tectonic events that transpired at the distant Eurasian margins throughout the Palaeo-Mesozoic, further discussed below.

Comparing the AU–Pb and AFT ages, samples that have experienced (partial) thermal resetting after crystallisation and magmatic cooling can be identified. Figure 14 plots the AFT versus AU–Pb ages, with the pink band representing the youngest AU–Pb age  $\pm$  uncertainty, recorded for the study area (interpreted as the youngest extent on post-magmatic cooling), while the purple band represents a 1:1 age relationship between the AU–Pb and AFT ages with a maximum  $2\sigma$  uncertainty. Samples outside of the pink and purple bands display evidence for (partial) thermal resetting after post-magmatic cooling.

DZ-14 records the oldest AFT age and (within uncertainty) records the youngest AU–Pb age (sample DZ-12) for the study area (i.e. DZ-14 plots in the pink band in (Figure 14). Hence, this sample has not experienced any post-magmatic thermal resetting. The

uncertainties on the AFT ages for samples DZ-15 and DZ-23 are within the uncertainty range of the pink band in Figure 14, suggesting that these samples have not experienced thermal resetting either. DZ-21 is a metasedimentary sample and its uncertainty overlaps with the range of the pink band, suggesting it has likely been metamorphosed during (or shortly after) granitoid emplacement and has not experienced (significant) subsequent thermal resetting. Hence, the late Carboniferous-early Permian fast cooling signal, recorded in the AFT data, is largely related with post-magmatic cooling. All other samples lie outside the pink and purple bands, indicating that they have experienced a degree of subsequent thermal resetting. The highlighted zones coloured green and orange in Figure 14 correspond to the timing of two different thermo-tectonic events that affected the southern Eurasian margin during the Late Triassic-Early Jurassic and Cretaceous. For the samples that plot within these coloured zones in Figure 14, the timing of cooling through the APAZ can be correlated with these thermo-tectonic events. Although samples DZ-04 and DZ-24 are within the green zone, they do not record thermal histories (Figures 11 and 13) that display cooling as a result of the Late Triassic-Early Jurassic event. Instead, they show fast post-magmatic cooling followed by prolonged residence or re-entry into the APAZ during the latest Triassic, leading to a mixed age between these two events. All other samples within the green and orange zones in Figure 14 record Late Triassic-Early Jurassic and Cretaceous cooling through the APAZ respectively. Therefore, noting the two exceptions mentioned above, the AFT ages can generally be used as a proxy for the timing of onset of cooling in Figure 14. DZ-06 records the youngest AFT age for the study area, correlating with results obtained by De Pelsmaeker et al. (2015) in roughly the same area.

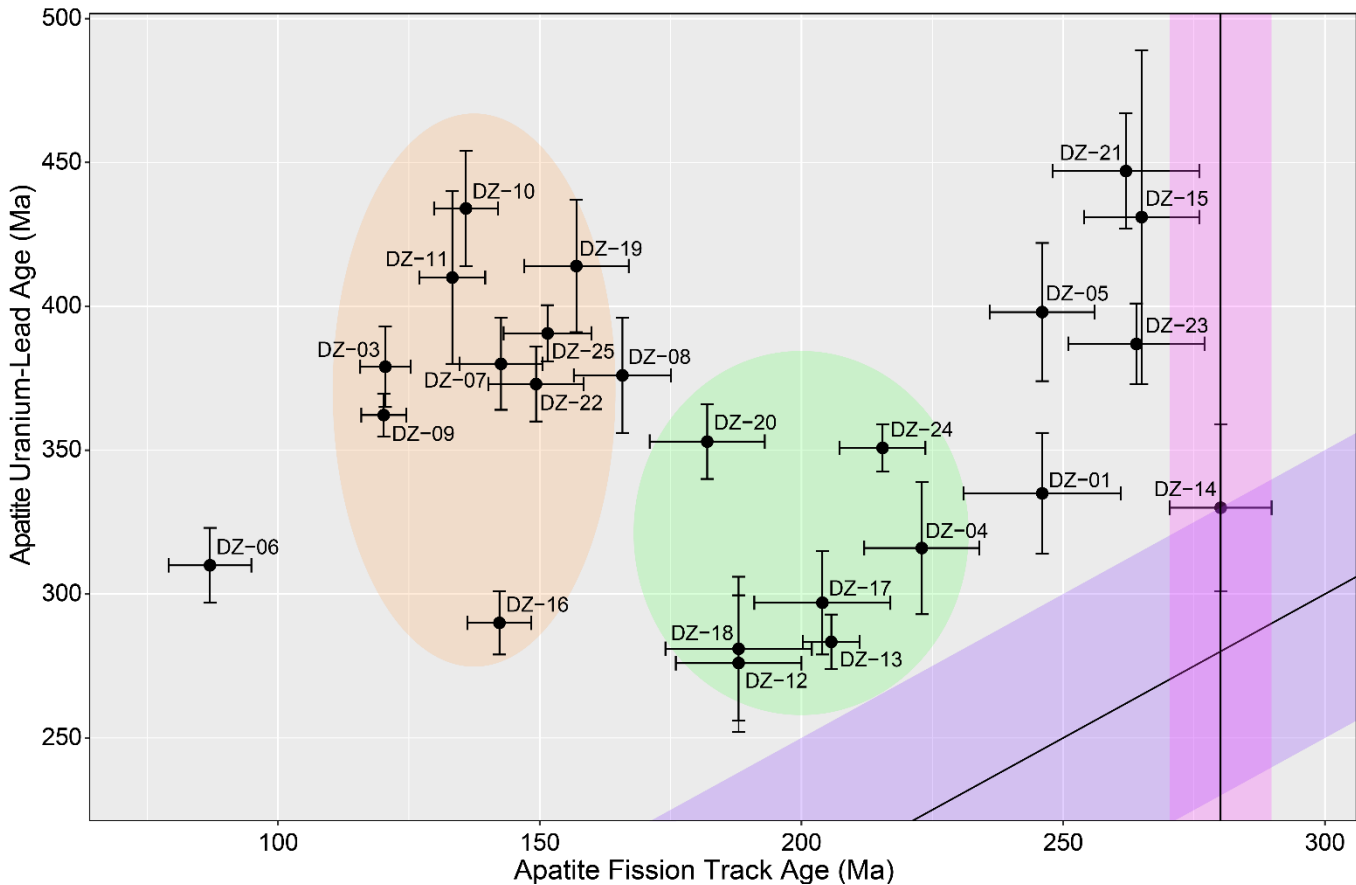


**Figure 14 – AU–Pb vs AFT plot of all samples excluding DZ-02 as no AU–Pb age was calculated. Error bars for each sample represent the uncertainty of the AU–Pb age in Ma on the y-axis and AFT age in Ma on the x-axis. The pink band is the youngest AU–Pb age  $\pm$  uncertainty and the purple band represents a 1:1 age relationship between AU–Pb and AFT ages. Samples outside these two bands record post-magmatic (partial) thermal resetting. Samples in the green and orange zones are likely related to a thermo-tectonic event occurring during those times.**

### 5.3. Boomerang plot

The ‘Boomerang’ plot displays the relationships between the AFT age and Mean Track Length (MTL) for each sample (Gallagher, Brown, & Johnson, 1998; Green, 1986), which can be used to identify the episodic nature of fast cooling events that have affected Central Asia. In this plot, each ‘blade’ of a ‘boomerang trend’ identifies a period of rapid cooling (long MTLs), while the central part of the boomerang trend reveals the timing of slow cooling (mostly short MTLs, reflecting prolonged APAZ residence).

The samples of this study along with samples analysed by De Pelsmaeker et al. (2015) constrain at least two complete boomerang trends throughout the late Palaeozoic-Mesozoic (Figure 15). Initially, rapid cooling is recorded in the early Permian (~280 Ma), representing the timing of post-magmatic cooling (Figure 14). This event is followed by slow cooling and APAZ residence, indicated by increasingly shorter MTLs during the Late Permian-Middle Triassic (~260–225 Ma). From the Late Triassic-Early Jurassic (~225–180 Ma), the MTLs increase in value, indicating an increase in cooling rates. This defines a ‘boomerang blade’ with rapid cooling coinciding with the timing of the Qiangtang collision (Figure 15). The Middle to Late Jurassic (~170–150 Ma) is characterised by another period of slow cooling and increased APAZ residence (shortening of MTLs), which is followed by a new ‘boomerang blade’ (increase in MTLs), suggesting rapid cooling during the Early Cretaceous (~150–120 Ma), coinciding with a period of back-arc extension in the Tethys Ocean. Published AFT data (De Pelsmaeker et al., 2015), in combination with the AFT data for sample DZ-06, suggests a new phase of rapid cooling at ~80-70 Ma.

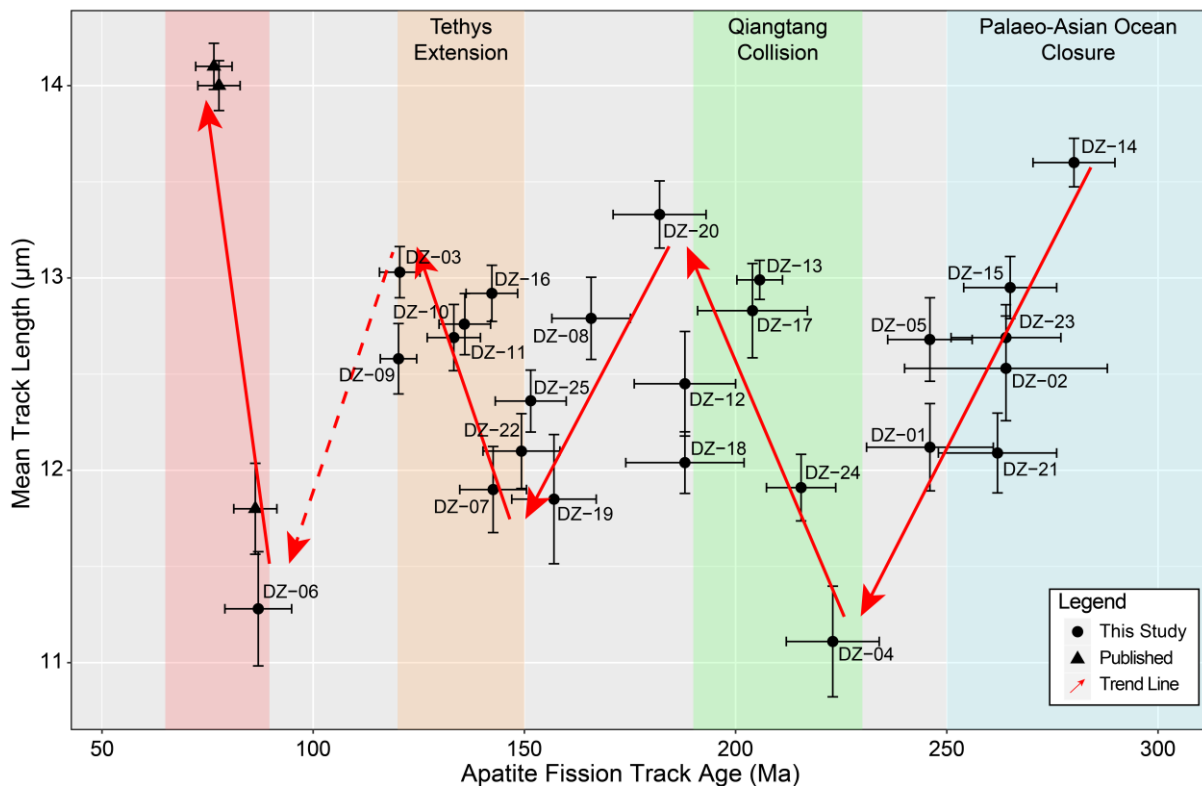


**Figure 15 – ‘Boomerang plot’ based on the relationship between MTL and AFT.** Samples from this study are indicated by circles and triangle symbols show previous results reported by De Pelsmaeker et al. (2015). Error bars represent the uncertainty of the MTL in µm on the y-axis and AFT age in Ma on the x-axis. Blue zone = Palaeo-Asian Ocean closure, green zone = Qiangtang collision, orange zone = Tethys extension, and red zone = Late Cretaceous thermo-tectonic event. The arrows indicate the main trends through the data, suggesting several ‘boomerang’ patterns (refer to text for more details).

#### 5.4. Geographical distribution of cooling events and cooling mechanism

Different thermal histories are preserved in the study area as indicated above.

Geographical differences across the Junggar Alatau can be used to associate preserved cooling signals with the structural architecture of the study area. Groups 1 and 3 which are distal to the CKFZ (Figure 2), primarily preserve either (1) post-magmatic cooling ages for intrusions that were emplaced during the progressive closure of the PAO (e.g. Windley et al., 2007; Xiao et al., 2017) or (2) cooling ages related to exhumation during the Qiangtang collision with Eurasia (e.g. Choulet et al., 2013; Jolivet et al., 2010). In contrast, Group 2 preserves Early Cretaceous ages that are localised along the CKFZ,

and therefore, suggests that the CKFZ was reactivated during the Early Cretaceous, recording rapid cooling in the vicinity of the fault at that time.

The mechanism of this cooling phase can be attributed to (1) extension in the Tethys Ocean (Zahirovic et al., 2016) or (2) collision of Lhasa with Eurasia (e.g. Brunet, Sobel, & McCann, 2017; Dumitru et al., 2001), as both events can be (partly) correlated in time to the recorded rapid Early Cretaceous cooling phase.

A compressional regime would require denudation after uplift to reset the fission track clock, inducing a significant time lag between uplift and AFT reset (Glorie & De Grave, 2016). In contrast, an extensional regime would rapidly reset the AFT ages in close vicinity to the fault. In the latter stress regime, rapid footwall exhumation occurs with respect to a rapidly subsiding hanging wall (Stockli, 2005; Stockli, Farley, & Dumitru, 2000).

Hence, this work suggests that the CKFZ was reactivated as a normal fault during the Early Cretaceous, recording a distal response to extensional tectonics in the Tethys Ocean at that time. This interpretation is in agreement with Jolivet et al. (2001), where reported AFT cooling ages along the Altyn-Tagh fault (a major structure in Central Asia in closer vicinity to the Lhasa terrane than the study area for this thesis) cannot be correlated with the Lhasa collision, suggesting that the Lhasa collision did not induce significant cooling and fault reactivation (Stockli, 2005; Stockli et al., 2000).

In addition, few Late Cretaceous AFT ages were obtained in this study. Samples displaying rapid cooling at that time are found in areas of higher relief, suggesting that these areas record a deeper level of the crust, where a younger thermal event may be recorded. The Late Cretaceous rapid cooling may be related to the Karakoram collision (Glorie & De Grave, 2016), although more data is required to confirm this theory.

## 5.5. Geographical age disparities

### 5.5.1. DZ-15 AND DZ-16

Samples DZ-15 and DZ-16 were taken in close vicinity to each other, on opposite sides of the shear zone and record vastly different AFT ages of  $265 \pm 11$  Ma and  $142 \pm 6$  Ma respectively (Figure 3). The disparity can be explained by either a difference in Cl concentration, which influences the annealing rate, or differential exhumation with respect to the fault. Firstly, looking at the Cl concentration of both samples (Table 3, Figure 16) reveals that there is a negligible difference that is likely not sufficient to differentially affect the annealing of the fission tracks between the two samples. Hence, sample DZ-16 records the fault reactivation during the Early Cretaceous while DZ-15 preserves an older thermo-tectonic event, indicating that the eastern side of the shear zone was tectonically stable at that time. Therefore, the disparity between the AFT ages of DZ-15 and DZ-16 can be explained by differential exhumation during fault reactivation.

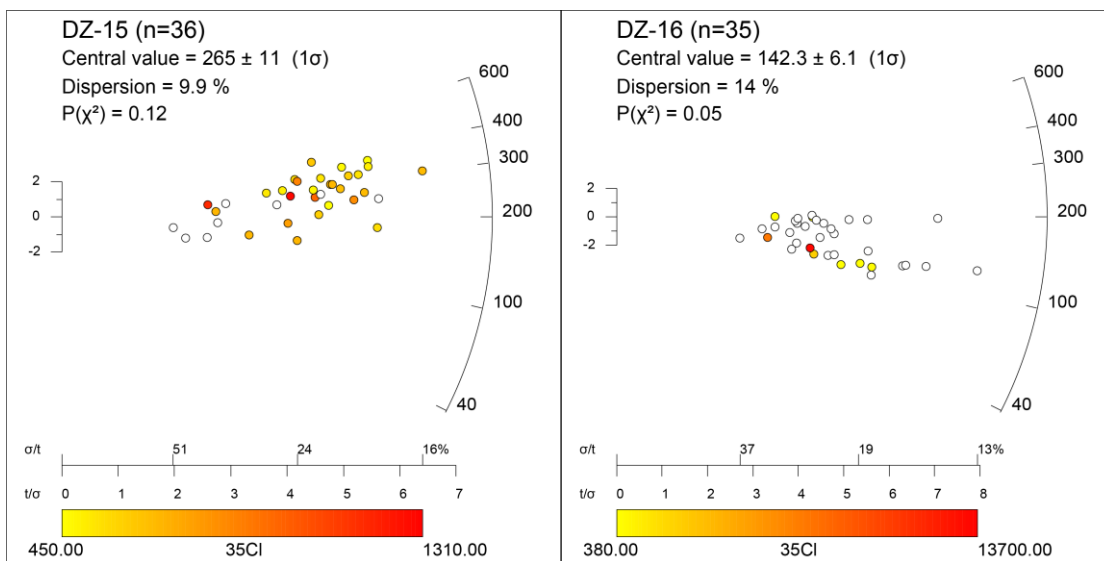


**Figure 16 – Radial plots of calculated AFT ages for samples DZ-15 and DZ-16 using RadialPlotter software (Vermeesch, 2009).** The coloured scale indicates the concentration of  $^{35}\text{Cl}$  in ppm within the analysed grains. White circles indicate grains with Cl concentrations below the limit of detection (LOD). The x-axis indicates the level of uncertainty in the single-grain ages and decreases from left to right. The curved y-axis to the right shows increasing age in Ma with the y-axis to the left representing  $2\sigma$  from the central age value.

### 5.5.2. DZ-22 AND DZ-23

Similarly to the case above, DZ-22 and DZ-23 record significantly different AFT ages of  $149 \pm 9$  Ma and  $264 \pm 13$  Ma respectively. Here, the disparity can be explained by the difference in Cl concentration between the samples. In Table 3 and Figure 17 it can be seen that DZ-23 contains higher concentrations of Cl, indicative of higher resistance to annealing (O'Sullivan & Parrish, 1995), and resulting in an older AFT age. Unlike with DZ-15 and DZ-16, there are no observed faults noted in the area from fieldwork or in literature. Therefore, the age disparity between DZ-22 and DZ-23 is likely to be solely caused by differences in Cl concentration.

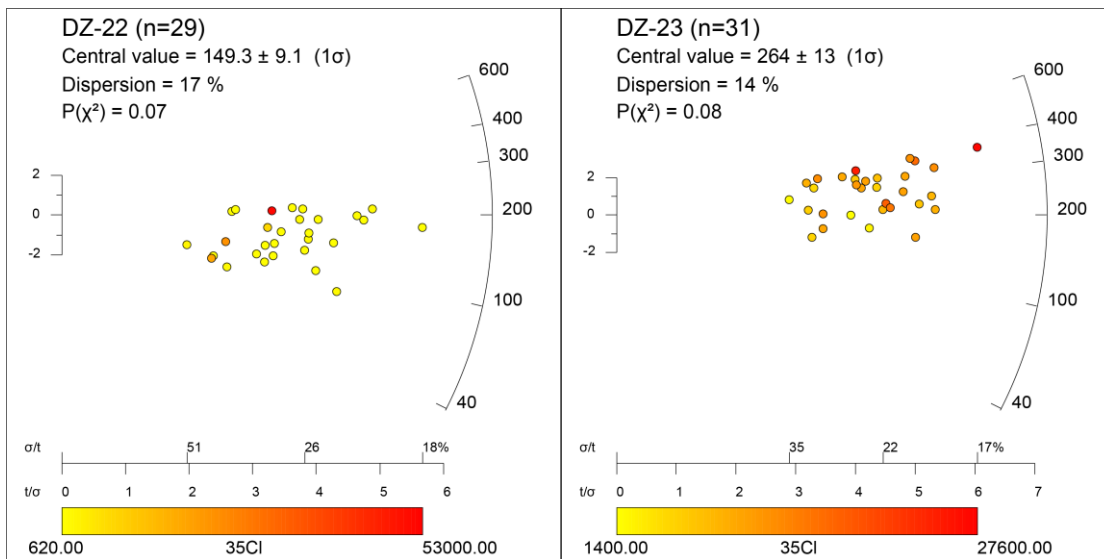


**Figure 17 – Radial plots of calculated AFT ages for samples DZ-22 and DZ-23 (caption as in Figure 16).**

### 5.5.3. DZ-06 AND DZ-07

Samples DZ-06 and DZ-07 record AFT ages of  $87 \pm 9$  Ma and  $143 \pm 8$  Ma respectively, both samples are found proximal to the CKFZ, but are located on the same side (unlike DZ-15 and DZ-16) (Figure 3). Differences in Cl concentration between the two samples are negligible (Figure 18) and, therefore, differential fission track annealing and

differential exhumation during fault reactivation are unlikely to have caused this age disparity. Instead, the disparity can be explained by differences in elevation as sample DZ-06 is found in an area of higher relief, suggesting exhumation from deeper depths (Glorie & De Grave, 2016).

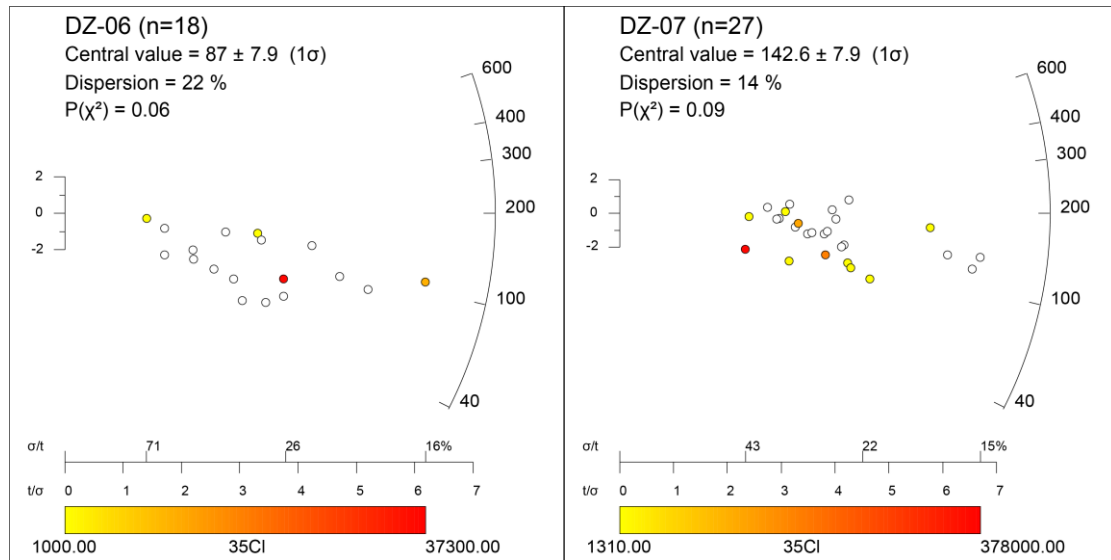


Figure 18 – Radial plots of calculated AFT ages for samples DZ-06 and DZ-07 (caption as in Figure 16)

## 5.6. Summary for the thermo-tectonic history of the Junggar Alatau

### 5.6.1. EARLY PERMIAN – EARLY TRIASSIC

The Early Permian-Early Triassic AU-Pb and AFT ages are interpreted in relation to granitoid emplacement and post-magmatic cooling in response to the closure of the PAO.

Published samples in the Tian Shan and neighbouring regions recording similar AFT ages are limited, likely as a result of deformation overprint in response to more recent thermo-tectonic events. Dumitru et al. (2001) and Song et al. (2018) reported latest Palaeozoic AFT ages at Aksu and along the Dushanzi-Kuqa highway in the Tian Shan (Dumitru et al., 2001), and in the southwestern Alxa Tectonic Belt (Song et al., 2018).

These AFT ages are similar to samples that are interpreted to record post-magmatic cooling due to the PAO closure in this study. Alternatively, cooling after regional heating associated with the Permian Tarim mantle plume was also suggested as a reason for the rapid cooling of emplaced granitoids (Song et al., 2018).

After the closure of the PAO, tectonic quiescence is recorded, indicated by shortening MTLs (Figure 15) until ~225 Ma.

#### 5.6.2. LATE TRIASSIC – EARLY JURASSIC REACTIVATION

The Late Triassic-Early Jurassic cooling event is interpreted to be in response to the accretion of the Qiangtang Block along the southern Eurasian margin. This is evidenced by the thermal history models for samples DZ-12, DZ-13, DZ-17, DZ-18, DZ-19 and DZ-20 recording cooling during the timeframe of the collision (Figures 11 and 13).

Increasing MTLs at ~230 Ma coincide with the beginning of the collision, suggesting enhanced exhumation at that time (Figure 15). Upper Triassic-Lower Jurassic conglomerate sediments were observed in both the Junggar and Tarim basins, indicating that the region underwent significant erosion following exhumation at that time (Choulet et al., 2013; Dumitru et al., 2001; Hendrix et al., 1992; Jolivet et al., 2010).

Similar conclusions were reached southwest of the study area in the Kyrgyz Tian Shan (De Grave et al., 2011) and western Tian Shan (Jepson et al., 2018).

Following the collision of the Qiangtang Block, an extensive peneplanation surface developed during the Late Jurassic period, suggesting a period of relative tectonic quiescence (Dumitru et al., 2001; Hendrix et al., 1992; Jolivet et al., 2010). The Jurassic AFT data in this study, associated with short MTLs, fit well with this period of no tectonic activity (Figure 15).

### 5.6.3. LATEST JURASSIC – EARLY CRETACEOUS REACTIVATION

The latest Jurassic-Early Cretaceous rapid cooling event is evidenced by central AFT ages and thermal history models in Group 2 (excluding sample DZ-06) and Group 3 (samples DZ-19, DZ-22 and DZ-25) (Table 3, Figures 12-13). Associated deposition of Lower Cretaceous conglomerates in the Junggar and Tarim basins (Dumitru et al., 2001; Hendrix et al., 1992; Jolivet et al., 2010), supports that rapid cooling can be linked to a period of exhumation at that time.

Major NW-SE orientated shear zones (Nachtergael et al., 2018) and other areas within the Tian Shan and neighbouring regions (e.g. Bullen et al., 2001; Glorie et al., 2011; Jepson et al., 2018; Macaulay et al., 2014) record similar AFT ages to the study area. Cooling signals within the Tian Shan are often linked to the Lhasa collision while not completely ruling out the MOOB. Alternatively, Jepson et al. (2018) instead attributed localised rapid cooling signals within the relict suture zones of the Kyzylum-Nurata Segment to be recording extension in response to slab-rollback of the subducting Tethys Ocean (Zahirovic et al., 2016). This work favours a similar interpretation for the localised Cretaceous cooling signals found along the CKFZ.

### 5.6.4. LATE CRETACEOUS REACTIVATION

De Pelsmaeker et al. (2015) interpreted Late Cretaceous-Palaeocene AFT ages within the Junggar Alatau to be related with the Lhasa collision. This suggests that there was a significant time-lag (~50–100 myr) between exhumation and the collision. However, as discussed above, the localised nature of the Early Cretaceous AFT data near the CKFZ favours a model of extension at that time. Hence it is unlikely that Late Cretaceous cooling is related to an event that occurred prior to Tethys extension, which is not recorded in the shear zone. Another interpretation by De Pelsmaeker et al. (2015) is that

exhumation was induced by the closure of the Mongol-Okhotsk Ocean, although, as pointed out by Jolivet et al. (2010), the Gobi Altai (east of the Tian Shan and more proximal to the MOOB) seems unaffected. Both the Gobi Altai and Tian Shan contain large scale NW-SE orientated shear zones, but if the Gobi Altai records no deformation as a result of the nearby closure then it is unlikely that the more distal Tian Shan would. AFT samples across the Kyrgyz Tian Shan (e.g. De Grave et al., 2013; Glorie & De Grave, 2016) and Chinese Tian Shan (e.g. Gillespie et al., 2017b; Jia, Fu, Jolivet, & Zheng, 2015; Wang, Li, & Du, 2009) were reported to record Late Cretaceous AFT ages. Samples located in the Chinese Northern Tian Shan (Wang et al., 2009) were interpreted to have exhumed in response to the Kohistan-Dras arc collision, while samples in the easternmost section of the Chinese Tian Shan (Gillespie et al., 2017a) were associated with ongoing tectonic processes following the formation of the MOOB. In the Kyrgyz Northern Tian Shan, De Grave et al. (2013) linked samples to be recording the far-field effects of the Karakoram collision. Hence, interpretations vary and more data is required to allow a more robust interpretation of the cause of the Late Cretaceous cooling.

## 6. CONCLUSIONS

AU-Pb and AFT results from the Junggar Alatau record post-magmatic cooling in the Permian-Triassic and at least two subsequent cooling periods during the Late Triassic and Early Cretaceous, with a potential cooling period in the Late Cretaceous.

1. Central AFT ages and thermal history modelling reflect post-magmatic cooling during the late Carboniferous-Late Permian (~320–250 Ma) linked to the closure of the Palaeo-Asian Ocean.

2. Central AFT ages and thermal history modelling evidenced renewed exhumation between the Late Triassic-Early Jurassic (~230–190 Ma) in response to the Qiangtang collision.
3. Central AFT ages and thermal history modelling suggest reactivation of shear zones in the Early Cretaceous, interpreted to be associated to extensional tectonics in response to the slab-rollback of the subducting Tethys Ocean (~150–120 Ma).
4. Central AFT ages suggest renewed tectonic activity in the Late Cretaceous (~80–70 Ma), although there is a lack of data to confirm and constraining the responsible thermo-tectonic event.

Cenozoic exhumation in response to the India-Eurasia collision is not constrained within this study, indicating that the extent of stress-field propagation through the crustal architecture has not reached the Junggar Alatau.

## 7. ACKNOWLEDGMENTS

Thank you to my supervisor Stijn Glorie and PhD students Gilby Jepson, Jack Gillespie, Angus Nixon, James Hall, Nick Fernie and Fan Yang for their assistance throughout the project. Juraj Farkas and Alec Walsh are thanked as well for supporting the entire honours cohort throughout the year. I would also like to thank Sarah Gilbert for her assistance with the LA-ICP-MS equipment and optical microscopes provided by Adelaide Microscopy.

## 8. REFERENCES

- AITCHISON, J. C., ALI, J. R., & DAVIS, A. M. (2007). When and where did India and Asia collide? *Journal of Geophysical Research*, 112(B5). doi:10.1029/2006jb004706
- BRUNET, M. F., SOBEL, E. R., & MCCANN, T. (2017). Geological evolution of Central Asian Basins and the western Tien Shan Range. *Geological Society, London, Special Publications*, 427(1), 1-17. doi:10.1144/sp427.17
- BULLEN, M. E., BURBANK, D. W., GARVER, J. I., & ABDRAKHMATOV, K. Y. (2001). Late Cenozoic tectonic evolution of the northwestern Tien Shan: New age estimates for the initiation of mountain building. *Geological Society of America Bulletin*, 113(12), 1544-1559. doi:10.1130/0016-7606(2001)113<1544:1cteot>2.0.co;2

- CHEW, D. M., PETRUS, J. A., & KAMBER, B. S. (2014). U-Pb LA-ICPMS dating using accessory mineral standards with variable common Pb. *Chemical Geology*, 363, 185-199. doi:10.1016/j.chemgeo.2013.11.006
- CHEW, D. M., & SPIKINGS, R. A. (2015). Geochronology and thermochronology using apatite: time and temperature, lower crust to surface. *Elements*, 11(3), 189-194. doi:10.2113/gselements.11.3.189
- CHOULET, F., CHEN, Y., COGNE, J. P., RABILLARD, A., WANG, B., LIN, W., FAURE, M., & CLUZEL, D. (2013). First Triassic palaeomagnetic constraints from Junggar (NW China) and their implications for the Mesozoic tectonics in Central Asia. *Journal of Asian Earth Sciences*, 78, 371-394. doi:10.1016/j.jseaes.2013.01.023
- CHOULET, F., FAURE, M., CLUZEL, D., CHEN, Y., LIN, W., & WANG, B. (2012). From oblique accretion to transpression in the evolution of the Altai collage: new insights from West Junggar, northwestern China. *Gondwana Research*, 21(2-3), 530-547. doi:10.1016/j.gr.2011.07.015
- DE GRAVE, J., BUSLOV, M. M., & VAN DEN HAUTE, P. (2007). Distant effects of India-Eurasia convergence and Mesozoic intracontinental deformation in Central Asia: Constraints from apatite fission-track thermochronology. *Journal of Asian Earth Sciences*, 29(2-3), 188-204. doi:10.1016/j.jseaes.2006.03.001
- DE GRAVE, J., GLORIE, S., BUSLOV, M. M., IZMER, A., FOURNIER-CARRIE, A., BATALEV, V. Y., VANHAECKE, F., ELBURG, M., & VAN DEN HAUTE, P. (2011). The thermo-tectonic history of the Song-Kul plateau, Kyrgyz Tien Shan: Constraints by apatite and titanite thermochronometry and zircon U/Pb dating. *Gondwana Research*, 20(4), 745-763. doi:10.1016/j.gr.2011.03.011
- DE GRAVE, J., GLORIE, S., BUSLOV, M. M., STOCKLI, D. F., MCWILLIAMS, M. O., BATALEV, V. Y., & VAN DEN HAUTE, P. (2013). Thermo-tectonic history of the Issyk-Kul basement (Kyrgyz Northern Tien Shan, Central Asia). *Gondwana Research*, 23(3), 998-1020. doi:10.1016/j.gr.2012.06.014
- DE PELSMAEKER, E., GLORIE, S., BUSLOV, M. M., ZHIMULEV, F. I., POUJOL, M., KOROBKIN, V. V., VANHAECKE, F., VETROV, E. V., & DE GRAVE, J. (2015). Late-Paleozoic emplacement and Meso-Cenozoic reactivation of the southern Kazakhstan granitoid basement. *Tectonophysics*, 662, 416-433. doi:10.1016/j.tecto.2015.06.014
- DE PELSMAEKER, E., JOLIVET, M., LABORDE, A., POUJOL, M., ROBIN, C., ZHIMULEV, F. I., NACHTERGAELE, S., GLORIE, S., DE CLERCQ, S., BATALEV, V. Y., & DE GRAVE, J. (2018). Source-to-sink dynamics in the Kyrgyz Tien Shan from the Jurassic to the Paleogene: Insights from sedimentological and detrital zircon U-Pb analyses. *Gondwana Research*, 54, 180-204. doi:10.1016/j.gr.2017.09.004
- DUMITRU, T. A., ZHOU, D., CHANG, E. Z., GRAHAM, S. A., HENDRIX, M. S., SOBEL, E. R., & CARROLL, A. R. (2001). Uplift, exhumation, and deformation in the Chinese Tian Shan. *Geological Society of America, Memoir* 194, 71-99. doi:10.1130/0-8137-1194-0.71
- GALBRAITH, R. F., & LASLETT, G. M. (1993). Statistical models for mixed fission track ages. *Nuclear Tracks and Radiation Measurements*, 21(4), 459-470. doi:10.1016/1359-0189(93)90185-C
- GALLAGHER, K. (2012). Transdimensional inverse thermal history modeling for quantitative thermochronology. *Journal of Geophysical Research: Solid Earth*, 117(B2). doi:10.1029/2011jb008825
- GALLAGHER, K., BROWN, R., & JOHNSON, C. (1998). Fission track analysis and its applications to geological problems. *Annual Review of Earth and Planetary Sciences*, 26(1), 519-572. doi:10.1146/annurev.earth.26.1.519
- GAO, L., ZHANG, C., SHI, X., SONG, B., WANG, Z., & LIU, Y. (2008). Mesoproterozoic age for Xiamaling Formation in North China Plate indicated by zircon SHRIMP dating. *Chinese Science Bulletin*, 53(17), 2665-2671. doi:10.1007/s11434-008-0340-3
- GILLESPIE, J., GLORIE, S., JEPSON, G., ZHANG, Z. Y., XIAO, W. J., DANIŠÍK, M., & COLLINS, A. S. (2017a). Differential Exhumation and Crustal Tilting in the Easternmost Tianshan (Xinjiang, China), Revealed by Low-Temperature Thermochronology. *Tectonics*, 36(10), 2142-2158. doi:10.1002/2017tc004574
- GILLESPIE, J., GLORIE, S., XIAO, W., ZHANG, Z., COLLINS, A. S., EVANS, N., MCINNES, B., & DE GRAVE, J. (2017b). Mesozoic reactivation of the Beishan, southern Central Asian Orogenic Belt: Insights from low-temperature thermochronology. *Gondwana Research*, 43, 107-122. doi:10.1016/j.gr.2015.10.004
- GLEADOW, A. J. W., DUDDY, I. R., GREEN, P. F., & HEGARTY, K. A. (1986a). Fission track lengths in the apatite annealing zone and the interpretation of mixed ages. *Earth and Planetary Science Letters*, 78(2-3), 245-254. doi:10.1016/0012-821X(86)90065-8

- GLEADOW, A. J. W., DUDDY, I. R., GREEN, P. F., & LOVERING, J. F. (1986b). Confined fission track lengths in apatite: a diagnostic tool for thermal history analysis. *Contributions to Mineral and Petrology*, 94(4), 405-415. doi:10.1007/BF00376334
- GLORIE, S., & DE GRAVE, J. (2016). Exhuming the Meso-Cenozoic Kyrgyz Tianshan and Siberian Altai-Sayan: a review based on low-temperature thermochronology. *Geoscience Frontiers*, 7(2), 155-170. doi:10.1016/j.gsf.2015.04.003
- GLORIE, S., DE GRAVE, J., BUSLOV, M. M., ZHIMULEV, F. I., STOCKLI, D. F., BATALEV, V. Y., IZMER, A., VAN DEN HAUTE, P., VANHAECKE, F., & ELBURG, M. A. (2011). Tectonic history of the Kyrgyz South Tien Shan (Atbashi-Inylchek) suture zone: The role of inherited structures during deformation-propagation. *Tectonics*, 30(6). doi:10.1029/2011tc002949
- GLORIE, S., DE GRAVE, J., DELVAUX, D., BUSLOV, M. M., ZHIMULEV, F. I., VANHAECKE, F., ELBURG, M. A., & VAN DEN HAUTE, P. (2012). Tectonic history of the Irtysh shear zone (NE Kazakhstan): New constraints from zircon U/Pb dating, apatite fission track dating and palaeostress analysis. *Journal of Asian Earth Sciences*, 45, 138-149. doi:10.1016/j.jseas.2011.09.024
- GREEN, P. F. (1986). On the thermo-tectonic evolution of Northern England: evidence from fission track analysis. *Geological Magazine*, 123(5), 493-506. doi:10.1017/s0016756800035081
- GREEN, P. F., DUDDY, I. R., GLEADOW, A. J. W., TINGATE, P. R., & LASLETT, G. M. (1986). Thermal annealing of fission tracks in apatite: 1. A qualitative description. *Chemical Geology*, 59, 237-253. doi:10.1016/0168-9622(86)90074-6
- HAN, Y., & ZHAO, G. (2017). Final amalgamation of the Tianshan and Junggar orogenic collage in the southwestern Central Asian Orogenic Belt: Constraints on the closure of the Paleo-Asian Ocean. *Earth-Science Reviews*. doi:10.1016/j.earscirev.2017.09.012
- HENDRIKS, B. W. H., & REDFIELD, T. F. (2005). Apatite fission track and (U-Th)/He data from Fennoscandia: An example of underestimation of fission track annealing in apatite. *Earth and Planetary Science Letters*, 236(1-2), 443-458. doi:10.1016/j.epsl.2005.05.027
- HENDRIX, M. S., DUMITRU, T. A., & GRAHAM, S. A. (1994). Late Oligocene-early Miocene unroofing in the Chinese Tian Shan: An early effect of the India-Asia collision. *Geology*, 22(6), 487-490. doi:10.1130/0091-7613(1994)022<0487:LOEMUI>2.3.CO;2
- HENDRIX, M. S., GRAHAM, S. A., CARROLL, A. R., SOBEL, E., MCKNIGHT, C. L., SCHULEIN, B. J., & WANG, Z. (1992). Sedimentary record and climatic implications of recurrent deformation in the Tian Shan: Evidence from Mesozoic strata of the north Tarim, south Junggar, and Turpan basins, northwest China. *Geological Society of America Bulletin*, 104(1), 53-79. doi:10.1130/0016-7606(1992)104<0053:SRACIO>2.3.CO;2
- HUANG, H., CAWOOD, P. A., NI, S., HOU, M., SHI, Z., & HU, X. (2017). Provenance of late Paleozoic strata in the Yili Basin: Implications for tectonic evolution of the South Tianshan orogenic belt. *GSA Bulletin*, 130(5-6), 952-974. doi:10.1130/b31588.1
- JEPSON, G., GLORIE, S., KONOPELKO, D., MIRKAMALOV, R., DANÍŠÍK, M., & COLLINS, A. S. (2018). The low-temperature thermo-tectonic evolution of the western Tian Shan, Uzbekistan. *Gondwana Research*, 64, 122-136. doi:10.1016/j.gr.2018.08.003
- JIA, Y., FU, B., JOLIVET, M., & ZHENG, S. (2015). Cenozoic tectono-geomorphological growth of the SW Chinese Tian Shan: Insight from AFT and detrital zircon U-Pb data. *Journal of Asian Earth Sciences*, 111, 395-413. doi:10.1016/j.jseas.2015.06.023
- JIAN, W., XIANHUA, L., TAIZHONG, D., DUNYI, L., BIAO, S., ZHONGXIONG, L., & YONGHUA, G. (2003). Zircon SHRIMP U-Pb dating for the Cangshuiyu volcanic rocks and its implications for the lower boundary age of the Nanhua strata in South China. *Chinese Science Bulletin*, 48(16), 1663-1669. doi:10.1360/03wd0168
- JOLIVET, M., BRUNEL, M., SEWARD, D., XU, Z., YANG, J., ROGER, F., TAPPONNIER, P., MALAVIEILLE, J., ARNAUD, N., & WU, C. (2001). Mesozoic and Cenozoic tectonics of the northern edge of the Tibetan plateau: fission-track constraints. *Tectonophysics*, 343(1-2), 111-134. doi:10.1016/S0040-1951(01)00196-2
- JOLIVET, M., DE BOISGROLLIER, T., PETIT, C., FOURNIER, M., SANKOV, V. A., RINGENBACH, J. C., BYZOV, L., MIROSHNICHENKO, A. I., KOVALENKO, S. N., & ANISIMOVA, S. V. (2009). How old is the Baikal Rift Zone? Insight from apatite fission track thermochronology. *Tectonics*, 28(3). doi:10.1029/2008tc002404
- JOLIVET, M., DOMINGUEZ, S., CHARREAU, J., CHEN, Y., LI, Y., & WANG, Q. (2010). Mesozoic and Cenozoic tectonic history of the central Chinese Tian Shan: Reactivated tectonic structures and active deformation. *Tectonics*, 29(6). doi:10.1029/2010tc002712

- KOROBKIN, V. V., & BUSLOV, M. M. (2011). Tectonics and geodynamics of the western Central Asian Fold Belt (Kazakhstan Paleozoides). *Russian Geology and Geophysics*, 52(12), 1600-1618. doi:10.1016/j.rgg.2011.11.011
- KRÖNER, A., ALEXEIEV, D. V., KOVACH, V. P., ROJAS-AGRAMONTE, Y., TRETYAKOV, A. A., MIKOŁAICHUK, A. V., XIE, H., & SOBEL, E. R. (2017). Zircon ages, geochemistry and Nd isotopic systematics for the Palaeoproterozoic 2.3–1.8 Ga Kuilyu Complex, East Kyrgyzstan – The oldest continental basement fragment in the Tianshan orogenic belt. *Journal of Asian Earth Sciences*, 135, 122-135. doi:10.1016/j.jseas.2016.12.022
- LEE, J. K. W., WILLIAMS, I. S., & ELLIS, D. J. (1997). Pb, U and Th diffusion in natural zircon. *Nature*, 390(6656), 159–162.
- LI, P., SUN, M., ROSENBAUM, G., YUAN, C., SAFONOVA, I., CAI, K., JIANG, Y., & ZHANG, Y. (2018). Geometry, kinematics and tectonic models of the Kazakhstan Orocline, Central Asian Orogenic Belt. *Journal of Asian Earth Sciences*, 153, 42-56. doi:10.1016/j.jseas.2017.07.029
- MACAULAY, E. A., SOBEL, E. R., MIKOŁAICHUK, A., KOHN, B., & STUART, F. M. (2014). Cenozoic deformation and exhumation history of the Central Kyrgyz Tien Shan. *Tectonics*, 33(2), 135-165. doi:10.1002/2013tc003376
- MCDOWELL, F. W., MCINTOSH, W. C., & FARLEY, K. A. (2005). A precise 40Ar–39Ar reference age for the Durango apatite (U–Th)/He and fission-track dating standard. *Chemical Geology*, 214(3-4), 249-263. doi:10.1016/j.chemgeo.2004.10.002
- METELKIN, D. V., VERNIKOVSKY, V. A., & KAZANSKY, A. Y. (2012). Tectonic evolution of the Siberian paleocontinent from the Neoproterozoic to the Late Mesozoic: paleomagnetic record and reconstructions. *Russian Geology and Geophysics*, 53(7), 675-688. doi:10.1016/j.rgg.2012.05.006
- METELKIN, D. V., VERNIKOVSKY, V. A., KAZANSKY, A. Y., & WINGATE, M. T. D. (2010). Late Mesozoic tectonics of Central Asia based on paleomagnetic evidence. *Gondwana Research*, 18(2-3), 400-419. doi:10.1016/j.gr.2009.12.008
- NACHTERGAELE, S., DE PELSMAEKER, E., GLORIE, S., ZHIMULEV, F., JOLIVET, M., DANIŠÍK, M., BUSLOV, M. M., & DE GRAVE, J. (2018). Meso-Cenozoic tectonic evolution of the Talas-Fergana region of the Kyrgyz Tien Shan revealed by low-temperature basement and detrital thermochronology. *Geoscience Frontiers*, 9(5), 1495-1514. doi:10.1016/j.gsf.2017.11.007
- O'SULLIVAN, P. B., & PARRISH, R. R. (1995). The importance of apatite composition and single-grain ages when interpreting fission track data from plutonic rocks: a case study from the Coast Ranges, British Columbia. *Earth and Planetary Science Letters*, 132(1-4), 213-224. doi:10.1016/0012-821X(95)00058-K
- PATON, C., HELLSTROM, J., PAUL, B., WOODHEAD, J., & HERGT, J. (2011). Iolite: Freeware for the visualisation and processing of mass spectrometric data. *Journal of Analytical Atomic Spectrometry*, 26(12), 2508-2518. doi:10.1039/c1ja10172b
- PETROV, O., POSPELOV, I. I., SHOKALSKY, S., TOLMACHEVA, T. Y., & KASHUBIN, S. (2016). *Atlas of geological maps of Asia and adjacent areas*. In (pp. 48).
- SOBEL, E. R., CHEN, J., & HEERMANCE, R. V. (2006). Late Oligocene–Early Miocene initiation of shortening in the Southwestern Chinese Tian Shan: Implications for Neogene shortening rate variations. *Earth and Planetary Science Letters*, 247(1-2), 70-81. doi:10.1016/j.epsl.2006.03.048
- SOBEL, E. R., & DUMITRU, T. A. (1997). Thrusting and exhumation around the margins of the western Tarim basin during the India-Asia collision. *Journal of Geophysical Research-Solid Earth*, 102(B3), 5043-5063. doi:10.1029/96jb03267
- SONG, D., GLORIE, S., XIAO, W., COLLINS, A. S., GILLESPIE, J., JEPSON, G., & LI, Y. (2018). Tectono-thermal evolution of the southwestern Alxa Tectonic Belt, NW China: Constrained by apatite U-Pb and fission track thermochronology. *Tectonophysics*, 722, 577-594. doi:10.1016/j.tecto.2017.11.029
- STOCKLI, D. F. (2005). Application of low-temperature thermochronometry to extensional tectonic settings. *Reviews in Mineralogy and Geochemistry*, 58(1), 411-448. doi:10.2138/rmg.2005.58.16
- STOCKLI, D. F., FARLEY, K. A., & DUMITRU, T. A. (2000). Calibration of the apatite (U-Th)/He thermochronometer on an exhumed fault block, White Mountains, California. *Geology*, 28(11), 983-986. doi:10.1130/0091-7613(2000)28<983:COTAHT>2.0.CO;2
- VAN HINSBERGEN, D. J., LIPPERT, P. C., DUPONT-NIVET, G., MCQUARRIE, N., DOUBROVINE, P. V., SPAKMAN, W., & TORSVIK, T. H. (2012). Greater India Basin hypothesis and a two-stage Cenozoic collision between India and Asia. *Proceedings of the National Academy of Sciences*, 109(20), 7659-7664. doi:10.1073/pnas.1117262109

- VERMEESCH, P. (2009). Radialplotter: a Java application for fission track, luminescence and other radial plots. *Radiation Measurements*, 44(4), 409-410. doi:doi.org/10.1016/j.radmeas.2009.05.003
- VERMEESCH, P. (2017). Statistics for LA-ICP-MS based fission track dating. *Chemical Geology*, 456, 19-27. doi:10.1016/j.chemgeo.2017.03.002
- WAGNER, G. A., GLEADOW, A. J. W., & FITZGERALD, P. G. (1989). The significance of the partial annealing zone in apatite fission-track analysis: Projected track length measurements and uplift chronology of the Transantarctic Mountains. *Chemical Geoscience*, 79(4), 295-305. doi:10.1016/0168-9622(89)90035-3
- WANG, Q., LI, S., & DU, Z. (2009). Differential uplift of the Chinese Tianshan since the Cretaceous: constraints from sedimentary petrography and apatite fission-track dating. *International Journal of Earth Sciences*, 98(6), 1341-1363. doi:10.1007/s00531-009-0436-2
- WANG, X., CAI, K., SUN, M., XIAO, W., XIA, X., WAN, B., BAO, Z., & WANG, Y. (2018). Two contrasting late Paleozoic magmatic episodes in the northwestern Chinese Tianshan Belt, NW China: Implication for tectonic transition from plate convergence to intra-plate adjustment during accretionary orogenesis. *Journal of Asian Earth Sciences*, 153, 118-138. doi:10.1016/j.jseaes.2017.03.013
- WINDLEY, B. F., ALEXEIEV, D., XIAO, W., KROENER, A., & BADARACH, G. (2007). Tectonic models for accretion of the Central Asian Orogenic Belt. *Journal of the Geological Society*, 164(1), 31-47. doi:10.1144/0016-76492006-022
- XIAO, W., WINDLEY, B. F., HAN, C., LIU, W., WAN, B., ZHANG, J. E., AO, S., ZHANG, Z., & SONG, D. (2017). Late Paleozoic to early Triassic multiple roll-back and orocinal bending of the Mongolia collage in Central Asia. *Earth-Science Reviews*. doi:10.1016/j.earscirev.2017.09.020
- ZAHIROVIC, S., MATTHEWS, K. J., FLAMENT, N., MÜLLER, R. D., HILL, K. C., SETON, M., & GURNIS, M. (2016). Tectonic evolution and deep mantle structure of the eastern Tethys since the latest Jurassic. *Earth-Science Reviews*, 162, 293-337. doi:10.1016/j.earscirev.2016.09.005
- ZHANG, Z., ZHU, W., ZHENG, D., ZHENG, B., & YANG, W. (2016). Apatite fission track thermochronology in the Kuluketage and Aksu areas, NW China: Implication for tectonic evolution of the northern Tarim. *Geoscience Frontiers*, 7(2), 171-180. doi:10.1016/j.gsf.2015.08.007
- ZHAO, L., & HE, G. (2013). Tectonic entities connection between West Junggar (NW China) and East Kazakhstan. *Journal of Asian Earth Sciences*, 72, 25-32. doi:10.1016/j.jseaes.2012.08.004
- ZHU, X., WANG, B., CHEN, Y., LIU, H., HORNG, C.-S., CHOULET, F., FAURE, M., SHU, L., & XUE, Z. (2018). First Early Permian Paleomagnetic Pole for the Yili Block and its Implications for Late Paleozoic Postorogenic Kinematic Evolution of the SW Central Asian Orogenic Belt. *Tectonics*, 37(6), 1709-1732. doi:10.1029/2017tc004642

## 9. APPENDIX A: EXTENDED METHODS

### 9.1 Laboratory processing

The separation and crushing of samples was performed at the Institute of Geology and Geophysics, Chinese Academy of Sciences (IGGCAS) following standard procedures.

Apatite grains were picked onto double sided tape under two Olympus SZ61 microscopes with magnifications of x45. Depending on grain availability, rasters of 115-200 grains were picked for each sample and positioned in a way so that the c-axis of the grain was parallel to the surface.

The mounting of grains involved an EpoxyCure resin mixture with a ratio of 5g epoxy resin to 1.15g epoxy hardener being poured onto the tape until all the grains were covered. Clean thin section slides of ~30x30mm with bevelled edges were placed on top of the resin with a gap equal to the thickness of one thin section slide between the two slides. The resin was left to dry for 3 days ensuring that the grains were embedded into the mount. Using a razor blade the double side tape was removed and cleaned from the mount with ethanol.

Exposing the internals of the grains was completed by grinding the mounts on wet #2000 silicon carbide paper. Applying even pressure onto the mount the sample was grinded in a figure-eight pattern until the top 8 $\mu$ m of each grain was removed.

To create a smooth surface for fission track analysis grain were polished using a Struers TegraPol. Grains were first polished using 3 $\mu$ m diamond suspension fluid combined with a 3 $\mu$ m polishing cloth. Followed by further, finer polishing using 1 $\mu$ m diamond suspension fluid combined with a 1 $\mu$ m polishing cloth. At first each sample was polished for 10 minutes with the 3 $\mu$ m diamond suspension fluid and polishing cloth after which samples would be checked under the Zeiss AXIO Imager M2m Autoscan

System for sufficient polishing. Samples deemed to not be sufficiently polished because of blemishes and scratches were polished again in 3 minute sets until sufficiently polished. This process was then repeated with the finer 1 $\mu\text{m}$  diamond suspension fluid and polishing cloth.

Etching of the grains is done to reveal the natural fission tracks formed by fission reactions. Samples were etched with 5M nitric acid ( $\text{HNO}_3$ ) at  $20\pm0.5^\circ\text{C}$  for  $20\pm0.5$  seconds, then washed in deionised water to prevent any further etching by residual acid. After etching, grains were examined under a Zeiss AXIO Imager M2m Autoscan System to determine whether the etching process successfully revealed the natural fission tracks. Following successful etching, the mounts were coated with a 3nm layer of gold to aid in the imaging of grains.

## 9.2 Fission track counting

Apatite grains were imaged with a Zeiss AXIO Imager M2m Autoscan System at a magnification of x1000 using FastTracks software. Grains with a width of at least 30 $\mu\text{m}$  were selected for imaging and further analysis. In each sample a minimum of 20 grains were imaged depending on the availability of grains present in each mount with the target being 40 grains. Using TrackWorks software, region of interests (ROIs) were defined on imaged grains. The ROI defines the region on the grain that will be used for track density calculations and the area in which laser ablation will be conducted. Fission tracks were counted within the ROI to calculate the fission track density and coupled with  $^{238}\text{U}$  concentrations for apatite fission track age calculations.

For modelling purposes, confined fission tracks (fission tracks that do not penetrate the surface of the grain) were measured using TrackWorks software. Confined fission track lengths can be used to model the timing of passage through the partial annealing zone

(APAZ) that occurs between temperatures of ~60–120°C (Wagner et al., 1989). The measuring of these lengths can be conducted on all apatite grains present in the sample, not just those that were imaged. A minimum of 30 lengths per sample is required for acceptable modelling of the samples thermal history, with 100 lengths being the target. Confined fission tracks are revealed when etching acid enters through an intersecting fission track (TINTs) or grain cracks/cleavages (TINCLEs) (Gleadow et al., 1986b).

### **9.3 LA-ICP-MS analysis**

‘Unknown’ grains (apatite grains to be analysed) were analysed by laser ablation inductively coupled plasma mass spectrometry (LA-ICP-MS) for elemental concentrations (e.g. U, Pb and Cl) using a solid state New Wave-213 laser coupled with an Agilent 7900x mass spectrometer (analytical details in Table 1). A laser diameter of 30µm was used in grain ablation, care was taken to avoid areas of heterogeneity in fission track densities. Laser ablation sessions were set up to analyse a block of standards before every block of ten unknown grains. Standard blocks contained two NIST 610 standards, two Madagascar apatite standards, one Durango apatite standard, and one McClure apatite standard.

### **9.4 Data reduction**

Iolite software was used for the process of data reduction (Paton, Hellstrom, Paul, Woodhead & Hergt, 2011) with Madagascar apatite used as the primary standard in U–Pb analysis and NIST 610 as the primary standard in AFT analysis. Secondary standards of Durango and McClure apatite were both used to test the accuracy of the analysed data. Apatite fission track ages were calculated with  $^{238}\text{U}$  concentrations and fission track densities for each grain using in-house Excel spreadsheets, following

methodology outlined in Gillespie et al. (2017b) and Glorie et al. (2017). Analysis of the Durango apatite standards were conducted in the same session as the unknown samples. Using the  $^{238}\text{U}$  concentrations of Durango apatite standards and calculating fission track densities, a zeta calibration factor was produced for unknown samples (Vermeesch, 2009, 2017). The zeta calibration factor overcomes the uncertainties of fission track analysis (Hasebe et al., 2004) by comparing the data of unknown grains to a known standard, Durango apatite in this case.

*AFT Age Equation* (Hasebe et al., 2004)

$$t = \frac{1}{\lambda_D} \ln\left(1 + \frac{\lambda_D \rho_s M}{\lambda_f N_A^{238} U 10^{-6} d R_{sp} k}\right)$$

Where  $\lambda_D$  =  $^{238}\text{U}$  total decay constant ( $1.55.125 \times 10^{-10} \text{ a}^{-1}$ ),  $\lambda_f$  =  $^{238}\text{U}$  spontaneous fission decay constant ( $8.46 \times 10^{-17} \text{ a}^{-1}$ ),  $N_A$  = Avogadro's number ( $6.02214 \times 10^{23} \text{ mol}^{-1}$ ),  $d$  = apatite density ( $3.19 \text{ g/cm}^2$  as in Hasebe et al. (2004)),  $M$  = atomic mass of  $^{238}\text{U}$  (238.0508 amu),  $k$  = observational parameter = 1 (constant),  $^{238}\text{U}$  is the samples measured  $^{238}\text{U}$  concentration ( $\mu\text{g/g}$ ),  $\rho_s$  = spontaneous fission track density ( $\text{tracks/cm}^2$ ), and  $R_{sp}$  = the registration factor, corresponding to the range or to half the measured mean confined fission track length.

## 9.5 Modelling

RadialPlotter software (Vermeesch, 2009, 2017) was used to determine the central AFT ages of samples by inputting single-grain AFT ages and associated AFT age uncertainties. Samples that pass the chi-squared ( $\chi^2$ ) test with a value of  $>0.05$  (O'Sullivan & Parrish, 1995) and record a single-grain age dispersion of  $<25\%$  are regarded as a single population and display homogeneity. Meanwhile, samples that fail the  $\chi^2$  or record a single-grain age dispersion of  $>25\%$  are considered to display

heterogeneity (Galbraith & Laslett, 1993) and potentially contain multiple populations.

To distinguish multiple populations present in a sample an automatic mixture model in RadialPlotter was used to statistically define the age populations.

Thermal history modelling of samples was conducted with QTQt software developed by (Gallagher, 2012). Inputs used for modelling involved single-grain AFT ages and the uncertainty associated with the grain age, the number of counted fission tracks, the weight percent (wt%) of chlorine within the grain, confined fission track lengths, the length of the etch pits and the angle of the lengths to the C-axis. Basement samples were constrained below the APAZ with associated AU–Pb ages at temperatures of  $400\pm50^{\circ}\text{C}$  to model the passage of the rock through the APAZ. (Meta)sedimentary samples were constrained to present day temperatures at  $22.5\pm2.5^{\circ}\text{C}$  with the depositional age of the formation. Modelling was first conducted by running 10,000 possible models (10,000 Burn-in and 10,000 Post-Burn-in) as a test run to determine the plausibility of the thermal history model. Statistically acceptable models were then refined by running an extra 200,000 possible models (200,000 Burn-in and 200,000 Post-Burn-in).

## 10. APPENDIX B: AFT DATA TABLE

**Table 5 – Single-grain AFT data used in this study for all sample.**  $\rho_s$  represents the average density of spontaneous fission tracks. Ns represents the number of tracks counted for each grain.  $^{35}\text{Cl}$  and  $^{238}\text{U}$  represent the average concentrations in grains analysed with  $1\sigma$  as the reported uncertainty. t represents the single-grain AFT age with  $1\sigma$  as the reported uncertainty, as calculated by in house Excel spreadsheets (e.g. Gillespie et al., 2017b; Glorie et al., 2017)

Grain	$\rho_s$ ( $\times 10^5/\text{cm}^2$ )	Ns	Cl (ppm)	$1\sigma$ (ppm)	U (ppm)	$1\sigma$ (ppm)	t (Ma)	$1\sigma$ (Ma)
DZ-01_1.d	5.511	10	5020	870	5.1	0.36	226.652395	73.939483
DZ-01_2.d	6.649	27	3110	700	5.44	0.34	256.364276	52.777914
DZ-01_3.d	7.723	19	3520	770	7.12	0.5	227.512947	55.263912
DZ-01_4.d	8.394	22	3940	650	5.87	0.53	299.937618	70.3711761
DZ-01_5.d	7.361	6	4070	670	6.29	0.31	245.463118	101.366202
DZ-01_7.d	15.45	19	3130	650	10.92	0.8	296.76038	72.3499792
DZ-01_12.d	4.761	6	44100	6800	5.47	0.41	182.56223	76.0923898
DZ-01_13.d	3.01	4	4620	710	4.56	0.36	138.452796	70.2806057
DZ-01_14.d	2.178	2	5360	830	3.15	0.19	145.026512	103.068627
DZ-01_15.d	9.323	12	2130	580	9.15	0.58	213.714833	63.6823087
DZ-01_16.d	7.205	10	3320	870	6.1	0.59	247.744616	82.4637981
DZ-01_17.d	5.772	10	6000	1100	5.29	0.46	228.860439	75.5589346
DZ-01_19.d	7.689	19	3410	650	6.35	0.45	253.978065	61.7397017
DZ-01_20.d	4.906	9	2950	730	4.31	0.35	238.753832	82.4116178
DZ-01_21.d	5.82	14	5010	850	7.61	0.65	160.412574	45.417897
DZ-01_22.d	7.885	17	3060	740	4.22	0.34	391.912682	101.257936
DZ-01_23.d	7.051	13	5330	840	4.83	0.38	306.198922	89.036158
DZ-01_24.d	9.564	23	2340	680	17	2.3	118.002369	29.6705573
DZ-01_25.d	5.163	9	5200	1100	2.44	0.25	443.82562	155.686318
DZ-01_26.d	8.863	12	3670	880	9.94	0.78	187.022751	56.3961192
DZ-01_27.d	8.76	20	4230	830	6.23	0.43	294.928087	69.9193399
DZ-01_28.d	7.946	9	6060	970	8.51	0.71	195.847972	67.7054619
DZ-01_30.d	5.103	9	2530	570	3.1	0.2	345.274055	117.956924
DZ-01_31.d	6.918	10	3020	790	6.31	0.49	229.959457	75.3866292
DZ-01_32.d	8.209	21	5100	1000	4.25	0.36	405.136521	96.0725767
DZ-01_33.d	8.017	15	4700	1000	5.39	0.54	311.97744	87.2105571
DZ-01_34.d	7.359	9	2950	900	6	0.42	257.257253	88.1648053
DZ-01_35.d	4.184	5	4400	1000	4.93	0.54	178.010178	82.2393676
DZ-01_36.d	6.358	15	2570	730	4	0.35	333.396169	91.7672022
DZ-01_37.d	6.329	6	3550	780	3.9	0.39	340.385115	143.651455
DZ-01_38.d	8.823	7	489000	88000	9	3	205.624021	103.918024
DZ-01_39.d	40.68	63	3210	970	60	4.3	142.209881	21.3071118
DZ-01_44.d	8.083	7	4010	680	8.77	0.56	193.318343	74.4649544
DZ-01_45.d	6.422	6	5360	880	6.53	0.34	206.280034	85.2556083
DZ-01_46.d	8.936	8	4300	1400	5.86	0.43	319.849456	116.129557
DZ-01_48.d	10.73	13	3380	690	6.48	0.47	347.315998	100.435773
DZ-01_51.d	9.72	8	9000	1200	8.29	0.62	245.93017	89.3619927
Grain	$\rho_s$	Ns	Cl (ppm)	$1\sigma$ (ppm)	U (ppm)	$1\sigma$ (ppm)	t (Ma)	$1\sigma$ (Ma)

	(x10 <sup>5</sup> /cm <sup>2</sup> )							
DZ-02_2.d	4.662	16	5320	760	2.94	0.25	332.627728	88.7376187
DZ-02_5.d	3.487	4	8800	1900	2.39	0.19	306.046599	155.379894
DZ-02_6.d	6.678	12	5740	670	4.55	0.29	307.87082	91.7615865
DZ-02_7.d	1.643	3	5800	1100	1.58	0.16	218.129292	128.127072
DZ-02_8.d	5.558	4	104000	15000	3.15	0.35	370.1191	190.093245
DZ-02_9.d	4.9	9	11100	1500	4.26	0.23	241.279261	81.9872427
DZ-02_10.d	2.488	2	6420	730	3.04	0.31	171.676285	122.822129
DZ-02_14.d	4.526	9	8400	1800	5.25	0.81	180.837611	66.7765214
DZ-02_15.d	2.156	3	5140	970	2.79	0.32	162.098153	95.6142585
DZ-02_17.d	2.707	4	5090	730	2.28	0.22	249.050215	127.174231
DZ-02_18.d	4.819	8	5360	730	2.5	0.21	404.343462	147.735111
DZ-02_19.d	5.781	8	600000	200000	5.5	2.5	220.482332	127.241624
DZ-02_21.d	4.948	5	5650	820	3.21	0.24	323.339058	147.12087
DZ-02_22.d	4.831	9	7800	1000	4.05	0.35	250.21626	86.684308
DZ-02_27.d	3.819	6	4950	550	3.93	0.3	203.840568	85.0123497
DZ-02_28.d	2.964	4	5520	830	2.14	0.17	290.534651	147.501809
DZ-02_29.d	2.799	3	11100	2400	3.58	0.34	164.003602	96.1615813
DZ-02_30.d	1.807	3	4460	750	1.75	0.15	216.597588	126.690106
DZ-02_33.d	4.104	6	5900	780	2.83	0.24	304.19665	127.362948
DZ-02_34.d	5.005	5	6420	900	4.4	0.32	238.607954	108.488912
DZ-02_35.d	5.122	5	5580	980	3.97	0.31	270.63414	123.290666
DZ-02_41.d	4.598	3	17400	3400	4.24	0.25	227.476546	132.298562
DZ-02_56.d	1.524	1	5250	640	3.02	0.27	105.85504	106.35311
DZ-02_59.d	4.656	7	6330	780	3.37	0.26	289.812145	112.336871
Grain	$\rho_s$ (x10 <sup>5</sup> /cm <sup>2</sup> )	Ns	Cl (ppm)	1 $\sigma$ (ppm)	U (ppm)	1 $\sigma$ (ppm)	t (Ma)	1 $\sigma$ (Ma)
DZ-03_1.d	10.23	37	1190	520	22.1	1.4	97.0969824	17.4988968
DZ-03_2.d	15.11	61	Below LOD	Below LOD	18.87	0.92	167.963508	23.8779776
DZ-03_4.d	12.57	38	Below LOD	Below LOD	15.48	0.88	170.328252	29.983058
DZ-03_5.d	10.42	40	Below LOD	Below LOD	17.06	0.9	128.11827	21.9013225
DZ-03_6.d	8.143	22	Below LOD	Below LOD	18.6	1.2	91.8319625	20.7500345
DZ-03_7.d	3.671	11	Below LOD	Below LOD	9.12	0.54	84.4329411	26.1407534
DZ-03_8.d	6.648	18	1620	750	9.77	0.53	142.731168	34.943744
DZ-03_9.d	21.02	41	1050	610	56.1	2.9	78.5945128	13.2687332
DZ-03_11.d	4.972	12	2100	760	6.57	0.48	158.740637	47.6514156
DZ-03_12.d	5.513	36	Below LOD	Below LOD	14.6	1.3	79.2058959	15.2655029
DZ-03_14.d	5.845	19	Below LOD	Below LOD	10.76	0.74	113.944828	27.6303469
DZ-03_15.d	10.45	45	Below LOD	Below LOD	13.12	0.65	167.072443	26.99975
DZ-03_17.d	15.23	38	4000	1200	32.8	2.1	97.397639	17.3833377
DZ-03_18.d	9.136	15	Below LOD	Below LOD	22.1	1.1	86.7133953	23.0376432
DZ-03_19.d	4.661	12	Below LOD	Below LOD	10.9	0.67	89.6963922	26.6914409
DZ-03_20.d	12.85	54	Below LOD	Below LOD	22.3	1.4	120.870588	18.685894
DZ-03_22.d	10.41	13	4800	1500	13.7	1.2	159.386866	46.7508587
DZ-03_23.d	7.088	37	Below LOD	Below LOD	16.1	1.5	92.3464504	17.7983832
DZ-03_24.d	10.63	38	Below LOD	Below LOD	13.91	0.75	160.298149	28.0693164

DZ-03_25.d	9.688	27	Below LOD	Below LOD	12.44	0.63	163.356387	33.0937828
DZ-03_26.d	15.59	25	Below LOD	Below LOD	27.9	1.7	117.209896	24.9059826
DZ-03_27.d	8.85	40	Below LOD	Below LOD	12.18	0.62	152.411716	25.9684782
DZ-03_28.d	6.334	11	Below LOD	Below LOD	10.93	0.67	121.557082	37.6839054
DZ-03_29.d	6.639	18	Below LOD	Below LOD	10.19	0.72	136.66297	34.0253829
DZ-03_30.d	5.146	9	1080	560	13.48	0.95	80.0759801	27.4506833
DZ-03_31.d	11.99	41	1820	590	21.1	1.2	119.195292	20.3206698
DZ-03_32.d	9.617	27	1790	910	20.9	1.5	96.5196421	20.16025
DZ-03_33.d	5.972	8	Below LOD	Below LOD	9.34	0.69	134.12054	48.7094199
DZ-03_34.d	16.36	76	1460	690	23.1	1.4	148.557195	20.0802297
DZ-03_35.d	14.12	34	Below LOD	Below LOD	25.9	1.6	114.355566	21.2921151
DZ-03_36.d	15.88	28	Below LOD	Below LOD	25.3	2.3	131.659544	28.0586968
DZ-03_37.d	6.491	7	Below LOD	Below LOD	10.36	0.7	131.423862	50.7067956
DZ-03_38.d	9.207	35	Below LOD	Below LOD	13.39	0.9	144.231439	26.8009366
DZ-03_39.d	3.573	9	Below LOD	Below LOD	6.15	0.35	121.86536	41.4681542
DZ-03_40.d	13.8	43	Below LOD	Below LOD	26.5	2.6	109.233433	20.2366563
DZ-03_41.d	10.48	34	Below LOD	Below LOD	22.4	1.3	98.1376455	18.1539791
DZ-03_43.d	6.427	20	Below LOD	Below LOD	13.53	0.7	99.6398064	23.1790967
DZ-03_44.d	9.165	32	Below LOD	Below LOD	16.42	0.78	117.079724	21.8867167
DZ-03_46.d	14.39	36	1420	670	24.6	1.2	122.700987	21.8107019
Grain	$\rho_s$ ( $\times 10^5/\text{cm}^2$ )	Ns	Cl (ppm)	$1\sigma$ (ppm)	U (ppm)	$1\sigma$ (ppm)	t (Ma)	$1\sigma$ (Ma)
DZ-04_1.d	6.137	8	Below LOD	Below LOD	7.45	0.48	172.78257	62.4390062
DZ-04_2.d	9.061	41	1370	520	6.07	0.45	313.103204	55.4163902
DZ-04_3.d	7.353	7	4200	1800	10.21	0.97	151.056321	59.1482557
DZ-04_4.d	5.916	9	1250	640	5.83	0.37	212.843155	72.6722674
DZ-04_5.d	6.641	14	1680	730	6.61	0.49	210.73278	58.9913797
DZ-04_6.d	8.878	14	1050	680	6.54	0.63	284.732778	81.6084006
DZ-04_7.d	8.691	19	1110	550	5.42	0.3	336.333816	80.3934596
DZ-04_8.d	8.935	21	1220	520	8.67	0.48	216.160102	49.3506517
DZ-04_9.d	4.895	11	2740	840	6.25	0.43	164.275484	51.184936
DZ-04_12.d	6.72	14	Below LOD	Below LOD	6.52	0.34	216.183106	59.4355724
DZ-04_13.d	11.14	14	1570	480	8.16	0.47	286.348627	79.0371996
DZ-04_14.d	4.956	14	Below LOD	Below LOD	5.62	0.31	184.967343	50.9620124
DZ-04_15.d	9.363	20	Below LOD	Below LOD	7.19	0.52	273.140567	65.0224075
DZ-04_16.d	5.587	12	1030	560	7.35	0.63	159.437844	48.3913592
DZ-04_19.d	8.067	20	5400	4300	6.98	0.77	242.413449	61.1386384
DZ-04_21.d	6.231	7	39600	8800	9.87	0.63	132.416064	51.0052648
DZ-04_23.d	12.01	17	Below LOD	Below LOD	15.3	1.2	164.646178	42.4309848
DZ-04_24.d	7.24	13	1030	480	6.62	0.45	229.39326	66.0809014
DZ-04_25.d	10.35	33	Below LOD	Below LOD	10.23	0.7	212.209486	40.5007053
DZ-04_26.d	9.389	22	Below LOD	Below LOD	8.55	0.63	230.331482	52.6867343
DZ-04_27.d	4.884	8	Below LOD	Below LOD	4.69	0.39	218.425273	79.7639198
DZ-04_29.d	9.548	12	1100	530	6.16	0.41	325.111081	97.100427
DZ-04_30.d	6.618	15	Below LOD	Below LOD	5.85	0.38	237.285376	63.8141531
DZ-04_31.d	3.677	5	Below LOD	Below LOD	7.27	0.39	106.0863	47.9525671

DZ-04_35.d	7.967	14	Below LOD	Below LOD	7.62	0.33	219.300651	59.9551965
DZ-04_36.d	6.07	7	Below LOD	Below LOD	7.03	0.34	181.106252	69.3510977
DZ-04_37.d	7.329	11	1110	670	4.27	0.27	360.011952	111.74695
DZ-04_40.d	4.403	11	Below LOD	Below LOD	4.72	0.27	195.662124	60.503845
DZ-04_42.d	2.747	5	Below LOD	Below LOD	3.17	0.18	181.760486	82.2280353
DZ-04_44.d	4.913	12	Below LOD	Below LOD	5.53	0.31	186.346702	55.2527585
DZ-04_45.d	7.894	9	Below LOD	Below LOD	7.93	0.51	208.796883	71.323845
DZ-04_46.d	5.054	8	Below LOD	Below LOD	8.51	0.93	124.567789	46.3389345
Grain	$\rho_s$ ( $\times 10^5/\text{cm}^2$ )	Ns	Cl (ppm)	$1\sigma$ (ppm)	U (ppm)	$1\sigma$ (ppm)	t (Ma)	$1\sigma$ (Ma)
DZ-05_1.d	13	31	11380	910	8.4	0.5	324.620009	62.6446307
DZ-05_3.d	5.408	38	10000	1000	3.34	0.32	339.626395	65.2706154
DZ-05_4.d	7.655	39	11900	1600	8.52	0.86	188.458975	36.3824394
DZ-05_5.d	8.878	21	15300	1600	5.47	0.4	340.438785	79.4076454
DZ-05_6.d	13.53	72	12100	1100	8.37	0.5	339.065465	46.6099821
DZ-05_7.d	11.71	41	9600	1100	11.4	0.94	215.458318	38.9191626
DZ-05_8.d	9.471	51	8600	1100	9.97	0.71	199.256227	32.2023692
DZ-05_9.d	12.31	50	10400	1000	8.64	0.53	298.851562	47.4434788
DZ-05_10.d	15.42	52	12300	1200	12.19	0.81	265.333379	42.0246406
DZ-05_11.d	5.216	22	10500	1300	4.95	0.4	221.026123	51.0871573
DZ-05_12.d	5.155	30	14800	1600	4.22	0.28	256.228503	50.7146324
DZ-05_13.d	11.75	44	13130	930	7.17	0.47	343.739887	57.9929896
DZ-05_14.d	12.28	33	8500	1100	10.24	0.91	251.541492	50.0813355
DZ-05_15.d	9.431	28	10000	1200	6.45	0.43	306.696804	62.5527826
DZ-05_17.d	15.12	56	7710	960	14.54	0.73	218.121567	32.2180467
DZ-05_20.d	6.091	16	10100	1000	5.05	0.28	252.992963	65.4922996
DZ-05_21.d	19.51	43	11000	1100	21.9	1.9	186.863457	33.5430339
DZ-05_22.d	14.27	43	7600	1100	12.88	0.76	232.391015	39.0091965
DZ-05_23.d	9.497	22	9610	740	9.53	0.57	209.028141	46.9599328
DZ-05_24.d	7.884	36	7850	870	7.72	0.55	214.210392	39.6682188
DZ-05_25.d	11.22	39	6640	840	7.32	0.55	321.508897	58.1620415
DZ-05_27.d	13.15	18	14600	1800	10.02	0.76	275.276573	68.9555519
DZ-05_28.d	6.555	13	6540	900	4.45	0.32	308.9754	89.3006434
DZ-05_29.d	8.353	11	5750	830	11.14	0.85	157.278195	49.2786792
DZ-05_30.d	8.328	25	9500	1100	6.39	0.51	273.370143	59.7734178
DZ-05_32.d	8.714	60	12400	1400	10.44	0.77	175.076671	26.8649588
DZ-05_33.d	14.55	15	9900	1200	13.9	0.98	219.563131	59.3539353
DZ-05_35.d	14.17	24	10800	1400	12.01	0.88	247.478835	54.4875025
DZ-05_37.d	11.6	32	11900	1100	10.21	0.69	238.31066	45.9986842
DZ-05_38.d	8.945	25	7700	1000	11.78	0.74	159.27451	33.9316897
DZ-05_41.d	11.64	13	10400	1100	9.63	0.67	253.534997	73.1320563
DZ-05_42.d	10.79	24	9600	1200	11.53	0.82	196.292343	43.0789228
Grain	$\rho_s$ ( $\times 10^5/\text{cm}^2$ )	Ns	Cl (ppm)	$1\sigma$ (ppm)	U (ppm)	$1\sigma$ (ppm)	t (Ma)	$1\sigma$ (Ma)
DZ-06_1.d	1.932	9	Below LOD	Below LOD	6.98	0.57	58.0625848	20.0479324
DZ-06_2.d	27.61	46	12800	3800	53.1	2.9	109.072822	17.6419359
DZ-06_3.d	7.276	25	Below LOD	Below LOD	15.81	0.93	96.5395972	20.4563052

DZ-06_4.d	2.016	2	1000	450	2.57	0.19	164.551583	117.156235
DZ-06_5.d	4.235	5	Below LOD	Below LOD	13.71	0.82	64.7978543	29.3396763
DZ-06_6.d	3.399	5	Below LOD	Below LOD	8.84	0.62	80.6572782	36.6399404
DZ-06_7.d	5.421	8	Below LOD	Below LOD	8.18	0.57	139.017914	50.372675
DZ-06_8.d	5.863	7	Below LOD	Below LOD	20.2	1.8	60.8854033	23.7560013
DZ-06_10.d	1.654	3	Below LOD	Below LOD	2.79	0.2	124.35864	72.5034874
DZ-06_11.d	10.61	15	Below LOD	Below LOD	37.1	2	59.9910055	15.9864795
DZ-06_12.d	18.68	34	Below LOD	Below LOD	43.5	3.4	90.0808096	17.3181112
DZ-06_13.d	2.366	3	Below LOD	Below LOD	9.2	0.67	53.9475319	31.4600833
DZ-06_16.d	7.266	20	Below LOD	Below LOD	11.48	0.75	132.769453	31.3368628
DZ-06_17.d	5.283	10	Below LOD	Below LOD	26.3	2.1	42.1375745	13.8359661
DZ-06_18.d	5.244	15	37300	5800	14.3	0.74	76.9256735	20.4662831
DZ-06_21.d	2.933	12	1110	460	4.25	0.34	144.766406	43.7119819
DZ-06_24.d	7.1	13	Below LOD	Below LOD	30.4	2.3	48.9924811	14.2066948
DZ-06_28.d	7.685	12	Below LOD	Below LOD	12.31	0.67	130.957532	38.7897791
Grain	$\rho_s$ ( $\times 10^5/\text{cm}^2$ )	Ns	Cl (ppm)	$1\sigma$ (ppm)	U (ppm)	$1\sigma$ (ppm)	t (Ma)	$1\sigma$ (Ma)
DZ-07_1.d	14.69	54	Below LOD	Below LOD	22.7	1.1	135.746755	20.2741321
DZ-07_2.d	6.299	10	Below LOD	Below LOD	7.3	0.81	181.001537	61.0464733
DZ-07_4.d	18.4	19	197000	37000	36.7	4.4	105.168403	27.5141374
DZ-07_6.d	13.76	8	Below LOD	Below LOD	12.52	0.95	230.540707	83.8220939
DZ-07_10.d	10.92	20	1980	720	22.9	1.5	100.027789	23.6137683
DZ-07_11.d	6.365	11	11400	2100	16.3	1.5	81.9113947	26.0082671
DZ-07_12.d	5.8	19	Below LOD	Below LOD	9.49	0.57	128.202147	30.7895174
DZ-07_13.d	11.64	16	Below LOD	Below LOD	16.7	1.2	146.207626	38.4342049
DZ-07_15.d	52.43	54	Below LOD	Below LOD	91	5.3	120.857049	18.4678556
DZ-07_17.d	4.295	9	Below LOD	Below LOD	5	0.34	180.188338	61.6798662
DZ-07_18.d	11.78	13	Below LOD	Below LOD	17.4	1	142.013477	40.5834451
DZ-07_19.d	3.97	14	Below LOD	Below LOD	5.69	0.42	146.356413	40.9579739
DZ-07_20.d	7.717	12	Below LOD	Below LOD	10.36	0.98	156.250803	47.8344327
DZ-07_21.d	23.75	32	1880	600	57.3	6.7	86.9445793	18.7207151
DZ-07_22.d	14.34	39	1800	670	17.32	0.93	173.673989	30.0630056
DZ-07_24.d	17.47	21	6400	1700	38.8	2.8	94.4484201	22.0018844
DZ-07_25.d	6.02	11	Below LOD	Below LOD	5.31	0.46	237.812941	75.1478229
DZ-07_27.d	4.775	16	Below LOD	Below LOD	6.56	0.36	152.687349	39.5077125
DZ-07_28.d	9.755	12	139000	23000	12.14	0.92	168.555179	50.7112528
DZ-07_29.d	8.592	19	Below LOD	Below LOD	14.46	0.99	124.640589	30.2130662
DZ-07_30.d	7.094	44	Below LOD	Below LOD	11.08	0.58	134.302761	22.0301267
DZ-07_32.d	5.649	10	1310	570	5.73	0.34	206.799967	66.9981947
DZ-07_34.d	13.64	6	378000	40000	35.3	4.3	81.0537636	34.6683323
DZ-07_38.d	25.11	18	Below LOD	Below LOD	28.5	2	184.814213	45.9885349
DZ-07_39.d	23.26	24	Below LOD	Below LOD	20.1	2.2	242.743253	56.9728598
DZ-07_41.d	10.74	17	Below LOD	Below LOD	10.59	0.64	212.736414	53.7829186
DZ-07_43.d	4.023	6	1530	460	4.56	0.31	185.062619	76.9130069
Grain	$\rho_s$ ( $\times 10^5/\text{cm}^2$ )	Ns	Cl (ppm)	$1\sigma$ (ppm)	U (ppm)	$1\sigma$ (ppm)	t (Ma)	$1\sigma$ (Ma)
DZ-08_1.d	9.268	23	4000	1300	15.43	0.8	124.68933	27.8292739

DZ-08_2.d	5.885	25	1380	430	5.2	0.38	234.937484	51.9988054
DZ-08_3.d	9.552	31	Below LOD	Below LOD	16.63	0.97	119.23706	23.6399803
DZ-08_5.d	4.269	15	1130	590	5.81	0.79	152.531386	45.4538622
DZ-08_6.d	18	55	2140	770	27	1.2	138.394215	21.3522282
DZ-08_7.d	2.447	8	Below LOD	Below LOD	3.65	0.26	139.171496	50.892074
DZ-08_8.d	5.543	20	Below LOD	Below LOD	9.18	0.58	125.346263	30.0932134
DZ-08_9.d	2.881	15	Below LOD	Below LOD	2.53	0.19	236.391539	65.1486693
DZ-08_10.d	3.753	10	Below LOD	Below LOD	3.15	0.18	247.33023	80.8706358
DZ-08_12.d	6.485	15	170000	140000	11.4	8	118.090326	88.5892182
DZ-08_13.d	4.882	9	900	360	4.34	0.34	233.516319	81.1936379
DZ-08_15.d	10.86	60	Below LOD	Below LOD	16.6	1.1	135.809745	21.3461773
DZ-08_16.d	5.44	18	1310	490	4.95	0.39	228.140764	58.3478605
DZ-08_17.d	15.19	56	870	380	25.1	1.1	125.629968	19.2278103
DZ-08_18.d	6.096	24	1310	480	6.35	0.49	199.287667	45.1236147
DZ-08_20.d	5.251	13	1360	390	3.81	0.34	286.105517	85.1295194
DZ-08_21.d	14.31	25	1460	590	27.2	2.3	109.214405	24.6149743
DZ-08_22.d	1.37	3	Below LOD	Below LOD	2.63	0.2	108.136924	63.3098218
DZ-08_23.d	2.563	6	Below LOD	Below LOD	1.91	0.16	278.56364	117.305039
DZ-08_24.d	4.423	12	Below LOD	Below LOD	5.29	0.3	173.56832	52.1272654
DZ-08_26.d	10.98	18	1840	410	17.7	1	128.776989	32.167036
DZ-08_27.d	6.407	18	Below LOD	Below LOD	5.11	0.37	260.281328	66.075193
DZ-08_28.d	6.434	15	Below LOD	Below LOD	10.93	0.74	122.199685	33.4428515
DZ-08_30.d	4.348	6	Below LOD	Below LOD	5.42	0.45	166.532669	70.103501
DZ-08_32.d	10.64	13	890	440	9.64	0.76	229.125689	67.4989813
DZ-08_33.d	6.801	16	Below LOD	Below LOD	9.01	0.67	156.695736	41.9513395
DZ-08_35.d	8.00E+00	16	740	440	9.43	0.59	176.111407	46.6151441
DZ-08_38.d	5.045	8	4500	1600	4.54	0.72	230.682426	90.4668688
DZ-08_40.d	9.948	19	760	320	12.66	0.82	163.121521	40.1138865
DZ-08_41.d	5.828	16	Below LOD	Below LOD	4.82	0.3	251.004609	66.4194458
DZ-08_42.d	1.803	4	Below LOD	Below LOD	2.7	0.19	138.624871	70.4943786
Grain	$\rho_s$ ( $\times 10^5/\text{cm}^2$ )	Ns	Cl (ppm)	$1\sigma$ (ppm)	U (ppm)	$1\sigma$ (ppm)	t (Ma)	$1\sigma$ (Ma)
DZ-09_1.d	27.65	51	Below LOD	Below LOD	43.4	2.1	132.265317	21.1608211
DZ-09_2.d	23.57	44	Below LOD	Below LOD	30.1	1.5	162.567474	27.6161862
DZ-09_3.d	11.48	18	950	410	20.1	1.1	118.573162	29.571451
DZ-09_4.d	17.2	33	8200	3500	34.2	2.2	104.410196	20.3768365
DZ-09_5.d	9.839	15	Below LOD	Below LOD	17.8	1.1	114.754977	31.2446703
DZ-09_6.d	10.55	23	910	330	11.7	0.8	187.20057	42.6063112
DZ-09_7.d	13.58	40	Below LOD	Below LOD	15.3	1.3	184.26757	34.8973534
DZ-09_8.d	7.248	16	980	420	19.05	0.95	78.9884833	20.6934445
DZ-09_9.d	25.86	46	810	360	41.7	2.6	128.745789	22.0277878
DZ-09_10.d	13.15	57	1600	730	22.1	1.7	123.530457	20.338652
DZ-09_13.d	21.78	45	1010	400	34.9	2.3	129.56062	22.5198106
DZ-09_15.d	14.7	27	Below LOD	Below LOD	32.6	2	93.6138931	19.7362699
DZ-09_17.d	16.97	34	1270	450	41	2.7	85.9287623	16.6168036
DZ-09_18.d	18.36	66	1390	520	36.6	2	104.143498	15.3711263

DZ-09_19.d	32.14	41	620	310	81.4	4	81.9713414	14.3043846
DZ-09_20.d	17.85	20	960	300	26.6	1.3	139.314767	32.9783076
DZ-09_21.d	15.61	29	1010	420	23.4	1.2	138.492934	27.9603172
DZ-09_22.d	22.63	44	Below LOD	Below LOD	43.4	2.6	108.251868	18.7382464
DZ-09_23.d	8.054	23	Below LOD	Below LOD	17.98	0.95	92.9956236	20.7771575
DZ-09_24.d	20.35	58	Below LOD	Below LOD	40.5	2	104.315769	15.932312
DZ-09_25.d	22.98	38	Below LOD	Below LOD	42	2	113.590315	20.3926305
DZ-09_26.d	17.74	55	740	280	33.2	2.4	110.93181	18.2463248
DZ-09_27.d	4.373	19	580	300	6.37	0.38	142.521575	34.863107
DZ-09_28.d	8.051	27	1100	340	17.3	1	96.6149413	20.2719193
DZ-09_29.d	6.857	32	910	390	7.69	0.75	185.117884	39.01065
DZ-09_30.d	2.512	5	800	420	6.54	0.43	79.7411433	36.3649222
DZ-09_31.d	14.17	48	Below LOD	Below LOD	22.1	1.5	133.112287	22.702191
DZ-09_32.d	10.11	18	Below LOD	Below LOD	11.17	0.84	187.905092	47.8541237
DZ-09_33.d	20.53	16	337000	74000	21.7	5.5	196.412799	70.9229617
DZ-09_34.d	18.18	22	1290	310	25.5	1.9	148.011094	34.6020561
DZ-09_35.d	20.95	31	Below LOD	Below LOD	45.6	3.6	95.3805351	19.5791996
DZ-09_36.d	18.92	36	Below LOD	Below LOD	36.4	2.4	107.909659	20.4094745
DZ-09_37.d	25.48	76	Below LOD	Below LOD	43	2.9	123.018815	17.9764134
DZ-09_38.d	6.621	32	Below LOD	Below LOD	11.25	0.82	122.18324	24.5006168
DZ-09_39.d	10.29	35	780	300	13.1	1.3	163.073972	33.446564
DZ-09_40.d	14.25	22	660	420	36.4	2.4	81.2744527	18.789829
DZ-09_41.d	8.667	20	Below LOD	Below LOD	10.88	0.81	165.379041	40.2348843
DZ-09_42.d	15.66	41	42400	7600	27.4	1.2	118.653831	20.5360967
DZ-09_44.d	19.23	31	1730	470	43.6	3	91.5658153	18.4589547
Grain	$\rho_s$ ( $\times 10^5/\text{cm}^2$ )	Ns	Cl (ppm)	$1\sigma$ (ppm)	U (ppm)	$1\sigma$ (ppm)	t (Ma)	$1\sigma$ (Ma)
DZ-10_1.d	11.51	62	Below LOD	Below LOD	25.8	1.5	92.5980947	14.0907857
DZ-10_2.d	4.961	31	740	380	10.53	0.83	97.7883889	20.0687762
DZ-10_3.d	7.193	23	Below LOD	Below LOD	14.07	0.71	106.111487	23.6491968
DZ-10_4.d	12.98	49	Below LOD	Below LOD	25.4	1.4	106.068741	17.4588889
DZ-10_5.d	5.85	42	Below LOD	Below LOD	8.4	0.45	144.551637	25.1728831
DZ-10_6.d	3.565	14	Below LOD	Below LOD	6.78	0.44	109.138072	30.7310546
DZ-10_7.d	4.578	20	Below LOD	Below LOD	8.84	0.52	107.490469	25.6871002
DZ-10_8.d	5.711	26	570	300	6.85	0.38	173.048573	36.7848777
DZ-10_9.d	6.598	20	Below LOD	Below LOD	8.63	0.47	158.689412	37.7577207
DZ-10_10.d	4.422	9	Below LOD	Below LOD	6.91	0.38	132.827233	45.5855295
DZ-10_11.d	6.733	32	560	310	11.1	1.1	125.901838	26.6238606
DZ-10_12.d	6.053	16	Below LOD	Below LOD	6.49	0.36	193.585316	50.9331119
DZ-10_13.d	2.798	30	10600	1600	4.13	0.21	140.619028	27.9707146
DZ-10_14.d	5.495	14	Below LOD	Below LOD	7.26	0.46	157.100479	44.1813035
DZ-10_15.d	8.282	30	Below LOD	Below LOD	16.37	0.97	105.010562	21.1307155
DZ-10_16.d	8.305	32	Below LOD	Below LOD	8.28	0.5	208.188019	40.8724762
DZ-10_17.d	4.785	25	Below LOD	Below LOD	7.88	0.42	126.038191	27.175116
DZ-10_18.d	5.174	14	Below LOD	Below LOD	10.71	0.74	100.272856	28.3347575
DZ-10_19.d	2.285	17	Below LOD	Below LOD	3.2	0.24	148.211758	38.6760109

DZ-10_20.d	2.307	9	Below LOD	Below LOD	5.01	0.36	95.5776405	33.0982137
DZ-10_21.d	2.909	22	Below LOD	Below LOD	5.5	0.36	109.781072	25.3653088
DZ-10_23.d	5.243	22	980	450	7.33	0.48	148.464396	34.3044812
DZ-10_24.d	2.635	7	Below LOD	Below LOD	5.92	0.34	92.3858265	35.7573177
DZ-10_25.d	4.922	9	650	220	8.13	0.36	125.660129	42.9306899
DZ-10_26.d	8.25	21	Below LOD	Below LOD	15.82	0.73	108.241526	25.0118128
DZ-10_27.d	4.094	33	Below LOD	Below LOD	4.27	0.26	199.006104	38.6182224
DZ-10_28.d	4.961	23	Below LOD	Below LOD	8.2	0.48	125.574602	28.2338241
DZ-10_29.d	5.245	28	Below LOD	Below LOD	6.42	0.32	169.573076	34.6882209
DZ-10_30.d	1.845	4	Below LOD	Below LOD	3.29	0.24	116.398373	59.2338923
DZ-10_31.d	3.987	12	Below LOD	Below LOD	3.91	0.22	211.648849	63.5461719
DZ-10_32.d	2.153	7	7900	1600	3.65	0.32	122.432749	48.0757562
DZ-10_33.d	2.391	24	Below LOD	Below LOD	3.04	0.22	163.249714	36.7042451
DZ-10_34.d	3.586	21	Below LOD	Below LOD	3.65	0.25	203.921893	48.2383131
DZ-10_35.d	2.631	18	Below LOD	Below LOD	3.15	0.24	173.363125	44.2016324
DZ-10_37.d	4.497	21	Below LOD	Below LOD	4.7	0.26	198.596441	46.2888073
DZ-10_38.d	3.467	12	14900	2900	3.86	0.21	186.428785	55.9100065
DZ-10_39.d	5.354	23	145000	18000	12.9	1.5	86.1459946	21.2146634
DZ-10_40.d	4.319	27	Below LOD	Below LOD	6.79	0.49	132.026122	28.2831039
DZ-10_41.d	3.59	25	Below LOD	Below LOD	3.91	0.26	190.574208	41.7825639
DZ-10_42.d	4.238	10	Below LOD	Below LOD	9.17	0.59	95.926379	31.4934611
Grain	$\rho_s$ ( $\times 10^5/\text{cm}^2$ )	Ns	Cl (ppm)	$1\sigma$ (ppm)	U (ppm)	$1\sigma$ (ppm)	t (Ma)	$1\sigma$ (Ma)
DZ-11_1.d	1.303	3	740	540	2.74	0.25	97.0883468	56.9969045
DZ-11_3.d	6.809	20	18800	4000	6.85	0.53	202.939233	49.2813745
DZ-11_4.d	14.08	97	Below LOD	Below LOD	19.1	1.2	150.502093	19.7613356
DZ-11_5.d	7.402	14	8700	2100	13.8	1.1	109.507345	31.1213145
DZ-11_6.d	5.685	16	Below LOD	Below LOD	7.74	0.41	149.955625	39.1868957
DZ-11_7.d	8.629	21	810	320	13.04	0.57	135.100244	30.9593712
DZ-11_8.d	14.36	63	Below LOD	Below LOD	18.1	1.1	161.975422	24.3234559
DZ-11_9.d	9.212	28	Below LOD	Below LOD	19.12	0.89	98.3647057	19.8844882
DZ-11_10.d	10.36	55	Below LOD	Below LOD	22.2	1.5	95.2752362	15.2830099
DZ-11_11.d	4.584	15	Below LOD	Below LOD	8.33	0.59	112.349944	30.6999563
DZ-11_12.d	16.73	40	Below LOD	Below LOD	35.7	2.8	95.6755534	17.6767798
DZ-11_13.d	6.766	12	Below LOD	Below LOD	10.39	0.79	132.950416	40.3474327
DZ-11_15.d	7.193	33	Below LOD	Below LOD	15.1	1.2	97.2537527	19.3538415
DZ-11_16.d	7.16	37	Below LOD	Below LOD	15.1	1.1	96.8075722	18.1930458
DZ-11_17.d	9.037	34	Below LOD	Below LOD	14.03	0.97	131.504274	25.3553183
DZ-11_18.d	9.095	31	Below LOD	Below LOD	9.07	0.62	204.723957	40.9010813
DZ-11_19.d	10.48	35	3200	1500	22.2	1.9	96.3788104	19.0040317
DZ-11_20.d	5.321	22	Below LOD	Below LOD	8.14	0.41	133.45723	30.1316175
DZ-11_21.d	5.864	47	1940	450	9.94	0.67	120.442797	20.4411761
DZ-11_22.d	35.17	49	74000	10000	42.3	9.1	169.748229	44.8061242
DZ-11_25.d	11.14	46	Below LOD	Below LOD	16.34	0.78	139.189473	22.8718791
DZ-11_27.d	6.249	25	Below LOD	Below LOD	8.85	0.53	144.158584	31.1096502
DZ-11_28.d	2.663	6	1100	380	2.74	0.19	198.423842	82.8782437

DZ-11_30.d	11.44	29	Below LOD	Below LOD	13.03	0.73	179.248224	36.1199084
DZ-11_31.d	5.556	19	Below LOD	Below LOD	6.74	0.72	168.296697	43.5713003
DZ-11_32.d	7.564	19	Below LOD	Below LOD	7.88	0.55	195.974045	48.1980869
DZ-11_33.d	6.86	51	Below LOD	Below LOD	14.46	0.95	96.8565688	15.8880208
DZ-11_35.d	11.54	12	29400	6800	19.7	1.5	119.594949	36.2975746
DZ-11_37.d	8.393	13	8300	2200	11.7	1	146.455139	43.2506799
DZ-11_38.d	7.703	14	Below LOD	Below LOD	11.43	0.84	137.590016	38.870906
DZ-11_40.d	13.76	19	3420	460	14.91	0.72	188.414378	45.3555895
DZ-11_41.d	8.286	8	2360	390	8.16	0.48	207.313709	75.1620352
Grain	$\rho_s$ ( $\times 10^5/\text{cm}^2$ )	Ns	Cl (ppm)	$1\sigma$ (ppm)	U (ppm)	$1\sigma$ (ppm)	t (Ma)	$1\sigma$ (Ma)
DZ-12_1.d	13.63	21	Below LOD	Below LOD	21.17	0.96	131.453215	30.1653715
DZ-12_3.d	11.89	15	2080	510	9.9	0.79	245.212648	67.6085784
DZ-12_5.d	15.95	28	Below LOD	Below LOD	18.2	1.1	178.930968	36.822886
DZ-12_6.d	16.85	55	Below LOD	Below LOD	18.4	1	186.97274	29.0376378
DZ-12_7.d	26.6	47	Below LOD	Below LOD	27.9	1.8	194.658622	32.8176157
DZ-12_8.d	33.2	77	Below LOD	Below LOD	27.2	1.6	249.209956	34.7387305
DZ-12_9.d	9.746	33	Below LOD	Below LOD	7.78	0.45	255.766121	48.9526161
DZ-12_10.d	7.831	16	Below LOD	Below LOD	13.26	0.7	120.57851	31.505549
DZ-12_12.d	7.776	20	Below LOD	Below LOD	9.48	0.63	167.472739	40.1236956
DZ-12_13.d	4.956	23	1040	520	6.48	0.34	156.153781	34.6419123
DZ-12_14.d	9.196	22	63000	13000	17.7	1.2	106.077166	24.428812
DZ-12_17.d	8.794	13	3500	1200	9.59	0.81	187.225097	55.2364613
DZ-12_19.d	8.134	27	29100	3800	5.19	0.37	319.987501	67.9574677
DZ-12_20.d	5.739	9	Below LOD	Below LOD	8.47	0.7	138.340399	48.1068892
DZ-12_24.d	30.87	17	23200	8800	33	2.8	190.993637	50.172346
DZ-12_26.d	7.842	17	1080	480	9.95	0.68	160.916274	41.489566
DZ-12_29.d	11.12	14	7200	1900	13.43	0.55	169.053818	46.632384
DZ-12_31.d	10.85	6	Below LOD	Below LOD	8.9	0.56	248.906329	103.710528
DZ-12_33.d	4.813	3	30900	9600	6.89	0.57	142.624078	83.549134
DZ-12_39.d	11.32	10	52000	11000	15.5	1.7	149.111432	50.5690056
DZ-12_42.d	7.694	16	Below LOD	Below LOD	6.07	0.43	258.797274	68.7165004
DZ-12_43.d	5.853	10	Below LOD	Below LOD	5.48	0.49	218.069122	72.6465126
DZ-12_44.d	8.949	8	281000	35000	10	1.4	182.713534	70.1924111
Grain	$\rho_s$ ( $\times 10^5/\text{cm}^2$ )	Ns	Cl (ppm)	$1\sigma$ (ppm)	U (ppm)	$1\sigma$ (ppm)	t (Ma)	$1\sigma$ (Ma)
DZ-13_1.d	34.19	43	1510	670	47.2	3	147.887122	25.7338335
DZ-13_2.d	47.53	83	990	480	71.5	6	135.717242	20.1639332
DZ-13_3.d	23.16	61	Below LOD	Below LOD	27.4	1.4	172.56839	25.5890461
DZ-13_4.d	20.55	58	1210	810	20.2	1.1	207.698666	31.6293381
DZ-13_5.d	32.16	65	Below LOD	Below LOD	29.7	1.7	221.071543	32.5244201
DZ-13_6.d	17.19	47	Below LOD	Below LOD	15.24	0.99	230.28421	38.8630428
DZ-13_7.d	30.38	43	Below LOD	Below LOD	32.7	2.2	189.676387	33.2697196
DZ-13_8.d	58.92	121	1120	600	59.8	3.5	201.156841	24.3673163
DZ-13_10.d	37.01	40	1340	530	48.3	3.9	156.439064	29.0588155
DZ-13_11.d	46.25	71	Below LOD	Below LOD	56	4.7	168.615293	26.1828552
DZ-13_12.d	35.87	83	Below LOD	Below LOD	37.7	2.5	194.251007	27.0765799

DZ-13_13.d	39.94	48	Below LOD	Below LOD	49.3	3.1	165.399578	27.5633008
DZ-13_14.d	26.91	59	Below LOD	Below LOD	26.5	1.7	207.31994	32.1502123
DZ-13_15.d	46.71	114	Below LOD	Below LOD	44.3	2.5	215.267959	26.3125149
DZ-13_16.d	85.5	99	41000	19000	68	3.9	256.702709	32.8481565
DZ-13_17.d	72.19	113	Below LOD	Below LOD	87.9	4.1	167.672338	19.8456914
DZ-13_18.d	30.47	53	Below LOD	Below LOD	31.3	2.6	198.74736	33.7003882
DZ-13_19.d	38.82	56	Below LOD	Below LOD	34.4	2	230.393562	35.8565347
DZ-13_20.d	30.72	84	950	400	28.6	1.8	219.294848	30.107916
DZ-13_21.d	27.2	49	1080	340	35.2	1.5	157.760943	25.047725
DZ-13_22.d	20.8	61	Below LOD	Below LOD	20.48	0.92	207.351239	30.3295299
DZ-13_23.d	35.18	56	1830	620	36.6	2.2	196.24021	30.6876885
DZ-13_24.d	49.13	73	Below LOD	Below LOD	38.5	1.9	260.530927	36.0230383
DZ-13_25.d	30.7	54	1020	460	25	1.2	250.709977	38.6828406
DZ-13_26.d	26.09	80	Below LOD	Below LOD	19.4	1.4	274.565269	39.4950929
DZ-13_27.d	42.85	52	Below LOD	Below LOD	38.5	2.1	227.228786	36.0641821
DZ-13_28.d	57.62	85	950	470	57.9	3	203.173912	26.8260433
DZ-13_29.d	19.65	63	1580	550	17.7	1.2	226.653557	34.7107652
DZ-13_30.d	30.64	80	1040	450	31.8	1.4	196.713829	25.9647967
DZ-13_31.d	67.81	74	1300	450	53	3.2	261.210797	37.0724357
DZ-13_32.d	34.18	45	1250	430	32.8	1.7	212.75093	35.5315477
DZ-13_33.d	38.89	81	Below LOD	Below LOD	32.6	1.5	243.553062	32.1699173
DZ-13_34.d	24.82	36	1050	420	25.4	1.4	199.499271	36.6773059
DZ-13_35.d	41.61	61	8600	2200	40.7	2.4	208.726003	31.5546106
DZ-13_37.d	10.47	27	5500	1800	8.83	0.5	242.080178	50.3313227
DZ-13_38.d	18.84	61	Below LOD	Below LOD	17.7	1.1	217.310586	33.1279614
DZ-13_39.d	77.61	83	1270	370	89.3	6.5	177.435076	25.2994081
DZ-13_40.d	37.78	61	Below LOD	Below LOD	42.4	2.2	181.915352	27.025024
DZ-13_42.d	22.68	46	810	360	18.6	1.1	248.944971	41.8201713
DZ-13_43.d	42.11	75	Below LOD	Below LOD	34.1	2.2	252.118151	36.0798008
DZ-13_44.d	15.44	33	1460	460	12.6	0.73	250.17851	47.8904256
DZ-13_45.d	24.06	52	Below LOD	Below LOD	34.8	1.6	141.152844	22.0164607
DZ-13_46.d	34.25	70	17900	7800	31	2.4	225.565219	34.4039381
Grain	$\rho_s$ ( $\times 10^5/\text{cm}^2$ )	Ns	Cl (ppm)	$1\sigma$ (ppm)	U (ppm)	$1\sigma$ (ppm)	t (Ma)	$1\sigma$ (Ma)
DZ-14_1.d	9.448	19	17500	2100	7.81	0.45	246.980179	59.9583904
DZ-14_2.d	12.73	39	13000	1400	11.31	0.62	229.794193	40.8684876
DZ-14_3.d	7.138	29	12900	1400	4.82	0.25	302.344975	60.5874248
DZ-14_4.d	14.58	30	15600	1800	8.62	0.42	345.32141	67.9250107
DZ-14_5.d	17.7	41	15500	2400	13.77	0.88	262.429454	46.5457107
DZ-14_6.d	17.8	39	13100	1800	9.41	0.52	386.192313	68.7363748
DZ-14_7.d	9.452	49	18800	2000	6.04	0.41	319.492025	53.4610824
DZ-14_8.d	14.44	42	12400	1700	7.19	0.43	410.026143	71.4552926
DZ-14_9.d	18.65	54	15000	1800	9.27	0.53	410.745058	64.646648
DZ-14_10.d	12.62	24	16900	1600	7.56	0.43	340.808805	74.578496
DZ-14_11.d	12.2	26	10100	1500	6.67	0.43	373.428313	79.7437775
DZ-14_12.d	10.83	52	11900	1500	6.22	0.48	355.476847	59.6628583

DZ-14_14.d	20.11	51	14600	1500	15.17	0.89	270.644832	43.668437
DZ-14_16.d	8.103	29	6630	860	7.15	0.38	231.373198	46.4427824
DZ-14_17.d	9.639	64	7100	1100	7.28	0.5	270.317307	41.2851541
DZ-14_18.d	11.72	52	13200	1800	5.87	0.38	407.626825	66.2382678
DZ-14_19.d	15.02	35	257000	41000	15.6	1.6	196.57061	40.3207923
DZ-14_20.d	7.526	17	13200	1700	6.83	0.57	224.965935	58.9960852
DZ-14_21.d	20.25	38	11900	1200	14.53	0.93	284.533013	51.9974739
DZ-14_23.d	7.746	28	6190	940	5.95	0.35	265.787026	54.5727249
DZ-14_24.d	9.276	22	7400	1400	9.14	0.55	207.199068	47.2756587
DZ-14_25.d	8.51	31	9000	1200	9.02	0.61	192.617737	38.4345566
DZ-14_26.d	15.08	47	14000	1400	11.46	0.65	268.651936	44.5326637
DZ-14_27.d	9.362	53	5900	1300	8.07	0.5	236.847254	37.9625367
DZ-14_28.d	12.97	28	24000	9100	13.5	1.3	196.146002	42.9605109
DZ-14_29.d	10.63	36	5370	890	9.35	0.65	232.110562	43.7911488
DZ-14_30.d	14.38	36	11900	1500	7.86	0.48	373.516324	69.3685606
DZ-14_31.d	9.203	49	9290	910	7.06	0.35	266.132535	42.788384
DZ-14_32.d	10.6	36	7680	920	6.01	0.36	360.084677	66.7368896
DZ-14_33.d	14.58	21	341000	50000	11.8	1.4	252.260218	64.15515
DZ-14_34.d	7.89	30	9800	1100	6.86	0.41	234.815163	46.8979835
DZ-14_35.d	14.32	43	8400	1000	8.77	0.51	333.362445	57.3746012
DZ-14_36.d	7.186	61	4370	650	6.27	0.4	233.987643	35.8293242
DZ-14_37.d	9.643	34	9570	970	7.94	0.53	247.950459	47.5982736
DZ-14_38.d	7.388	30	11000	930	6.31	0.32	239.040109	47.1394279
DZ-14_39.d	10.42	43	10300	1400	8.72	0.98	243.963292	48.0986128
DZ-14_40.d	24.91	55	6590	740	20.1	1.3	253.01771	40.2836862
DZ-14_41.d	10.83	42	8590	880	9.35	0.6	236.477647	41.5765938
DZ-14_42.d	8.051	19	4880	860	7.09	0.52	231.833847	57.2562038
DZ-14_43.d	10.17	36	8000	1100	6.05	0.41	343.19332	64.5296795
Grain	$\rho_s$ ( $\times 10^5/\text{cm}^2$ )	Ns	Cl (ppm)	$1\sigma$ (ppm)	U (ppm)	$1\sigma$ (ppm)	t (Ma)	$1\sigma$ (Ma)
DZ-15_1.d	11.04	31	850	300	9.32	0.54	242.755626	46.7501185
DZ-15_2.d	4.952	33	550	280	3.2	0.21	317.136916	60.2409985
DZ-15_3.d	4.593	7	Below LOD	Below LOD	7.3	0.54	128.940613	49.9054191
DZ-15_4.d	6.573	23	620	300	6.54	0.36	205.969079	45.1164668
DZ-15_6.d	5.484	19	710	270	7.73	0.43	145.389853	34.7716874
DZ-15_7.d	4.089	16	Below LOD	Below LOD	3.48	0.23	240.798629	62.9496094
DZ-15_8.d	4.194	8	Below LOD	Below LOD	4.81	0.28	178.689689	64.3930264
DZ-15_9.d	4.647	5	Below LOD	Below LOD	8.2	0.57	116.138168	52.7508052
DZ-15_11.d	4.704	7	1190	280	3.67	0.23	262.674183	101.140493
DZ-15_12.d	5.28	18	1310	290	4.03	0.24	268.50045	66.0830264
DZ-15_13.d	4.69	23	990	240	3.75	0.25	256.305377	56.9638598
DZ-15_14.d	5.357	31	620	250	3.46	0.24	317.293874	62.2913341
DZ-15_15.d	5.213	8	710	250	4.75	0.4	224.910774	82.1967345
DZ-15_16.d	3.602	4	Below LOD	Below LOD	4.92	0.3	150.035749	75.7926141
DZ-15_17.d	5.38	9	Below LOD	Below LOD	4.22	0.31	261.267847	89.740763
DZ-15_18.d	6.626	26	450	230	5.87	0.4	231.328678	48.8412361

DZ-15_19.d	3.853	17	510	230	2.69	0.19	293.537014	75.0012884
DZ-15_20.d	6.572	38	450	250	3.72	0.29	362.051836	66.6268059
DZ-15_21.d	5.042	24	Below LOD	Below LOD	3.88	0.25	266.309867	57.9128242
DZ-15_22.d	6.409	18	790	270	7.15	0.5	183.696286	45.7097893
DZ-15_23.d	5.917	24	540	240	3.74	0.24	324.224707	70.4821106
DZ-15_24.d	8.084	19	570	250	4.94	0.32	335.36327	80.9747935
DZ-15_25.d	6.727	22	480	270	4.86	0.27	283.662092	63.4372103
DZ-15_26.d	9.016	35	520	300	5.43	0.33	340.275134	62.5006634
DZ-15_27.d	7.57	39	Below LOD	Below LOD	6.44	0.43	240.894095	42.8030392
DZ-15_28.d	6.661	54	690	290	4.51	0.3	302.67673	47.2947425
DZ-15_31.d	6.819	14	530	290	4.78	0.25	292.35393	80.4033541
DZ-15_32.d	5.03	26	710	250	3.48	0.22	296.213524	62.0851411
DZ-15_33.d	7.001	35	570	240	7.98	0.34	179.793229	32.0914964
DZ-15_34.d	4.655	26	700	240	3.23	0.19	295.347503	61.524568
DZ-15_36.d	4.257	28	470	250	2.46	0.14	354.637521	71.3036971
DZ-15_37.d	4.039	28	670	210	2.99	0.18	276.833605	55.9250102
DZ-15_38.d	4.962	33	690	210	3.9	0.21	260.740381	48.552896
DZ-15_40.d	6.053	22	650	240	3.06	0.19	405.382863	91.3526836
DZ-15_41.d	5.832	19	880	240	3.66	0.2	326.552167	78.0247687
DZ-15_42.d	3.607	12	700	270	4.98	0.36	148.433847	44.5379202
Grain	$\rho_s$ (x10 <sup>5</sup> /cm <sup>2</sup> )	Ns	Cl (ppm)	1 $\sigma$ (ppm)	U (ppm)	1 $\sigma$ (ppm)	t (Ma)	1 $\sigma$ (Ma)
DZ-16_2.d	8.89	18	Below LOD	Below LOD	10.07	0.78	180.920774	45.4207015
DZ-16_3.d	8.5	12	7700	1600	13.3	1	130.973499	39.3920961
DZ-16_5.d	6.209	36	Below LOD	Below LOD	6.55	0.62	194.265869	37.9738685
DZ-16_6.d	6.795	23	580	460	6.94	0.65	200.65322	46.5077568
DZ-16_7.d	7.39	20	Below LOD	Below LOD	8.82	0.7	171.708581	41.2712408
DZ-16_8.d	10.79	23	Below LOD	Below LOD	12.18	0.67	181.547513	39.7653307
DZ-16_9.d	11.09	26	Below LOD	Below LOD	20.3	1.6	111.957105	24.0502293
DZ-16_10.d	14.44	25	3060	680	27	2.9	109.602277	25.2344076
DZ-16_11.d	10.88	27	Below LOD	Below LOD	14.2	1	157.020623	32.7374668
DZ-16_12.d	16.42	17	Below LOD	Below LOD	30.2	2.5	111.424926	28.8736016
DZ-16_13.d	12.38	38	Below LOD	Below LOD	13.03	0.92	194.711845	35.2495008
DZ-16_14.d	22.72	53	Below LOD	Below LOD	40.1	2.8	116.1128	18.4381334
DZ-16_15.d	5.948	14	Below LOD	Below LOD	7.4	0.71	164.723433	47.2002444
DZ-16_16.d	5.735	45	Below LOD	Below LOD	9.05	0.85	129.867652	23.4179956
DZ-16_18.d	5.747	28	Below LOD	Below LOD	6.98	0.61	168.733735	35.7237981
DZ-16_20.d	5.264	16	Below LOD	Below LOD	7.17	0.5	150.457163	39.47467
DZ-16_21.d	5.747	17	Below LOD	Below LOD	6.3	0.4	186.946265	47.4147882
DZ-16_24.d	14.12	33	450	230	28.3	2.7	102.250257	20.6732074
DZ-16_26.d	7.897	8	Below LOD	Below LOD	13.8	1.3	117.273314	43.1442331
DZ-16_27.d	9.228	13	400	240	9.31	0.56	203.129991	58.1723596
DZ-16_28.d	4.027	11	Below LOD	Below LOD	5.3	0.37	155.711936	48.5599227
DZ-16_29.d	12.81	66	Below LOD	Below LOD	13.27	0.77	197.831003	27.9711122
DZ-16_30.d	7.79	21	Below LOD	Below LOD	7.73	0.53	206.525703	47.8999021
DZ-16_31.d	7.111	17	Below LOD	Below LOD	7.45	0.38	195.609774	49.0577276

DZ-16_32.d	16.82	54	Below LOD	Below LOD	29.2	2	118.048178	18.5460298
DZ-16_34.d	5.198	20	13700	2200	8.79	0.52	121.189096	28.414133
DZ-16_36.d	10.69	33	380	250	20.1	1.1	108.992796	20.3236774
DZ-16_38.d	46.25	84	Below LOD	Below LOD	76.2	3.8	124.386403	15.6667601
DZ-16_39.d	9.355	38	550	230	17.9	1.1	107.1043	19.0285913
DZ-16_40.d	9.056	37	Below LOD	Below LOD	19.2	1.1	96.6610106	17.2321673
DZ-16_41.d	25.19	59	Below LOD	Below LOD	43	2.4	120.053786	17.618354
DZ-16_43.d	7.207	18	Below LOD	Below LOD	11.63	0.95	126.996267	32.0525048
DZ-16_44.d	9.752	31	Below LOD	Below LOD	17.3	1.7	115.521745	24.0625416
DZ-16_45.d	6.439	25	Below LOD	Below LOD	9.06	0.83	145.64862	32.5240257
DZ-16_46.d	4.788	21	Below LOD	Below LOD	5.13	0.26	191.272671	43.4740853
Grain	$\rho_s$ ( $\times 10^5/\text{cm}^2$ )	Ns	Cl (ppm)	$1\sigma$ (ppm)	U (ppm)	$1\sigma$ (ppm)	t (Ma)	$1\sigma$ (Ma)
DZ-17_3.d	10.65	30	640	240	8.26	0.57	264.232177	52.5600741
DZ-17_4.d	9.426	21	460	220	8.92	0.64	216.560241	50.4354288
DZ-17_6.d	10.05	29	720	210	13.84	0.89	148.814798	29.7965748
DZ-17_7.d	5.944	9	Below LOD	Below LOD	8.2	1	148.552886	53.0347431
DZ-17_8.d	12.78	29	470	150	11.95	0.83	219.168983	44.258702
DZ-17_9.d	19.42	36	36600	7000	16.1	0.86	247.194892	44.2909525
DZ-17_10.d	8.188	15	3600	1600	7.86	0.58	213.486999	57.9113417
DZ-17_14.d	5.126	11	29600	8500	3.95	0.37	265.948563	84.5848829
DZ-17_18.d	9.72	18	770	230	12.43	0.7	160.254888	39.3194161
DZ-17_19.d	11.7	22	1420	650	9.22	0.58	260.058519	58.662735
DZ-17_22.d	3.015	4	380	170	3.18	0.22	194.301584	98.3593198
DZ-17_25.d	8.768	16	570	230	10.02	0.58	179.328355	46.5297209
DZ-17_26.d	6.909	8	690	240	9.45	0.73	149.830258	54.5266251
DZ-17_29.d	6.755	15	640	280	9.01	0.58	153.64439	41.3080246
DZ-17_30.d	10.35	27	1970	870	7.73	0.5	274.395508	56.6965623
DZ-17_36.d	10.25	11	Below LOD	Below LOD	10.8	0.96	194.498499	61.5926922
DZ-17_38.d	3.498	7	Below LOD	Below LOD	6.36	0.56	112.714253	43.9560068
DZ-17_41.d	7.105	5	268000	76000	16.2	4.3	89.8804448	46.8695744
Grain	$\rho_s$ ( $\times 10^5/\text{cm}^2$ )	Ns	Cl (ppm)	$1\sigma$ (ppm)	U (ppm)	$1\sigma$ (ppm)	t (Ma)	$1\sigma$ (Ma)
DZ-18_5.d	8.92	12	680	370	7.86	0.5	232.579346	69.3274968
DZ-18_6.d	31.07	38	900	360	25.4	1.3	250.689632	43.7147185
DZ-18_7.d	5.457	15	13500	3000	4.63	0.31	241.547085	65.0932107
DZ-18_8.d	7.456	14	Below LOD	Below LOD	6.48	0.89	235.808649	71.4327984
DZ-18_10.d	2.632	4	870	370	4.13	0.35	130.606465	66.4239087
DZ-18_11.d	3.03	9	3190	650	2.45	0.18	253.457637	87.0586219
DZ-18_13.d	2.471	8	Below LOD	Below LOD	3.17	0.29	159.750535	58.6616091
DZ-18_14.d	4.227	12	Below LOD	Below LOD	5.34	0.46	162.225765	49.2659568
DZ-18_15.d	7.925	25	Below LOD	Below LOD	6.62	0.47	245.340993	52.9123286
DZ-18_17.d	8.529	15	630	310	13.5	1.2	129.477167	35.7038401
DZ-18_20.d	4.775	6	Below LOD	Below LOD	3.82	0.28	256.176242	106.709526
DZ-18_22.d	9.115	19	Below LOD	Below LOD	12.58	0.73	148.49262	35.5983729
DZ-18_23.d	15.18	26	Below LOD	Below LOD	30	2.5	103.700144	22.4525354
DZ-18_25.d	2.096	6	Below LOD	Below LOD	2.95	0.21	145.612314	60.6010593

DZ-18_26.d	4.847	25	Below LOD	Below LOD	4.51	0.26	220.254766	46.6169737
DZ-18_27.d	5.233	6	Below LOD	Below LOD	4.08	0.26	262.856916	109.077685
DZ-18_29.d	44.9	42	79000	12000	36.9	2.5	249.372645	43.1003787
DZ-18_31.d	13.03	20	3500	1100	25.1	1.9	106.389687	25.4452478
DZ-18_36.d	5.873	10	Below LOD	Below LOD	6.34	0.64	189.845183	63.4385537
DZ-18_40.d	2.824	6	710	360	3.01	0.4	192.276866	82.8797729
DZ-18_41.d	3.585	9	Below LOD	Below LOD	4.55	0.27	161.475487	55.0213982
DZ-18_43.d	2.397	5	150000	21000	2.03	0.52	241.991902	125.063015
DZ-18_44.d	2.376	4	102000	31000	3.8	1	128.142054	72.5700952
Grain	$\rho_s$ ( $\times 10^5/\text{cm}^2$ )	Ns	Cl (ppm)	$1\sigma$ (ppm)	U (ppm)	$1\sigma$ (ppm)	t (Ma)	$1\sigma$ (Ma)
DZ-19_1.d	4.079	10	Below LOD	Below LOD	5.16	0.35	162.001915	52.7622044
DZ-19_2.d	0.9372	3	Below LOD	Below LOD	1.5	0.15	128.043391	75.187279
DZ-19_3.d	2.406	5	710	330	2.69	0.22	183.298744	83.6294419
DZ-19_5.d	18.81	27	Below LOD	Below LOD	22.4	1.6	172.090511	35.9382581
DZ-19_6.d	29.08	28	9700	1700	24.7	1.4	241.275704	48.4953757
DZ-19_7.d	0.8992	2	940	380	1.51	0.12	122.038117	86.9634281
DZ-19_8.d	10.77	35	Below LOD	Below LOD	16.05	0.81	137.517134	24.8258289
DZ-19_10.d	2.897	7	Below LOD	Below LOD	4.14	0.27	143.405003	55.2775208
DZ-19_11.d	3.678	3	23700	6600	8.6	1.8	87.6454587	53.9296072
DZ-19_12.d	6.34	8	670	440	12.71	0.85	102.225644	36.9916741
DZ-19_16.d	1.384	2	1020	510	2.55	0.22	111.22747	79.3478116
DZ-19_18.d	2.579	5	Below LOD	Below LOD	4.89	0.43	108.083308	49.4361316
DZ-19_19.d	6.827	16	710	300	8.23	0.4	169.99894	43.7840709
DZ-19_20.d	39.38	67	Below LOD	Below LOD	59.3	3	136.093432	18.7379864
DZ-19_22.d	1.345	6	Below LOD	Below LOD	2.47	0.21	111.594162	46.7321721
DZ-19_23.d	1.724	4	Below LOD	Below LOD	2.61	0.23	135.36703	68.9226828
DZ-19_24.d	1.701	3	Below LOD	Below LOD	3.37	0.24	103.440489	60.3047828
DZ-19_26.d	7.973	8	Below LOD	Below LOD	5.25	0.34	311.227957	112.502102
DZ-19_30.d	1.782	4	670	320	1.82	0.14	200.656142	101.800022
DZ-19_31.d	3.831	5	1590	420	3.46	0.26	226.909248	103.267153
DZ-19_32.d	2.833	6	Below LOD	Below LOD	2.58	0.17	225.031342	93.4573052
DZ-19_34.d	10.16	5	Below LOD	Below LOD	12.41	0.74	167.779182	75.9704424
DZ-19_36.d	1.799	2	Below LOD	Below LOD	2.19	0.17	168.346153	119.927945
DZ-19_37.d	4.507	3	Below LOD	Below LOD	9.14	0.55	101.054932	58.7881547
DZ-19_40.d	1.87	4	Below LOD	Below LOD	2.3	0.18	166.621068	84.5668983
Grain	$\rho_s$ ( $\times 10^5/\text{cm}^2$ )	Ns	Cl (ppm)	$1\sigma$ (ppm)	U (ppm)	$1\sigma$ (ppm)	t (Ma)	$1\sigma$ (Ma)
DZ-20_1.d	2.914	10	2550	420	3.61	0.26	165.42399	54.0254417
DZ-20_2.d	6.636	24	2570	410	3.65	0.23	372.588676	80.8695393
DZ-20_3.d	5.42	12	2390	380	10.59	0.78	104.886472	31.5062344
DZ-20_4.d	2.223	4	2300	410	3.39	0.26	134.386582	68.1744921
DZ-20_5.d	13.33	24	2100	480	19.9	1.6	137.275558	30.5737938
DZ-20_6.d	7.242	19	2630	410	8.75	0.52	169.61592	40.7204246
DZ-20_7.d	4.822	8	3310	490	5.42	0.39	182.324094	66.1537454
DZ-20_9.d	9.793	31	2590	380	14.71	0.85	136.432937	26.2679906
DZ-20_10.d	6.183	24	2670	420	6.75	0.41	187.720464	40.6224844

DZ-20_11.d	7.369	13	2450	390	6.28	0.38	240.472299	68.8846415
DZ-20_13.d	4.665	9	1700	390	4.97	0.37	192.35851	66.1125198
DZ-20_15.d	5.722	13	2830	330	8.57	0.45	136.830583	38.9793288
DZ-20_17.d	2.175	5	5590	500	3.29	0.21	135.481348	61.4235109
DZ-20_20.d	4.445	14	2380	290	4.31	0.23	211.354082	58.1698717
DZ-20_21.d	2.54	8	2180	270	2.98	0.17	174.676145	62.9141422
DZ-20_22.d	3.578	7	32200	8400	5.42	0.39	135.287353	52.3104093
DZ-20_24.d	3.779	13	2170	330	3.96	0.24	195.568025	56.0255496
DZ-20_26.d	4.023	9	2480	360	4.3	0.29	191.733377	65.6198499
DZ-20_30.d	2.93	13	2480	320	3.61	0.21	166.33229	47.5661982
DZ-20_31.d	13.48	20	12000	3500	21.1	1.9	130.925302	31.9578101
DZ-20_32.d	2.676	7	1970	370	3.22	0.23	170.312445	65.8366153
DZ-20_33.d	4.523	14	1930	350	3.91	0.28	237.0642	66.2207697
DZ-20_34.d	2.233	4	11100	1500	1.86	0.14	246.032184	124.759845
DZ-20_36.d	4.924	20	3470	500	3.63	0.23	277.988968	65.4821531
DZ-20_37.d	2.202	3	2310	420	3.66	0.3	123.296963	72.0548439
DZ-20_39.d	4.742	15	1760	270	7.52	0.52	129.228963	34.8967449
DZ-20_40.d	4.429	11	2100	360	4.38	0.3	207.227656	64.5648821
DZ-20_43.d	6.217	27	3120	400	5.21	0.33	244.545282	50.4269317
DZ-20_44.d	3.143	16	2320	300	3.25	0.21	198.187913	51.7371008
DZ-20_47.d	5.158	23	3190	360	5.49	0.28	192.541849	41.9863917
DZ-20_48.d	2.954	7	2090	360	3.31	0.23	182.893656	70.6352828
Grain	$\rho_s$ ( $\times 10^5/\text{cm}^2$ )	Ns	Cl (ppm)	$1\sigma$ (ppm)	U (ppm)	$1\sigma$ (ppm)	t (Ma)	$1\sigma$ (Ma)
DZ-21_2.d	6.502	26	6110	640	5.54	0.33	240.51416	50.1528717
DZ-21_3.d	9.761	16	7520	720	3.9	0.25	512.900527	133.828199
DZ-21_4.d	31.02	43	5850	600	47.4	2.6	134.111774	22.335522
DZ-21_5.d	11.84	21	19200	2400	11.96	0.59	202.87287	46.0503295
DZ-21_6.d	7.25	42	4260	560	5.18	0.27	286.821495	47.9933257
DZ-21_8.d	4.33	11	7720	880	5.7	0.33	155.674146	48.1668061
DZ-21_10.d	10.65	18	5160	570	9.19	0.61	237.485745	58.8628118
DZ-21_12.d	6.741	9	22700	5000	8.7	0.54	158.784654	54.1816441
DZ-21_14.d	15.45	26	9710	870	13.81	0.89	229.265261	48.1387018
DZ-21_15.d	12.88	36	6650	750	10.44	0.68	252.824299	46.2693116
DZ-21_16.d	11.88	18	4330	590	10.07	0.62	241.763325	59.6223059
DZ-21_17.d	26.65	31	10360	920	21	1.2	260.064677	50.0215393
DZ-21_19.d	5.466	12	5990	660	2.19	0.14	511.480348	152.496926
DZ-21_20.d	18.46	36	10600	1000	12.54	0.81	301.67381	55.1513949
DZ-21_23.d	4.644	7	4320	520	4.04	0.26	235.566916	90.7685618
DZ-21_24.d	4.762	7	6500	1100	4.3	0.32	226.946968	87.8573859
DZ-21_25.d	7.253	17	4500	640	5.43	0.37	273.729306	69.7547584
DZ-21_26.d	8.202	33	5610	830	5.21	0.4	322.615692	62.6155726
DZ-21_30.d	7.397	20	77000	15000	5.39	0.46	281.235604	68.170377
DZ-21_31.d	4.945	16	13100	1100	4.4	0.32	230.312267	60.6126561
DZ-21_32.d	5.801	13	4690	620	4.47	0.35	265.949263	77.3204987
DZ-21_33.d	6.949	14	382000	78000	6.5	1.4	219.084879	75.6688355

DZ-21_34.d	4.512	8	13600	2300	3.79	0.2	243.96826	87.7122933
DZ-21_35.d	3.231	9	96000	10000	1.9	0.27	348.487177	126.983944
DZ-21_36.d	5.652	14	3640	410	4.39	0.24	263.840269	72.6829362
DZ-21_37.d	8.411	13	5450	560	4.72	0.28	365.181761	104.517623
DZ-21_39.d	9.099	14	9500	1100	6.42	0.39	290.443782	80.3806459
DZ-21_41.d	3.921	7	20700	6000	3.15	0.29	255.087829	99.7146019
DZ-21_42.d	5.093	14	19800	3100	3.61	0.24	289.114532	80.3929559
DZ-21_43.d	21.88	29	10800	1100	12.21	0.87	367.227417	74.3869858
DZ-21_44.d	3.438	8	24300	5800	2.74	0.24	257.133558	94.177097
Grain	$\rho_s$ ( $\times 10^5/\text{cm}^2$ )	Ns	Cl (ppm)	$1\sigma$ (ppm)	U (ppm)	$1\sigma$ (ppm)	t (Ma)	$1\sigma$ (Ma)
DZ-22b_6.d	10.45	21	2200	310	26.2	1.6	82.3799364	19.0596238
DZ-22b_7.d	6.108	7	1690	340	17.22	0.97	73.2609134	28.2040571
DZ-22b_11.d	10.25	16	1410	360	9.71	0.69	218.027402	57.5731815
DZ-22b_17.d	5.404	7	23800	4200	9.31	0.66	119.887005	46.4417712
DZ-22b_21.d	5.66	15	1560	350	5.27	0.45	221.825905	61.2087155
DZ-22b_27.d	11.35	17	1290	350	18.5	1.6	126.715745	33.1607117
DZ-22b_29.d	6.829	21	940	270	9.72	0.68	145.109985	33.9363322
DZ-22b_30.d	15.74	42	1000	260	18.1	1.3	179.610863	31.6992795
DZ-22b_31.d	13.18	29	1700	430	12.74	0.92	213.674368	43.72641
DZ-22b_36.d	5.841	12	940	330	11.13	0.78	108.392314	32.5943474
DZ-22b_38.d	5.886	11	1080	330	9.71	0.68	125.200908	39.1927971
DZ-22b_41.d	8.305	18	2140	470	11.7	1.1	146.608862	37.8281883
DZ-22b_45.d	7.488	11	1450	340	16.2	1.2	95.4678786	29.9739049
DZ-22b_48.d	2.052	4	2840	550	4.46	0.35	95.0274222	48.2996004
DZ-22b_49.d	5.582	18	1470	380	6.09	0.37	189.312367	46.9200363
DZ-22b_55.d	16.39	24	1500	260	17.04	0.86	198.66246	42.7904292
DZ-22b_60.d	6.296	12	53000	12000	6.09	0.47	213.527529	64.5791304
DZ-22b_61.d	9.528	11	9400	1500	11.92	0.58	165.094248	51.0076607
DZ-22b_62.d	5.023	12	1070	330	7.94	0.49	130.661947	39.0506477
DZ-22b_67.d	4.203	8	1210	380	4.02	0.45	215.943324	80.7150906
DZ-22b_69.d	4.168	6	990	370	10.11	0.82	85.1496774	35.6639229
DZ-22b_70.d	6.815	18	620	330	8.86	0.82	158.86879	40.9072026
DZ-22b_71.d	4.971	13	1590	430	6.53	0.45	157.230585	45.5296412
DZ-22b_73.d	8.338	18	1030	350	17.2	1.2	100.124393	25.0517553
DZ-22b_75.d	3.642	10	1230	320	7.07	0.46	106.396411	34.7076486
DZ-22b_76.d	5.038	6	19700	5200	13.1	1.4	79.431602	33.7250588
DZ-22b_89.d	9.241	27	1050	310	10.06	0.72	189.726256	39.9505712
DZ-22b_94.d	2.894	16	1840	370	3.15	0.26	189.755521	50.7371445
DZ-22b_95.d	4.191	8	1010	300	3.88	0.31	223.096307	81.5335862
Grain	$\rho_s$ ( $\times 10^5/\text{cm}^2$ )	Ns	Cl (ppm)	$1\sigma$ (ppm)	U (ppm)	$1\sigma$ (ppm)	t (Ma)	$1\sigma$ (Ma)
DZ-23b_1.d	8.799	13	13500	1100	5.06	0.49	359.122313	106.823537
DZ-23b_7.d	15.03	28	10900	1200	10.1	0.71	307.324509	63.6066047
DZ-23b_11.d	14.66	37	9700	1200	14.3	1.1	211.717875	39.6790814
DZ-23b_13.d	31.8	52	27600	5900	18	1.4	364.849877	60.4598243
DZ-23b_15.d	8.42	12	6200	1000	12.4	1.1	140.232929	42.8532404

DZ-23b_18.d	19.56	39	9300	1000	16.6	1.5	243.343839	46.1625054
DZ-23b_21.d	10.16	14	10900	1100	12.9	1.3	162.653568	47.0753157
DZ-23b_23.d	12.82	23	6440	550	9.4	0.79	281.656491	64.671645
DZ-23b_27.d	5.949	11	6740	670	5.64	0.36	217.833395	67.9009737
DZ-23b_29.d	7.538	23	8930	740	7.29	0.5	213.544406	47.9228117
DZ-23b_37.d	8.947	17	1400	350	9.21	0.59	200.621466	51.1909048
DZ-23b_42.d	15.42	24	18400	1500	13.8	1	230.762312	51.1323759
DZ-23b_45.d	10.37	27	11500	1200	8.21	0.53	260.852613	54.3329081
DZ-23b_46.d	4.316	9	1790	270	3.35	0.26	266.070191	91.9059271
DZ-23b_48.d	12.33	20	2470	280	15.02	0.92	169.532411	40.0942967
DZ-23b_49.d	10.44	33	7570	590	9.58	0.77	225.058067	44.4131721
DZ-23b_50.d	8.357	11	9800	1400	5.01	0.39	344.486547	108.471686
DZ-23b_51.d	9.996	22	8190	760	6.56	0.45	314.689316	71.9946459
DZ-23b_53.d	12.94	25	16000	1500	12.24	0.91	218.329516	47.6876551
DZ-23b_72.d	6.422	13	13000	1100	6.47	0.44	204.986668	59.3145387
DZ-23b_77.d	12.5	18	25300	2900	7.1	0.48	363.589433	90.7563434
DZ-23b_78.d	18.12	31	17200	1600	10.45	0.78	358.097668	71.6280543
DZ-23b_80.d	18.03	27	10600	1700	10.8	1.9	344.771661	91.3268316
DZ-23b_82.d	17.94	21	7200	1400	11.4	1.3	324.995373	81.445683
DZ-23b_88.d	20.77	31	11300	1100	27.1	2	158.280277	31.6104245
DZ-23b_91.d	10.44	19	11200	1100	7.55	0.52	285.570366	69.6905111
DZ-23b_92.d	8.198	12	5570	520	5.45	0.43	310.649746	94.0907525
DZ-23b_99.d	15.15	30	13100	1400	8.42	0.65	371.586674	75.6732279
DZ-23b_103.d	10.62	20	11300	1300	7.05	0.52	311.096403	74.6764369
DZ-23b_104.d	8.509	18	12100	1400	5.85	0.39	300.387772	74.9045401
DZ-23b_108.d	15.18	34	13500	1200	9.7	0.6	323.191274	60.8235687
Grain	$\rho_s$ ( $\times 10^5/\text{cm}^2$ )	Ns	Cl (ppm)	$1\sigma$ (ppm)	U (ppm)	$1\sigma$ (ppm)	t (Ma)	$1\sigma$ (Ma)
DZ-24b_1.d	14.61	25	1840	310	13.63	0.92	221.403372	47.8641723
DZ-24b_2.d	11.89	30	1740	280	11.53	0.79	213.001381	42.7109023
DZ-24b_3.d	23.67	56	1280	250	19.5	1.5	250.722619	40.3923548
DZ-24b_4.d	38.41	64	1620	350	27.1	2.3	292.755379	46.2962597
DZ-24b_5.d	15.16	38	950	250	12.56	0.75	249.309847	44.6408013
DZ-24b_6.d	7.393	29	1310	290	5.72	0.47	266.965134	55.6252001
DZ-24b_7.d	11.79	37	1750	350	12.16	0.76	200.267327	36.4428176
DZ-24b_9.d	13.43	42	2070	340	18.7	1.2	148.342051	25.7396214
DZ-24b_10.d	14.78	57	2240	310	12.98	0.77	235.195826	35.8572061
DZ-24b_11.d	56.29	100	1210	210	78.8	4.8	147.548536	18.5996597
DZ-24b_12.d	22.14	65	2150	340	17.9	1.3	255.478557	38.6095843
DZ-24b_14.d	13.7	55	1440	280	9.84	0.59	287.577786	44.5114847
DZ-24b_15.d	2.77	9	900	270	1.84	0.15	310.950897	107.688281
DZ-24b_16.d	6.51	16	13600	1900	8.71	0.4	154.380593	39.8974984
DZ-24b_17.d	11.54	17	4290	900	9.62	0.62	247.776781	63.2473362
DZ-24b_18.d	10.21	39	1360	340	9.19	0.61	229.477495	41.1955129
DZ-24b_20.d	12.86	46	1740	310	10.36	0.69	256.395903	43.1744478
DZ-24b_21.d	10.26	29	1580	290	12.9	1	164.28107	33.9359241

DZ-24b_22.d	20.91	45	2230	400	29.5	2.2	146.407016	25.343202
DZ-24b_24.d	15.26	27	1430	320	19.9	1.1	158.391302	32.5657416
DZ-24b_28.d	7.151	21	1010	330	5.84	0.44	252.920364	59.5710155
DZ-24b_31.d	7.697	19	1410	360	6.93	0.65	229.413051	57.8599612
DZ-24b_32.d	7.556	21	1980	280	5.95	0.56	262.303962	63.5281004
DZ-24b_33.d	8.282	24	2170	410	7.21	0.58	237.262899	53.2220361
DZ-24b_35.d	14.33	39	1550	260	16.8	1	176.184127	31.2021175
DZ-24b_38.d	6.813	36	1530	280	9.6	0.78	146.58753	28.0283088
DZ-24b_42.d	6.511	15	1200	290	5.94	0.38	226.407663	61.1465592
DZ-24b_43.d	12.45	15	1870	360	17.2	1.4	149.510185	41.073685
DZ-24b_45.d	9.931	23	5300	1200	8.96	0.64	228.936396	51.5795367
DZ-24b_46.d	7.716	27	1820	380	6.24	0.49	255.409766	54.4109309
DZ-24b_47.d	5.128	13	1570	310	3.75	0.32	282.453276	83.0167472
DZ-24b_48.d	15.86	30	1380	320	18.9	1.3	173.329007	34.7716134
DZ-24b_49.d	10.11	20	1770	260	8.84	0.69	236.226578	57.0244257
DZ-24b_52.d	4.255	11	1840	340	3	0.24	292.959899	92.4051473
DZ-24b_54.d	4.706	13	1550	400	3.91	0.34	248.602238	73.1856575
DZ-24b_55.d	3.891	13	1030	280	3.44	0.31	233.632179	69.0003033
DZ-24b_56.d	3.746	18	1320	360	3.03	0.24	255.36126	64.6066849
DZ-24b_57.d	5.218	21	1950	390	4.14	0.36	260.335625	62.3505727
DZ-24b_58.d	27.42	50	2440	310	22.9	1.4	247.32148	39.8161851
DZ-24b_60.d	7.787	17	1030	300	9.55	0.67	168.421168	43.2438067
DZ-24b_61.d	8.722	19	1480	290	7.05	0.58	255.53879	63.4127458
DZ-24b_62.d	13.22	32	1170	330	17.02	0.91	160.43598	30.562437
Grain	$\rho_s$ ( $\times 10^5/\text{cm}^2$ )	Ns	Cl (ppm)	$1\sigma$ (ppm)	U (ppm)	$1\sigma$ (ppm)	t (Ma)	$1\sigma$ (Ma)
DZ-25_2.d	11.63	20	12700	4500	23	2	103.313643	27.0982367
DZ-25_4.d	15.96	29	2670	520	32.5	2.3	100.335663	22.5980694
DZ-25_7.d	10.99	30	29200	4700	16.12	0.88	139.295939	30.3743684
DZ-25_10.d	5.21	19	3360	500	7.64	0.49	139.331772	36.3279757
DZ-25_11.d	8.411	21	4170	550	8.06	0.71	213.215309	55.0301648
DZ-25_13.d	9.441	18	4290	650	15.8	1.2	122.086238	32.8860949
DZ-25_15.d	9.272	23	3910	530	11.04	0.88	171.597179	42.4046767
DZ-25_16.d	10.43	14	5300	580	14.4	1.1	147.98838	44.0247286
DZ-25_18.d	8.275	13	4550	630	8.25	0.56	204.936752	62.4185433
DZ-25_20.d	6.635	12	283000	30000	7.7	1.4	176.058095	62.8964449
DZ-25_22.d	70.94	79	5120	660	134.9	9.7	107.444709	18.3172574
DZ-25_23.d	15.23	30	4360	560	13.16	0.57	236.455711	50.9585248
DZ-25_24.d	16.2	27	6880	870	23.2	1.4	142.670055	32.5067566
DZ-25_26.d	28.93	34	3930	570	50.4	3.4	117.27993	24.933443
DZ-25_27.d	25.18	38	6780	600	28.3	1.6	181.792133	36.696513
DZ-25_30.d	10.2	26	5350	690	10.88	0.79	191.547757	44.9092347
DZ-25_31.d	11.9	25	3480	730	10.39	0.65	234.011504	54.9547979
DZ-25_32.d	61.57	85	3630	620	112.7	6.8	111.622318	18.2188697
DZ-25_37.d	10.64	26	5220	610	11.68	0.73	186.124945	43.0922099
DZ-25_38.d	22.64	31	564000	96000	28.5	6	162.307041	48.0972798

DZ-25_40.d	3.994	13	6200	920	5.38	0.41	151.681139	46.4961171
DZ-25_43.d	46.76	79	7500	1000	73.6	6.9	129.808307	23.4671061
DZ-25_44.d	20.27	27	590000	120000	19.5	3.3	212.385533	58.9006054
DZ-25_45.d	27.22	35	9500	1700	55.1	3.5	100.935124	21.1341499
DZ-25_46.d	15.74	30	46500	9300	15.7	2	204.838162	50.5067501
DZ-25_48.d	11.16	19	177000	29000	13.5	1.1	168.902556	44.8486167
DZ-25_50.d	7.505	14	175000	29000	8.14	0.75	188.378827	56.8745064

## 11. APPENDIX C: AU–Pb DATA TABLE

**Table 6 – Single-grain AU–Pb data used in this study for all samples, as calculated with Iolite software (Paton et al., 2011). Final 238/206 and 207/206 represent the ratios of  $^{238}\text{U}/^{206}\text{Pb}$  and  $^{207}\text{Pb}/^{206}\text{Pb}$  with  $2\sigma$  as the reported standard error. Error correlation represents that correlation of standard error between  $^{238}\text{U}/^{206}\text{Pb}$  and  $^{207}\text{Pb}/^{206}\text{Pb}$ . Common-Pb corrected AU–Pb ages given by the Final 207 Age with  $2\sigma$  as the reported standard error.**

Grain	Final 238/206	$2\sigma$	Final 207/206	$2\sigma$	Error Correlation 238/206 vs 207/206	Final 207 Age (Ma)	$2\sigma$ (Ma)
DZ-01_7.d	13.42282	1.1	0.32	0.04	0.34112	353	36
DZ-01_14.d	5.235602	0.39	0.834	0.061	-0.13324	308	75
DZ-01_15.d	12.12121	1	0.449	0.044	0.1738	314	35
DZ-01_17.d	4.237288	0.38	0.856	0.048	0.237	334	76
DZ-01_19.d	6.849315	0.76	0.765	0.058	0.14513	273	56
DZ-01_20.d	4.329004	0.53	0.864	0.058	0.16299	314	79
DZ-01_21.d	5.917116	0.37	0.82	0.049	0.17678	282	55
DZ-01_22.d	3.690037	0.37	0.903	0.052	0.098385	330	100
DZ-01_23.d	4.807692	0.35	0.858	0.061	0.47519	327	84
DZ-01_24.d	12.34568	1.4	0.457	0.056	-0.25728	300	37
DZ-01_26.d	8.006405	0.48	0.718	0.048	0.4255	292	43
DZ-01_30.d	6.578947	0.73	0.783	0.078	0.31819	283	78
DZ-01_31.d	3.571429	0.47	0.89	0.054	-0.03762	340	110
DZ-01_34.d	8.474576	0.94	0.704	0.076	0.27679	272	74
DZ-01_35.d	6.622517	0.96	0.746	0.064	0.16784	314	75
DZ-01_36.d	2.754821	0.43	0.965	0.057	-0.066017	250	120
DZ-01_37.d	3.278689	0.39	0.941	0.068	0.34518	330	140
DZ-01_39.d	14.49275	0.94	0.251	0.021	-0.17886	332	17
DZ-01_40.d	5.434783	0.4	0.869	0.063	0.16932	267	79
DZ-01_44.d	7.54717	0.51	0.689	0.036	0.18993	327	38
DZ-01_45.d	5.050505	0.34	0.777	0.033	0.26475	366	52
DZ-01_48.d	7.462687	0.6	0.748	0.054	0.063232	283	55
DZ-01_51.d	6.501951	0.36	0.708	0.042	0.2951	364	49
Grain	Final 238/206	$2\sigma$	Final 207/206	$2\sigma$	Error Correlation 238/206 vs 207/206	Final 207 Age	$2\sigma$
DZ-03_1.d	9.389671	0.48	0.426	0.02	0.29649	367	28
DZ-03_2.d	8.857396	0.48	0.468	0.022	0.45733	352	32

DZ-03_3.d	5.711022	0.31	0.591	0.028	0.15478	383	45
DZ-03_4.d	6.002401	0.33	0.556	0.02	0.31578	397	40
DZ-03_5.d	7.633588	0.36	0.472	0.02	0.28814	394	32
DZ-03_6.d	7.942812	0.39	0.479	0.02	0.079857	380	29
DZ-03_7.d	4.385965	0.26	0.677	0.032	0.021986	330	59
DZ-03_9.d	11.53403	0.56	0.302	0.012	0.25943	374	20
DZ-03_11.d	3.508772	0.21	0.71	0.038	0.15476	338	84
DZ-03_12.d	7.423905	0.42	0.52	0.026	0.070438	362	37
DZ-03_13.d	5.154639	0.43	0.634	0.032	0.44932	349	68
DZ-03_14.d	5.656109	0.33	0.619	0.027	0.17339	346	45
DZ-03_15.d	6.930007	0.33	0.551	0.024	0.060323	360	37
DZ-03_16.d	7.032349	0.48	0.543	0.027	0.095519	360	40
DZ-03_17.d	9.803922	0.62	0.358	0.017	0.18638	410	36
DZ-03_18.d	10.38422	0.59	0.376	0.016	0.2634	364	24
DZ-03_19.d	4.878049	0.38	0.641	0.037	0.22288	374	65
DZ-03_20.d	9.345794	0.54	0.434	0.025	0.011015	360	31
DZ-03_21.d	7.581501	0.53	0.486	0.029	0.014043	383	38
DZ-03_22.d	6.622517	0.53	0.51	0.025	0.23675	416	45
DZ-03_23.d	5.208333	0.41	0.615	0.029	-0.28062	347	41
DZ-03_24.d	7.496252	0.44	0.521	0.021	0.25099	361	32
DZ-03_25.d	7.434944	0.53	0.515	0.03	0.04683	376	54
DZ-03_26.d	10.52632	0.53	0.348	0.016	0.21737	375	21
DZ-03_27.d	6.920415	0.4	0.535	0.021	0.36872	369	28
DZ-03_28.d	5.91716	0.43	0.534	0.026	0.35151	444	50
DZ-03_29.d	5.050505	0.42	0.587	0.027	0.029978	423	52
DZ-03_30.d	5.878895	0.31	0.571	0.026	0.23146	386	48
DZ-03_31.d	9.191176	0.6	0.392	0.019	-0.13311	395	26
DZ-03_32.d	10.59322	0.69	0.338	0.02	0.38583	387	31
DZ-03_33.d	4.464286	0.39	0.635	0.074	0.10834	390	160
DZ-03_34.d	10.22495	0.63	0.364	0.024	0.2763	368	32
DZ-03_35.d	10.2459	0.59	0.407	0.02	0.15063	349	26
DZ-03_36.d	10.11122	0.73	0.348	0.018	-0.27687	392	28
DZ-03_37.d	4.761905	0.28	0.646	0.024	0.28327	362	51
DZ-03_38.d	6.868132	0.5	0.523	0.029	0.44552	400	46
DZ-03_39.d	3.125	0.25	0.683	0.026	0.058633	478	80
DZ-03_40.d	10.79914	0.55	0.315	0.016	0.088819	394	25
DZ-03_41.d	5.319149	0.29	0.572	0.021	0.16503	430	44
DZ-03_42.d	7.230658	0.46	0.499	0.022	0.037703	390	32
DZ-03_43.d	6.697924	0.35	0.517	0.023	0.35579	413	40
DZ-03_44.d	8.038585	0.51	0.46	0.016	0.20081	388	29
DZ-03_46.d	8.960573	0.67	0.405	0.014	-0.21752	388	25
Grain	Final 238/206	$2\sigma$	Final 207/206	$2\sigma$	Error Correlation 238/206 vs 207/206	Final 207 Age	$2\sigma$
DZ-04_1.d	8.410429	0.72	0.577	0.044	0.06069	268	48
DZ-04_5.d	8.680556	0.66	0.53	0.043	0.54167	316	47
DZ-04_7.d	2.12766	0.89	0.741	0.047	-0.31112	275	98

DZ-04_8.d	10.04016	0.69	0.493	0.04	0.14327	305	41
DZ-04_12.d	9.689922	0.86	0.486	0.04	0.30532	305	50
DZ-04_13.d	10.41667	0.81	0.484	0.037	0.38791	300	41
DZ-04_14.d	8.090615	0.55	0.545	0.041	0.31879	324	45
DZ-04_23.d	12.13592	0.76	0.359	0.028	0.14055	326	28
DZ-04_24.d	8.680556	0.82	0.478	0.038	0.23462	355	48
DZ-04_25.d	10.69519	0.7	0.42	0.03	0.23856	326	34
DZ-04_26.d	10.33058	0.73	0.462	0.043	0.39084	313	44
DZ-04_27.d	6.622517	0.57	0.56	0.045	0.57756	366	71
DZ-04_29.d	8.510638	0.69	0.522	0.04	0.44555	339	52
DZ-04_30.d	7.507508	0.58	0.559	0.044	0.40639	332	56
DZ-04_35.d	9.13242	0.52	0.453	0.036	0.18539	353	39
DZ-04_36.d	8.787346	0.6	0.463	0.037	0.30765	361	46
DZ-04_40.d	6.944444	0.64	0.588	0.049	0.37596	347	69
DZ-04_42.d	5.128205	0.39	0.626	0.052	0.076186	358	93
DZ-04_45.d	9.033424	0.56	0.481	0.028	0.19732	337	33
Grain	Final 238/206	$2\sigma$	Final 207/206	$2\sigma$	Error Correlation 238/206 vs 207/206	Final 207 Age	$2\sigma$
DZ-05_1.d	6.410256	0.44	0.54	0.033	0.25624	393	53
DZ-05_4.d	4.504505	0.51	0.605	0.039	-0.075904	330	150
DZ-05_6.d	4.166667	0.4	0.614	0.033	0.027239	445	71
DZ-05_7.d	4.62963	0.31	0.594	0.03	0.20315	440	71
DZ-05_8.d	4.950495	0.41	0.567	0.036	0.05386	415	58
DZ-05_9.d	3.861004	0.29	0.682	0.033	0.22796	352	76
DZ-05_12.d	3.378378	0.25	0.692	0.038	0.31127	376	95
DZ-05_13.d	5.347594	0.43	0.588	0.04	0.36875	400	69
DZ-05_14.d	4.1841	0.41	0.622	0.039	0.20627	429	90
DZ-05_16.d	4.366812	0.34	0.618	0.039	0.41904	414	91
DZ-05_17.d	9.532888	0.71	0.359	0.026	0.23419	391	33
DZ-05_20.d	1.908397	0.24	0.764	0.028	-0.016271	360	120
DZ-05_21.d	7.593014	0.36	0.485	0.022	0.26289	378	27
DZ-05_22.d	5.714286	0.36	0.601	0.026	0.24808	349	43
DZ-05_23.d	3.571429	0.2	0.695	0.023	0.29691	313	64
DZ-05_24.d	5.376344	0.41	0.614	0.032	0.16959	349	59
DZ-05_25.d	4.237288	0.19	0.662	0.036	0.25786	356	69
DZ-05_27.d	5.952381	0.44	0.598	0.029	0.1731	337	49
DZ-05_28.d	2.544529	0.2	0.732	0.039	0.28856	350	130
DZ-05_29.d	2.392344	0.16	0.764	0.028	0.2724	300	110
DZ-05_30.d	4	0.37	0.704	0.041	0.007935	310	99
DZ-05_32.d	5.154639	0.4	0.629	0.029	-0.002758	330	48
DZ-05_34.d	4.975124	0.42	0.654	0.039	0.22015	310	83
DZ-05_35.d	2.770083	0.4	0.707	0.036	-0.086184	364	92
DZ-05_37.d	5.714286	0.43	0.593	0.037	0.29618	347	73
DZ-05_38.d	4.926108	0.35	0.601	0.033	-0.26675	383	61
DZ-05_41.d	3.144654	0.19	0.707	0.028	0.11226	389	79
DZ-05_42.d	2.227171	0.19	0.763	0.028	-0.18419	320	100

Grain	Final 238/206	$2\sigma$	Final 207/206	$2\sigma$	Error Correlation 238/206 vs 207/206	Final 207 Age	$2\sigma$
DZ-06_1.d	4.115226	0.29	0.657	0.033	0.24948	363	75
DZ-06_2.d	11.26126	0.82	0.36	0.027	0.33698	337	33
DZ-06_3.d	9.208103	0.58	0.516	0.022	0.51628	287	31
DZ-06_4.d	2.403846	0.15	0.794	0.043	0.38997	190	140
DZ-06_5.d	7.518797	0.34	0.575	0.032	0.2721	287	39
DZ-06_6.d	5.995204	0.3	0.61	0.026	0.3874	317	42
DZ-06_7.d	6.954103	0.46	0.572	0.034	0.29428	313	49
DZ-06_8.d	7.246377	0.63	0.558	0.025	-0.11241	311	34
DZ-06_9.d	10.97695	0.53	0.402	0.017	0.3113	319	20
DZ-06_10.d	2.222222	0.2	0.773	0.046	0.24533	270	170
DZ-06_11.d	12.8866	0.57	0.358	0.018	0.2487	297	19
DZ-06_12.d	12.85347	0.6	0.336	0.017	0.41688	315	21
DZ-06_13.d	7.102273	0.51	0.567	0.034	0.48916	326	48
DZ-06_16.d	6.920415	0.4	0.591	0.023	0.18522	289	38
DZ-06_17.d	9.813543	0.77	0.451	0.024	0.14252	322	37
DZ-06_18.d	6.901311	0.46	0.529	0.036	0.29095	353	59
DZ-06_21.d	3.460208	0.6	0.689	0.032	0.11754	346	83
DZ-06_24.d	12.87001	0.66	0.371	0.019	0.24293	293	20
DZ-06_25.d	8.045052	0.84	0.514	0.074	0.26927	359	81
Grain	Final 238/206	$2\sigma$	Final 207/206	$2\sigma$	Error Correlation 238/206 vs 207/206	Final 207 Age	$2\sigma$
DZ-07_1.d	8.920607	0.437675	0.503	0.026	0.21283	325	32
DZ-07_2.d	4.739336	0.404304	0.707	0.04	0.15518	283	64
DZ-07_3.d	4.878049	0.452112	0.725	0.053	0.29689	287	92
DZ-07_4.d	7.194245	0.828115	0.551	0.058	0.012521	401	84
DZ-07_6.d	8.312552	0.532059	0.489	0.031	-0.40323	336	30
DZ-07_7.d	7.716049	0.535837	0.505	0.034	-0.14042	372	42
DZ-07_9.d	12.2399	0.928854	0.269	0.046	-0.70286	360	20
DZ-07_10.d	8.93655	0.455213	0.49	0.021	0.23409	336	25
DZ-07_12.d	8.510638	0.492531	0.506	0.028	0.11444	335	34
DZ-07_13.d	9.587728	0.597509	0.424	0.024	-0.21495	357	29
DZ-07_15.d	12.8041	0.721358	0.291	0.02	-0.017627	350	22
DZ-07_17.d	5.988024	0.430277	0.622	0.046	0.13951	325	61
DZ-07_18.d	7.89266	0.492123	0.52	0.022	0.29956	353	34
DZ-07_19.d	4.237288	0.395001	0.712	0.036	0.05275	277	69
DZ-07_20.d	6.024096	0.362897	0.593	0.036	-0.043997	362	49
DZ-07_21.d	15.2439	0.859793	0.1311	0.0084	0.5157	373	23
DZ-07_22.d	7.674597	0.424076	0.499	0.022	0.08412	387	36
DZ-07_23.d	7.575758	1.434803	0.475	0.065	-0.029109	410	120
DZ-07_25.d	5.181347	0.375849	0.624	0.038	-0.005993	371	67
DZ-07_27.d	6.451613	0.416233	0.569	0.032	0.11943	373	50
DZ-07_29.d	7.794232	0.3888	0.497	0.028	0.12051	375	34
DZ-07_30.d	6.6357	0.400696	0.546	0.03	0.1062	376	41
DZ-07_32.d	7.199424	0.492401	0.53	0.035	0.055128	381	50
DZ-07_33.d	10.85776	0.825237	0.352	0.04	0.077052	375	44

DZ-07_34.d	6.756757	1.232652	0.468	0.088	0.1495	440	130
DZ-07_38.d	12.30012	0.574914	0.237	0.014	0.35873	398	22
DZ-07_40.d	8.130081	0.859277	0.57	0.072	-0.036694	318	86
DZ-07_43.d	7.462687	0.462241	0.605	0.05	0.55215	310	54
Grain	Final 238/206	$2\sigma$	Final 207/206	$2\sigma$	Error Correlation 238/206 vs 207/206	Final 207 Age	$2\sigma$
DZ-08_1.d	6.373486	0.4	0.501	0.026	0.1083	422	47
DZ-08_2.d	3.891051	0.3	0.683	0.048	0.41218	340	110
DZ-08_3.d	7.968127	0.37	0.434	0.022	0.30786	408	33
DZ-08_5.d	3.095975	0.44	0.668	0.038	0.11915	420	120
DZ-08_6.d	8.474576	0.64	0.413	0.019	-0.34421	390	26
DZ-08_7.d	1.923077	0.16	0.742	0.032	0.20726	420	140
DZ-08_9.d	2.012072	0.14	0.771	0.039	0.37319	310	160
DZ-08_10.d	2.518892	0.13	0.728	0.034	0.1654	340	110
DZ-08_13.d	3.257329	0.22	0.65	0.032	0.16879	463	87
DZ-08_16.d	2.145923	0.21	0.718	0.038	0.042562	440	130
DZ-08_17.d	10.58201	0.35	0.362	0.018	0.27488	361	20
DZ-08_18.d	4.385965	0.27	0.644	0.031	0.17903	371	68
DZ-08_20.d	2.724796	0.27	0.714	0.039	0.22767	350	110
DZ-08_21.d	8.90472	0.56	0.425	0.023	0.018982	369	32
DZ-08_23.d	1.328021	0.11	0.788	0.033	0.35914	280	200
DZ-08_24.d	3.246753	0.21	0.676	0.027	0.35514	420	78
DZ-08_27.d	3.194888	0.44	0.659	0.04	-0.17109	385	98
DZ-08_28.d	3.236246	0.25	0.677	0.029	-0.008078	362	67
DZ-08_30.d	4.098361	0.36	0.67	0.036	0.11998	341	79
DZ-08_33.d	6.024096	0.42	0.606	0.039	0.39733	329	60
DZ-08_35.d	5.665722	0.28	0.58	0.033	0.47595	384	57
DZ-08_38.d	2.739726	0.27	0.677	0.051	0.21479	430	150
DZ-08_40.d	6.968641	0.37	0.53	0.022	0.17239	346	37
DZ-08_41.d	4.608295	0.69	0.576	0.037	-0.32308	427	75
DZ-08_42.d	1.712329	0.17	0.751	0.029	0.20986	410	160
Grain	Final 238/206	$2\sigma$	Final 207/206	$2\sigma$	Error Correlation 238/206 vs 207/206	Final 207 Age	$2\sigma$
DZ-09_1.d	13.31558	0.46	0.265	0.015	0.28266	346	18
DZ-09_3.d	8.764242	0.42	0.437	0.019	0.32025	367	31
DZ-09_5.d	9.541985	0.43	0.415	0.024	0.26981	359	28
DZ-09_6.d	7.107321	0.38	0.529	0.025	0.17641	344	36
DZ-09_7.d	9.009009	0.5	0.421	0.029	-0.14854	364	29
DZ-09_8.d	9.541985	0.52	0.444	0.027	0.52073	336	32
DZ-09_9.d	12.59446	0.45	0.26	0.014	0.16436	366	18
DZ-09_10.d	8.944544	0.61	0.414	0.031	0.26987	385	37
DZ-09_11.d	6.544503	0.44	0.548	0.036	0.44676	375	55
DZ-09_13.d	11.68224	0.61	0.316	0.02	-0.075539	357	20
DZ-09_14.d	6.72043	0.35	0.533	0.033	0.57122	382	51
DZ-09_15.d	11.48106	0.58	0.322	0.017	0.16092	361	21
DZ-09_16.d	13.58696	0.62	0.273	0.018	0.018176	333	18
DZ-09_17.d	12.46883	0.66	0.298	0.022	0.13939	346	28

	Final 238/206	$2\sigma$	Final 207/206	$2\sigma$	Error Correlation 238/206 vs 207/206	Final 207 Age	$2\sigma$	
DZ-09_19.d	13.42282	0.7	0.236	0.022	-0.47821	349	14	
DZ-09_20.d	10.71811	0.45	0.356	0.017	0.14881	359	22	
DZ-09_21.d	9.910803	0.45	0.39	0.029	-0.10761	368	31	
DZ-09_22.d	12.46883	0.6	0.27	0.015	0.34536	361	21	
DZ-09_23.d	9.532888	0.5	0.428	0.024	0.5505	349	32	
DZ-09_24.d	12.43781	0.49	0.256	0.014	0.36936	374	17	
DZ-09_25.d	13.44086	0.42	0.252	0.011	0.20716	350	13	
DZ-09_26.d	11.18568	0.63	0.322	0.014	0.23453	366	25	
DZ-09_27.d	5.208333	0.26	0.641	0.037	0.21323	326	66	
DZ-09_28.d	8.880995	0.4	0.443	0.02	0.30195	362	28	
DZ-09_29.d	5.154639	0.41	0.581	0.042	0.098306	405	88	
DZ-09_30.d	5.208333	0.41	0.612	0.037	0.38156	371	71	
DZ-09_31.d	9.199632	0.53	0.435	0.018	0.44093	359	33	
DZ-09_32.d	7.022472	0.4	0.537	0.034	0.096697	348	45	
DZ-09_34.d	10.1626	0.71	0.357	0.021	-0.1685	386	33	
DZ-09_35.d	12.78772	0.92	0.265	0.022	-0.14103	352	24	
DZ-09_36.d	13.36898	0.66	0.224	0.014	0.10967	359	22	
DZ-09_37.d	12.2549	0.6	0.259	0.014	0.14545	380	22	
DZ-09_38.d	7.423905	0.45	0.504	0.033	-0.020519	377	49	
DZ-09_39.d	7.440476	0.37	0.503	0.028	0.083091	364	36	
DZ-09_40.d	11.52074	0.51	0.303	0.015	0.43692	377	22	
DZ-09_41.d	7.564297	0.82	0.488	0.026	0.053485	378	42	
DZ-09_44.d	11.94743	0.72	0.262	0.015	-0.17333	394	27	
Grain	Final 238/206	$2\sigma$	Final 207/206	$2\sigma$	Error Correlation 238/206 vs 207/206	Final 207 Age	$2\sigma$	
DZ-10_1.d	7.722008	0.39	0.428	0.022	0.18194	371	33	
DZ-10_2.d	5.482456	0.34	0.536	0.041	0.078712	330	71	
DZ-10_3.d	5.750431	0.29	0.519	0.025	0.34892	371	49	
DZ-10_4.d	7.587253	0.32	0.41	0.017	0.46877	400	32	
DZ-10_5.d	4.237288	0.19	0.615	0.027	-0.013581	296	66	
DZ-10_6.d	3.30033	0.18	0.663	0.033	0.53835	240	100	
DZ-10_7.d	5.440696	0.27	0.569	0.032	0.48479	323	61	
DZ-10_8.d	3.984064	0.21	0.646	0.036	0.24933	246	87	
DZ-10_9.d	4.547522	0.21	0.59	0.027	0.20339	322	60	
DZ-10_10.d	3.344482	0.15	0.657	0.028	0.30993	262	80	
DZ-10_11.d	4.62963	0.36	0.565	0.035	0.22996	355	68	
DZ-10_12.d	3.436426	0.15	0.639	0.025	0.43067	298	76	
DZ-10_14.d	4.081633	0.23	0.603	0.026	0.22222	335	64	
DZ-10_15.d	6.891799	0.26	0.479	0.021	0.42639	356	32	
DZ-10_16.d	4.842615	0.24	0.547	0.022	0.36592	374	49	
DZ-10_17.d	4.405286	0.19	0.587	0.03	0.34101	347	65	
DZ-10_18.d	6.064281	0.33	0.498	0.027	0.37129	383	47	
DZ-10_19.d	1.785714	0.11	0.759	0.03	0.43675	-40	160	
DZ-10_20.d	2.985075	0.18	0.682	0.032	0.20119	230	110	
DZ-10_21.d	2.95858	0.15	0.686	0.03	0.23173	217	96	
DZ-10_24.d	3.717472	0.17	0.628	0.028	0.20309	311	73	

DZ-10_25.d	4.081633	0.15	0.616	0.03	0.49035	313	69
DZ-10_26.d	6.472492	0.25	0.493	0.02	0.095111	357	36
DZ-10_27.d	2.923977	0.18	0.656	0.031	0.35633	320	100
DZ-10_29.d	2.673797	0.22	0.698	0.032	0.016036	170	120
DZ-10_30.d	2.610966	0.18	0.689	0.037	0.33241	250	130
DZ-10_31.d	2.150538	0.13	0.723	0.044	0.20385	150	180
DZ-10_33.d	1.980198	0.15	0.713	0.045	0.30336	210	220
DZ-10_34.d	2.415459	0.12	0.702	0.036	0.3839	210	140
DZ-10_35.d	2.487562	0.21	0.708	0.042	0.43462	190	160
DZ-10_37.d	3.322259	0.21	0.673	0.036	0.47806	234	97
DZ-10_40.d	4.098361	0.24	0.631	0.039	0.38351	277	87
DZ-10_41.d	2.087683	0.13	0.737	0.036	0.43857	90	150
DZ-10_42.d	5.51572	0.27	0.561	0.026	0.16322	312	52
Grain	Final 238/206	$2\sigma$	Final 207/206	$2\sigma$	Error Correlation 238/206 vs 207/206	Final 207 Age	$2\sigma$
DZ-11_1.d	1.390821	0.14	0.787	0.034	0.23656	300	210
DZ-11_3.d	2.564103	0.29	0.708	0.037	0.11372	410	120
DZ-11_4.d	5.136107	0.28	0.56	0.023	0.10458	427	43
DZ-11_6.d	2.570694	0.091	0.697	0.022	0.25196	444	73
DZ-11_7.d	3.745318	0.18	0.645	0.021	0.14875	412	55
DZ-11_8.d	5.073567	0.23	0.586	0.023	0.19248	398	47
DZ-11_9.d	5.29661	0.21	0.561	0.022	0.1509	421	40
DZ-11_10.d	5.291005	0.37	0.577	0.027	0.007272	380	39
DZ-11_11.d	3.125	0.28	0.666	0.027	0.29831	446	94
DZ-11_12.d	7.61035	0.33	0.445	0.027	0.062465	419	39
DZ-11_13.d	3.717472	0.25	0.63	0.033	0.19758	446	77
DZ-11_14.d	1.984127	0.12	0.72	0.034	0.33252	510	140
DZ-11_15.d	3.861004	0.2	0.651	0.027	0.2879	404	67
DZ-11_16.d	4.291845	0.24	0.594	0.021	0.31581	454	48
DZ-11_17.d	3.90625	0.2	0.633	0.027	0.22571	415	58
DZ-11_18.d	3.412969	0.19	0.636	0.031	0.4751	493	87
DZ-11_19.d	3.215434	0.5	0.623	0.026	-0.1053	464	71
DZ-11_20.d	2.48139	0.11	0.702	0.028	0.41984	470	100
DZ-11_21.d	3.484321	0.24	0.69	0.035	0.39016	382	97
DZ-11_22.d	1.508296	0.21	0.723	0.025	0.1651	650	140
DZ-11_23.d	1.30039	0.13	0.778	0.048	0.25627	340	310
DZ-11_25.d	4.761905	0.2	0.599	0.023	0.40723	412	48
DZ-11_27.d	2.631579	0.14	0.679	0.027	0.35455	473	90
DZ-11_28.d	1.396648	0.1	0.766	0.035	0.2484	390	220
DZ-11_29.d	4.113534	0.16	0.607	0.024	0.11145	456	56
DZ-11_31.d	2.770083	0.26	0.673	0.027	0.10891	462	80
DZ-11_32.d	3.164557	0.19	0.688	0.027	0.35708	391	73
DZ-11_33.d	3.571429	0.16	0.623	0.022	0.3763	492	57
DZ-11_35.d	3.90625	0.28	0.68	0.033	0.2299	330	72
DZ-11_37.d	2.10084	0.15	0.689	0.027	0.15081	540	100
DZ-11_38.d	3.076923	0.19	0.661	0.029	0.47684	494	90

DZ-11_39.d	1.831502	0.16	0.755	0.031	0.2028	420	130
DZ-11_40.d	5.724098	0.21	0.515	0.021	0.22008	444	37
DZ-11_41.d	3.558719	0.2	0.654	0.024	0.39389	423	64
Grain	Final 238/206	$2\sigma$	Final 207/206	$2\sigma$	Error Correlation 238/206 vs 207/206	Final 207 Age	$2\sigma$
DZ-12_1.d	4.446421	0.15	0.668	0.021	0.38919	279	42
DZ-12_3.d	3.003003	0.21	0.719	0.019	-0.22343	249	61
DZ-12_5.d	4.486317	0.19	0.651	0.023	0.040908	301	45
DZ-12_6.d	4.08998	0.16	0.706	0.027	0.50153	232	62
DZ-12_7.d	7.479432	0.32	0.563	0.027	0.49403	286	35
DZ-12_8.d	6.067961	0.37	0.624	0.022	-0.14575	257	35
DZ-12_9.d	4.524887	0.24	0.66	0.032	0.2474	283	64
DZ-12_10.d	2.710027	0.13	0.734	0.024	0.35235	258	76
DZ-12_12.d	5.608525	0.3	0.659	0.029	0.33855	231	52
DZ-12_13.d	2.702703	0.23	0.744	0.025	0.15783	225	82
DZ-12_17.d	1.162791	0.17	0.836	0.077	0.067571	240	230
DZ-12_19.d	2.293578	0.14	0.696	0.039	0.29156	450	150
DZ-12_20.d	2.380952	0.22	0.752	0.029	-0.16484	191	98
DZ-12_26.d	5.38503	0.25	0.626	0.027	0.29989	296	47
DZ-12_31.d	1.795332	0.08	0.746	0.021	0.40858	336	99
DZ-12_39.d	3.571429	0.85	0.652	0.057	-0.054356	400	140
DZ-12_42.d	3.134796	0.18	0.721	0.031	0.42082	271	90
DZ-12_43.d	1.73913	0.13	0.777	0.023	0.16253	210	110
DZ-12_44.d	2.380952	0.54	0.75	0.15	0.25063	110	400
Grain	Final 238/206	$2\sigma$	Final 207/206	$2\sigma$	Error Correlation 238/206 vs 207/206	Final 207 Age	$2\sigma$
DZ-13_1.d	13.83126	0.5	0.353	0.016	0.33389	270	17
DZ-13_2.d	15.92357	0.66	0.257	0.017	0.39685	286	16
DZ-13_4.d	10.12146	0.59	0.518	0.033	0.44728	246	39
DZ-13_5.d	12.36094	0.52	0.391	0.021	0.41948	282	24
DZ-13_6.d	8.403361	0.47	0.497	0.029	0.34512	296	39
DZ-13_7.d	10.46025	0.37	0.455	0.017	0.24674	274	19
DZ-13_8.d	15.26718	0.59	0.293	0.014	0.44565	280	15
DZ-13_10.d	12.65823	0.71	0.349	0.015	0.31406	294	19
DZ-13_12.d	13.28021	0.78	0.355	0.023	0.47658	284	26
DZ-13_13.d	14.53488	0.65	0.325	0.017	0.33693	273	18
DZ-13_14.d	11.24859	0.62	0.459	0.023	0.38583	256	24
DZ-13_15.d	14.1844	0.61	0.33	0.016	0.39093	281	18
DZ-13_17.d	17.92115	0.55	0.226	0.01	0.32844	267	11
DZ-13_18.d	11.75088	0.53	0.423	0.022	0.21609	269	21
DZ-13_19.d	12.97017	0.66	0.41	0.021	0.34017	250	21
DZ-13_20.d	11.65501	0.55	0.421	0.016	0.04937	267	19
DZ-13_21.d	12.93661	0.52	0.367	0.016	0.30615	280	17
DZ-13_22.d	9.891197	0.39	0.485	0.028	0.58049	271	31
DZ-13_23.d	13.5318	0.68	0.378	0.019	0.24138	260	20
DZ-13_24.d	13.45895	0.48	0.352	0.015	-0.000266	278	14
DZ-13_25.d	11.44165	0.52	0.438	0.019	0.097238	265	22

DZ-13_26.d	10.92896	0.41	0.437	0.019	0.41641	274	19
DZ-13_27.d	12.30012	0.68	0.348	0.02	-0.022304	302	21
DZ-13_28.d	15.4321	0.64	0.274	0.011	0.36836	288	15
DZ-13_30.d	12.04819	0.34	0.41	0.015	0.33421	271	15
DZ-13_31.d	15.29052	0.56	0.271	0.013	-0.15828	288	10
DZ-13_32.d	13.947	0.58	0.354	0.017	-0.039164	268	17
DZ-13_33.d	12.57862	0.42	0.382	0.016	0.37686	279	16
DZ-13_34.d	12.0048	0.44	0.404	0.021	0.21565	277	20
DZ-13_38.d	9.569378	0.4	0.489	0.03	0.22212	269	34
DZ-13_39.d	18.31502	0.78	0.205	0.011	0.076375	272	12
DZ-13_40.d	13.29787	0.56	0.382	0.014	0.16933	261	16
DZ-13_42.d	10.5042	0.42	0.475	0.023	0.29711	254	21
DZ-13_43.d	13.71742	0.64	0.352	0.02	0.30458	271	18
DZ-13_44.d	8.103728	0.41	0.542	0.03	0.44	274	39
DZ-13_45.d	13.2626	0.47	0.363	0.016	0.26086	272	14
Grain	Final 238/206	$2\sigma$	Final 207/206	$2\sigma$	Error Correlation 238/206 vs 207/206	Final 207 Age	$2\sigma$
DZ-14_1.d	4.405286	0.26	0.72	0.04	0.59332	316	71
DZ-14_2.d	6.21118	0.27	0.659	0.029	0.24089	291	39
DZ-14_3.d	3.215434	0.16	0.743	0.033	0.35008	339	74
DZ-14_4.d	4.714757	0.27	0.684	0.037	0.34975	340	61
DZ-14_5.d	5.586592	0.43	0.631	0.03	0.39107	375	67
DZ-14_6.d	5.614823	0.26	0.654	0.032	0.23358	334	48
DZ-14_7.d	3.717472	0.25	0.707	0.045	0.60106	423	94
DZ-14_8.d	4.166667	0.23	0.72	0.035	0.54113	328	73
DZ-14_10.d	3.861004	0.2	0.719	0.033	0.5511	370	76
DZ-14_12.d	3.623188	0.2	0.736	0.036	0.32858	352	79
DZ-14_14.d	6.98324	0.34	0.597	0.026	0.33144	327	35
DZ-14_16.d	4.264392	0.19	0.698	0.031	0.53959	344	65
DZ-14_17.d	4.273504	0.28	0.72	0.031	0.37547	316	64
DZ-14_18.d	3.355705	0.19	0.737	0.027	0.40461	350	59
DZ-14_20.d	3.984064	0.53	0.686	0.035	-0.23467	364	79
DZ-14_21.d	7.122507	0.34	0.586	0.025	0.46583	338	35
DZ-14_23.d	4.098361	0.21	0.738	0.035	0.11252	317	69
DZ-14_24.d	5.252101	0.27	0.647	0.03	0.22102	336	53
DZ-14_25.d	5.847953	0.32	0.647	0.043	0.40453	337	63
DZ-14_26.d	5.649718	0.29	0.618	0.031	0.52074	379	55
DZ-14_27.d	5.208333	0.29	0.626	0.044	0.40543	407	74
DZ-14_29.d	5	0.3	0.625	0.031	0.10824	430	55
DZ-14_30.d	4.56621	0.25	0.687	0.032	0.086556	347	57
DZ-14_31.d	4.659832	0.2	0.67	0.029	0.3514	377	56
DZ-14_32.d	3.571429	0.2	0.739	0.035	0.46085	359	85
DZ-14_34.d	3.937008	0.19	0.715	0.031	0.37996	360	64
DZ-14_35.d	4.90918	0.24	0.684	0.028	0.31185	325	47
DZ-14_36.d	5.333333	0.26	0.631	0.031	0.45391	376	49
DZ-14_37.d	5.025126	0.26	0.676	0.031	0.33664	344	53

DZ-14_38.d	3.546099	0.16	0.721	0.033	0.58173	398	78
DZ-14_39.d	4.56621	0.41	0.722	0.024	0.12017	298	51
DZ-14_40.d	7.974482	0.3	0.535	0.021	0.38283	339	28
DZ-14_41.d	4.901961	0.26	0.637	0.029	0.4271	410	54
DZ-14_42.d	4.098361	0.27	0.711	0.034	0.19402	345	72
DZ-14_43.d	3.610108	0.19	0.746	0.04	0.36438	322	87
Grain	Final 238/206	$2\sigma$	Final 207/206	$2\sigma$	Error Correlation 238/206 vs 207/206	Final 207 Age	$2\sigma$
DZ-15_1.d	3.802281	0.26	0.604	0.03	0.31278	369	85
DZ-15_2.d	1.639344	0.11	0.692	0.032	0.29279	440	180
DZ-15_3.d	3.067485	0.2	0.665	0.031	0.17186	290	90
DZ-15_4.d	2.754821	0.22	0.657	0.029	0.06524	361	99
DZ-15_6.d	3.355705	0.23	0.61	0.031	0.29482	426	88
DZ-15_7.d	1.652893	0.14	0.711	0.036	0.19156	340	200
DZ-15_8.d	2.178649	0.17	0.696	0.034	0.54789	290	160
DZ-15_9.d	2.932551	0.17	0.631	0.028	-0.17452	389	92
DZ-15_11.d	1.841621	0.11	0.68	0.028	0.16123	410	140
DZ-15_12.d	1.782531	0.13	0.671	0.035	0.38507	450	170
DZ-15_13.d	1.801802	0.12	0.698	0.033	0.25517	320	160
DZ-15_14.d	1.785714	0.15	0.705	0.035	0.23583	310	180
DZ-15_15.d	2.257336	0.15	0.677	0.036	0.20581	340	150
DZ-15_16.d	2.207506	0.14	0.659	0.028	0.18177	440	120
DZ-15_17.d	1.748252	0.16	0.685	0.028	0.058096	370	140
DZ-15_18.d	2.680965	0.2	0.651	0.029	0.33217	400	110
DZ-15_19.d	1.331558	0.095	0.723	0.03	0.058991	230	190
DZ-15_20.d	1.869159	0.14	0.713	0.035	0.31717	310	190
DZ-15_21.d	1.872659	0.13	0.704	0.032	0.17652	280	170
DZ-15_22.d	3.08642	0.22	0.628	0.023	0.26358	399	78
DZ-15_23.d	1.834862	0.13	0.685	0.032	0.28771	420	180
DZ-15_24.d	2.314815	0.13	0.678	0.027	0.37993	350	110
DZ-15_25.d	2.212389	0.13	0.673	0.028	0.35357	370	120
DZ-15_26.d	2.427184	0.23	0.671	0.029	0.10962	360	110
DZ-15_27.d	3.773585	0.19	0.587	0.033	0.021528	412	85
DZ-15_28.d	2.169197	0.16	0.65	0.028	0.18987	490	120
DZ-15_31.d	2.020202	0.21	0.658	0.054	0.023033	390	150
DZ-15_32.d	1.647446	0.13	0.735	0.058	-0.045717	290	180
DZ-15_33.d	3.436426	0.18	0.614	0.026	0.10108	395	73
DZ-15_34.d	1.55521	0.1	0.724	0.035	0.25615	240	200
DZ-15_36.d	1.308901	0.098	0.725	0.031	0.29982	290	190
DZ-15_37.d	1.557632	0.11	0.729	0.031	0.066493	140	200
DZ-15_38.d	2.020202	0.14	0.696	0.025	0.22828	300	110
DZ-15_40.d	1.451379	0.11	0.704	0.031	0.032199	350	190
DZ-15_41.d	1.703578	0.13	0.676	0.035	0.35679	410	160
DZ-15_42.d	2.267574	0.18	0.662	0.029	0.054733	410	130
Grain	Final 238/206	$2\sigma$	Final 207/206	$2\sigma$	Error Correlation 238/206 vs 207/206	Final 207 Age	$2\sigma$
DZ-16_1.d	4.166667	0.29	0.631	0.042	0.23426	270	100

DZ-16_2.d	4.504505	0.53	0.587	0.036	0.15668	317	81
DZ-16_5.d	3.787879	0.31	0.629	0.034	0.3155	287	97
DZ-16_6.d	3.436426	0.32	0.649	0.037	0.24576	290	110
DZ-16_7.d	4.56621	0.31	0.627	0.03	0.42947	252	66
DZ-16_8.d	5.347594	0.34	0.578	0.031	0.36182	299	62
DZ-16_9.d	8.123477	0.46	0.499	0.021	0.10485	275	29
DZ-16_10.d	6.369427	0.75	0.516	0.024	-0.031171	308	45
DZ-16_11.d	6.622517	0.37	0.561	0.03	0.24685	258	45
DZ-16_12.d	10.12146	0.62	0.414	0.026	0.36794	302	32
DZ-16_13.d	5.847953	0.41	0.583	0.032	0.28144	266	63
DZ-16_14.d	12.16545	0.74	0.382	0.022	0.38946	269	27
DZ-16_15.d	4.132231	0.35	0.615	0.041	0.4276	310	91
DZ-16_16.d	4.524887	0.46	0.632	0.039	0.31136	220	80
DZ-16_18.d	3.636364	0.29	0.677	0.041	0.42583	210	110
DZ-16_20.d	4.132231	0.28	0.658	0.035	-0.024065	184	86
DZ-16_21.d	3.875969	0.27	0.67	0.034	0.31221	193	92
DZ-16_24.d	10.22495	0.6	0.425	0.027	0.40734	282	31
DZ-16_27.d	4.608295	0.3	0.618	0.029	0.2908	265	68
DZ-16_28.d	3.424658	0.25	0.648	0.03	0.15391	256	88
DZ-16_29.d	6.896552	0.67	0.55	0.026	-0.077232	241	39
DZ-16_30.d	4.926108	0.66	0.577	0.036	-0.39933	264	70
DZ-16_31.d	3.891051	0.3	0.647	0.027	0.45659	248	66
DZ-16_32.d	10.38422	0.69	0.423	0.02	0.30653	279	28
DZ-16_36.d	8.658009	0.4	0.501	0.021	0.30234	255	26
DZ-16_38.d	14.51379	0.65	0.275	0.01	0.46753	294	16
DZ-16_39.d	7.806401	0.45	0.525	0.025	0.16423	251	34
DZ-16_40.d	7.7101	0.38	0.505	0.018	0.32525	281	26
DZ-16_41.d	12.78772	0.42	0.376	0.017	0.57658	261	17
DZ-16_43.d	5.747126	0.33	0.587	0.024	0.13221	240	43
DZ-16_44.d	6.622517	0.54	0.516	0.026	0.099892	317	45
DZ-16_45.d	4.149378	0.36	0.627	0.039	0.26167	290	100
DZ-16_46.d	3.412969	0.26	0.651	0.03	0.27003	268	81
Grain	Final 238/206	$2\sigma$	Final 207/206	$2\sigma$	Error Correlation 238/206 vs 207/206	Final 207 Age	$2\sigma$
DZ-17_3.d	11.6144	1.1	0.371	0.03	0.16245	309	35
DZ-17_4.d	11.99041	0.75	0.374	0.027	0.25659	305	28
DZ-17_6.d	12.5	0.86	0.372	0.022	0.13637	286	23
DZ-17_7.d	12.04819	2.4	0.28	0.033	0.5449	345	45
DZ-17_8.d	11.82033	0.65	0.347	0.023	0.31943	324	24
DZ-17_10.d	2.083333	0.83	0.675	0.054	-0.2641	310	190
DZ-17_14.d	4.484305	1.6	0.65	0.11	-0.052194	340	180
DZ-17_18.d	12.10654	0.88	0.359	0.023	0.24951	304	30
DZ-17_22.d	8.920607	0.91	0.465	0.042	0.3889	322	56
DZ-17_25.d	9.615385	0.96	0.431	0.043	-0.48151	299	35
DZ-17_26.d	10.29866	0.81	0.406	0.029	0.40523	313	42
DZ-17_29.d	12.97017	1.1	0.346	0.031	0.20572	296	34

DZ-17_30.d	10.92896	0.97	0.379	0.028	0.28563	334	37
DZ-17_36.d	14.94768	0.84	0.27	0.021	0.13774	297	21
DZ-17_38.d	6.666667	0.64	0.57	0.034	0.05662	287	53
Grain	Final 238/206	$2\sigma$	Final 207/206	$2\sigma$	Error Correlation 238/206 vs 207/206	Final 207 Age	$2\sigma$
DZ-18_1.d	1.298701	0.17	0.701	0.059	0.033729	80	400
DZ-18_5.d	5.524862	0.45	0.577	0.033	0.26941	293	59
DZ-18_6.d	8.726003	0.46	0.476	0.021	-0.043787	274	31
DZ-18_10.d	2.583979	0.23	0.672	0.039	0.28453	310	130
DZ-18_11.d	1.468429	0.21	0.668	0.057	0.098759	570	240
DZ-18_13.d	2.45098	0.23	0.704	0.046	0.23539	130	160
DZ-18_14.d	2.570694	0.31	0.628	0.039	0.35805	460	140
DZ-18_15.d	3.846154	0.3	0.654	0.036	0.297	230	100
DZ-18_17.d	5.889282	0.35	0.575	0.026	0.47924	265	49
DZ-18_19.d	3.597122	0.55	0.621	0.083	0.30712	410	180
DZ-18_20.d	2.724796	0.26	0.652	0.03	0.48421	320	110
DZ-18_22.d	8.503401	0.69	0.49	0.032	0.26904	291	46
DZ-18_23.d	9.569378	0.78	0.443	0.028	0.21581	294	34
DZ-18_25.d	2.132196	0.17	0.708	0.034	0.073618	190	150
DZ-18_26.d	3.773585	0.23	0.634	0.039	0.48378	310	100
DZ-18_27.d	2.583979	0.16	0.68	0.034	0.3478	260	130
DZ-18_36.d	3.521127	0.34	0.646	0.042	0.11944	270	120
DZ-18_39.d	4.132231	1.5	0.648	0.039	0.15041	250	120
DZ-18_40.d	3.278689	0.4	0.6	0.034	-0.15781	330	100
DZ-18_41.d	2.645503	0.21	0.664	0.037	0.12098	240	120
Grain	Final 238/206	$2\sigma$	Final 207/206	$2\sigma$	Error Correlation 238/206 vs 207/206	Final 207 Age	$2\sigma$
DZ-19_1.d	2.222222	0.12	0.676	0.024	0.1476	376	99
DZ-19_5.d	4.950495	0.27	0.521	0.02	0.33741	427	50
DZ-19_6.d	9.940358	0.78	0.339	0.023	-0.13244	376	33
DZ-19_8.d	3.745318	0.21	0.588	0.016	0.18091	425	49
DZ-19_10.d	1.272265	0.068	0.678	0.022	0.17646	660	170
DZ-19_11.d	1.440922	0.37	0.691	0.038	0.086618	500	250
DZ-19_12.d	3.215434	0.16	0.623	0.024	0.21758	410	72
DZ-19_18.d	1.901141	0.15	0.706	0.032	0.24739	290	150
DZ-19_19.d	3.731343	0.25	0.582	0.025	0.44825	460	68
DZ-19_20.d	8.4246	0.61	0.346	0.012	0.015823	438	27
DZ-19_23.d	1.172333	0.11	0.717	0.029	0.20653	430	220
DZ-19_26.d	1.324503	0.11	0.704	0.033	-0.010622	470	190
DZ-19_34.d	2.659574	0.15	0.619	0.02	0.3986	496	81
DZ-19_36.d	0.934579	0.067	0.732	0.035	0.021473	330	310
DZ-19_37.d	2.583979	0.16	0.648	0.024	0.49001	440	92
Grain	Final 238/206	$2\sigma$	Final 207/206	$2\sigma$	Error Correlation 238/206 vs 207/206	Final 207 Age	$2\sigma$
DZ-20_1.d	6.944444	0.5	0.524	0.048	0.33483	354	67
DZ-20_2.d	0.934579	0.13	0.724	0.028	0.09587	550	260
DZ-20_3.d	6.009615	0.34	0.507	0.023	0.39836	409	44

DZ-20_4.d	6.127451	0.36	0.535	0.05	0.54199	402	87
DZ-20_5.d	13.12336	0.71	0.226	0.016	0.23303	367	24
DZ-20_6.d	8.56898	0.57	0.444	0.024	0.40584	362	38
DZ-20_7.d	5.555556	0.39	0.56	0.032	0.29972	339	61
DZ-20_9.d	12.82051	0.57	0.261	0.015	0.21801	359	22
DZ-20_10.d	8.865248	0.7	0.44	0.029	0.26475	357	46
DZ-20_11.d	9.0009	0.58	0.472	0.028	0.10868	307	35
DZ-20_13.d	8.438819	0.6	0.422	0.032	0.42665	380	52
DZ-20_15.d	8.312552	0.4	0.438	0.021	0.091636	366	29
DZ-20_17.d	6.289308	0.58	0.501	0.036	0.50188	410	64
DZ-20_20.d	7.616146	0.61	0.469	0.029	0.36293	370	46
DZ-20_21.d	6.024096	0.48	0.554	0.037	0.54453	372	65
DZ-20_22.d	3.333333	0.59	0.592	0.046	0.18368	450	150
DZ-20_24.d	6.410256	0.56	0.536	0.047	0.61761	374	69
DZ-20_26.d	6.540222	0.39	0.538	0.031	0.27261	324	48
DZ-20_30.d	6.747638	0.47	0.507	0.036	0.42888	376	63
DZ-20_31.d	10.76426	0.8	0.293	0.023	-0.072522	399	34
DZ-20_32.d	5.586592	0.4	0.584	0.04	0.27275	320	69
DZ-20_33.d	6.896552	0.56	0.493	0.041	0.36441	376	60
DZ-20_34.d	5.882353	0.58	0.618	0.07	0.34146	310	110
DZ-20_36.d	5.025126	0.29	0.553	0.046	0.48819	435	85
DZ-20_37.d	5.319149	0.54	0.543	0.05	0.56418	430	100
DZ-20_39.d	9.107468	0.6	0.409	0.032	0.12883	368	43
DZ-20_40.d	6.622517	0.55	0.469	0.029	0.17526	415	47
DZ-20_41.d	2.898551	0.29	0.665	0.051	0.46396	420	130
DZ-20_43.d	6.535948	0.54	0.524	0.028	0.19077	364	51
DZ-20_44.d	5.181347	0.43	0.597	0.044	0.47897	358	83
DZ-20_47.d	6.807352	0.45	0.513	0.035	0.21822	357	54
DZ-20_48.d	5.714286	0.38	0.554	0.039	0.29361	371	68
Grain	Final 238/206	$2\sigma$	Final 207/206	$2\sigma$	Error Correlation 238/206 vs 207/206	Final 207 Age	$2\sigma$
DZ-21_2.d	7.358352	0.52	0.398	0.027	0.39072	464	58
DZ-21_3.d	6.211118	0.57	0.456	0.027	0.41277	435	53
DZ-21_4.d	10.89325	0.65	0.1956	0.0075	0.27216	459	26
DZ-21_5.d	5.025126	0.38	0.506	0.022	0.17302	460	54
DZ-21_6.d	6.98324	0.56	0.429	0.031	0.3119	441	55
DZ-21_8.d	3.861004	0.35	0.568	0.031	0.12148	448	79
DZ-21_9.d	1.703578	0.12	0.686	0.037	0.52537	490	190
DZ-21_10.d	5.906675	0.39	0.478	0.022	0.21836	440	45
DZ-21_14.d	6.455778	0.39	0.429	0.021	0.4649	455	44
DZ-21_15.d	6.341154	0.44	0.436	0.024	0.28655	468	48
DZ-21_16.d	6.925208	0.44	0.423	0.022	0.40629	440	46
DZ-21_17.d	7.680492	0.39	0.372	0.014	0.12178	450	30
DZ-21_19.d	4.587156	0.39	0.55	0.044	0.3089	456	98
DZ-21_23.d	7.70416	0.56	0.368	0.028	0.40801	463	50
DZ-21_24.d	3.875969	0.54	0.508	0.051	0.009096	530	170

DZ-21_25.d	6.578947	0.55	0.447	0.033	0.12169	444	64
DZ-21_26.d	6.060606	0.63	0.484	0.046	0.37186	411	94
DZ-21_31.d	3.984064	0.26	0.58	0.032	0.20683	434	74
DZ-21_32.d	5.319149	0.4	0.474	0.035	0.34301	492	67
DZ-21_34.d	4.807692	0.45	0.448	0.039	0.55022	600	110
DZ-21_35.d	1.204819	0.47	0.69	0.12	0.31353	150	550
DZ-21_36.d	7.102273	0.41	0.406	0.034	0.24321	450	55
DZ-21_37.d	5	0.28	0.522	0.035	0.26335	450	74
DZ-21_39.d	3.787879	0.28	0.578	0.03	0.091325	452	78
DZ-21_40.d	4.237288	0.73	0.57	0.094	0.52861	460	170
DZ-21_41.d	3.134796	0.57	0.55	0.051	0.022205	610	140
DZ-21_42.d	2.724796	0.33	0.602	0.051	0.2188	530	190
DZ-21_43.d	5.580357	0.29	0.477	0.02	0.011146	458	43
DZ-21_44.d	3.831418	0.53	0.523	0.055	0.13931	500	150
Grain	Final 238/206	$2\sigma$	Final 207/206	$2\sigma$	Error Correlation 238/206 vs 207/206	Final 207 Age	$2\sigma$
DZ-22b_6.d	12.42236	0.49	0.27	0.014	0.18283	375	20
DZ-22b_7.d	8.756567	0.46	0.41	0.024	0.31198	412	34
DZ-22b_11.d	6.574622	0.42	0.516	0.031	0.36941	424	57
DZ-22b_17.d	5.235602	0.44	0.562	0.043	0.31679	462	80
DZ-22b_18.d	8.1103	0.38	0.498	0.035	0.25647	364	41
DZ-22b_27.d	11.49425	0.73	0.347	0.022	0.42753	358	28
DZ-22b_29.d	8.032129	0.56	0.517	0.031	0.21808	350	40
DZ-22b_30.d	11.16071	0.5	0.322	0.02	0.026137	378	21
DZ-22b_31.d	10.35197	0.83	0.329	0.033	-0.40169	391	27
DZ-22b_36.d	8.510638	0.45	0.496	0.033	0.50552	350	38
DZ-22b_38.d	9.11577	0.68	0.43	0.025	0.30467	381	35
DZ-22b_41.d	9.165903	0.66	0.43	0.032	-0.42631	364	32
DZ-22b_45.d	10.1626	0.74	0.388	0.026	-0.16363	364	31
DZ-22b_48.d	4	0.29	0.658	0.038	0.13227	429	80
DZ-22b_49.d	5.882353	0.49	0.556	0.033	-0.15722	411	48
DZ-22b_55.d	10.29866	0.4	0.372	0.016	0.27837	375	21
DZ-22b_60.d	2.73224	0.41	0.732	0.087	0.20921	450	240
DZ-22b_62.d	5.810575	0.31	0.615	0.032	0.26436	354	48
DZ-22b_67.d	4.830918	0.83	0.627	0.044	0.14147	388	81
DZ-22b_69.d	8.688097	0.53	0.456	0.035	0.4904	365	37
DZ-22b_70.d	8.169935	0.64	0.493	0.035	0.32582	377	52
DZ-22b_71.d	6.666667	0.45	0.552	0.041	0.39315	401	63
DZ-22b_73.d	8.635579	0.51	0.484	0.026	0.3647	354	31
DZ-22b_75.d	5.91716	0.4	0.612	0.036	0.24708	356	57
DZ-22b_87.d	3.952569	0.27	0.698	0.056	0.51253	370	110
DZ-22b_89.d	9.259259	0.59	0.397	0.034	0.41157	394	40
DZ-22b_94.d	4.716981	0.43	0.661	0.047	0.42508	367	88
DZ-22b_95.d	3.10559	0.28	0.725	0.045	0.24972	400	110
Grain	Final 238/206	$2\sigma$	Final 207/206	$2\sigma$	Error Correlation 238/206 vs 207/206	Final 207 Age	$2\sigma$
DZ-23b_1.d	5.376344	0.42	0.601	0.04	0.41465	384	71

DZ-23b_7.d	3.496503	0.25	0.693	0.031	0.43363	403	91
DZ-23b_11.d	10.12146	0.62	0.38	0.028	0.41272	370	37
DZ-23b_13.d	5.291005	0.36	0.571	0.027	0.20467	419	56
DZ-23b_15.d	5.917116	0.64	0.537	0.032	-0.33233	404	50
DZ-23b_17.d	2.666667	0.18	0.712	0.035	0.42941	450	110
DZ-23b_18.d	7.830854	0.41	0.5	0.026	0.15242	352	32
DZ-23b_21.d	10.64963	0.91	0.311	0.029	-0.083689	401	39
DZ-23b_23.d	5.208333	0.3	0.61	0.031	0.39451	379	58
DZ-23b_27.d	4.132231	0.25	0.651	0.036	0.61317	405	87
DZ-23b_29.d	4.385965	0.26	0.633	0.032	0.4014	402	66
DZ-23b_37.d	5.291005	0.32	0.608	0.03	0.41671	380	55
DZ-23b_42.d	4.132231	0.2	0.65	0.027	0.35873	390	59
DZ-23b_45.d	2.09205	0.095	0.748	0.023	0.35715	399	98
DZ-23b_46.d	2.873563	0.22	0.698	0.034	0.50869	460	100
DZ-23b_48.d	7.127584	0.31	0.479	0.022	0.10457	414	32
DZ-23b_49.d	10.29866	0.75	0.356	0.028	-0.049763	375	37
DZ-23b_50.d	3.355705	0.2	0.706	0.032	0.25217	333	80
DZ-23b_51.d	6.369427	0.49	0.505	0.032	0.30407	431	52
DZ-23b_53.d	3.861004	0.18	0.662	0.028	0.19522	370	61
DZ-23b_72.d	3.571429	0.21	0.69	0.036	0.3133	370	82
DZ-23b_76.d	8.354219	0.46	0.446	0.028	0.08287	383	37
DZ-23b_77.d	3.831418	0.19	0.651	0.035	0.31802	393	79
DZ-23b_78.d	2.673797	0.12	0.73	0.025	0.34309	379	81
DZ-23b_81.d	10.15228	0.7	0.346	0.032	-0.51976	364	24
DZ-23b_82.d	3.267974	0.35	0.714	0.031	-0.054078	309	80
DZ-23b_88.d	8.216927	0.4	0.444	0.019	0.15522	386	28
DZ-23b_91.d	3.267974	0.22	0.695	0.035	0.32309	384	89
DZ-23b_92.d	3.174603	0.19	0.714	0.035	0.38263	356	92
DZ-23b_98.d	7.092199	0.59	0.513	0.035	-0.48464	356	37
DZ-23b_99.d	2.444988	0.14	0.713	0.03	0.26311	470	110
DZ-23b_103.d	5.208333	0.29	0.655	0.034	0.38461	306	60
DZ-23b_104.d	3.558719	0.19	0.667	0.035	0.36902	402	80
DZ-23b_108.d	4.761905	0.25	0.662	0.034	0.31604	333	64
Grain	Final 238/206	$2\sigma$	Final 207/206	$2\sigma$	Error Correlation 238/206 vs 207/206	Final 207 Age	$2\sigma$
DZ-24b_1.d	8.849558	0.47	0.473	0.029	0.27522	342	35
DZ-24b_2.d	11.83432	0.69	0.323	0.024	0.34294	354	27
DZ-24b_3.d	13.45895	0.61	0.232	0.017	0.30741	363	21
DZ-24b_5.d	10.12146	0.51	0.448	0.029	0.31574	318	31
DZ-24b_6.d	7.032349	0.44	0.537	0.039	0.39201	350	56
DZ-24b_7.d	10.66098	0.59	0.379	0.024	0.42642	349	32
DZ-24b_9.d	10.74114	0.47	0.376	0.021	0.15686	348	23
DZ-24b_11.d	15.17451	0.52	0.1955	0.0079	0.21977	338	14
DZ-24b_12.d	10.04016	0.52	0.419	0.02	0.30365	337	26
DZ-24b_13.d	5.025126	0.51	0.602	0.048	-0.11024	387	85
DZ-24b_14.d	8.673027	0.48	0.461	0.029	0.42519	361	37

DZ-24b_15.d	3.257329	0.25	0.699	0.063	0.50227	420	160	
DZ-24b_16.d	7.874016	0.41	0.447	0.031	0.31322	406	44	
DZ-24b_17.d	7.824726	0.46	0.458	0.031	0.42683	401	47	
DZ-24b_18.d	9.578544	0.47	0.44	0.028	0.058561	340	29	
DZ-24b_19.d	13.69863	0.53	0.233	0.014	0.46983	356	18	
DZ-24b_20.d	9.910803	0.55	0.438	0.03	0.56342	330	34	
DZ-24b_21.d	11.83432	0.64	0.278	0.022	0.30117	375	26	
DZ-24b_22.d	14.28571	0.67	0.194	0.012	0.12773	362	20	
DZ-24b_24.d	13.71742	0.72	0.258	0.019	0.10242	341	21	
DZ-24b_28.d	6.6313	0.36	0.54	0.038	0.31005	365	58	
DZ-24b_31.d	8.496177	0.51	0.512	0.037	0.19863	308	39	
DZ-24b_32.d	6.666667	0.49	0.563	0.038	0.092342	332	55	
DZ-24b_33.d	6.369427	0.46	0.54	0.03	0.32808	387	50	
DZ-24b_35.d	9.861933	0.49	0.407	0.023	0.32995	358	28	
DZ-24b_38.d	8.93655	0.55	0.432	0.03	0.34328	375	39	
DZ-24b_42.d	8.257638	0.45	0.476	0.045	0.037338	358	51	
DZ-24b_43.d	9.680542	0.48	0.379	0.024	0.31319	386	29	
DZ-24b_45.d	5.91716	0.5	0.567	0.052	0.059136	410	63	
DZ-24b_46.d	6.134969	0.44	0.583	0.051	0.519	358	74	
DZ-24b_48.d	12.03369	0.55	0.321	0.028	0.46215	351	27	
DZ-24b_49.d	6.934813	0.44	0.529	0.035	0.31443	355	48	
DZ-24b_50.d	10.03009	0.57	0.403	0.022	0.22607	349	29	
DZ-24b_52.d	3.984064	0.31	0.71	0.055	0.4076	300	120	
DZ-24b_53.d	7.246377	0.62	0.543	0.042	0.31524	343	65	
DZ-24b_54.d	5.524862	0.39	0.61	0.053	0.26316	368	84	
DZ-24b_55.d	4.975124	0.39	0.657	0.055	0.42829	330	100	
DZ-24b_56.d	4.166667	0.29	0.654	0.055	0.4793	410	120	
DZ-24b_57.d	5.434783	0.42	0.572	0.046	0.31334	416	82	
DZ-24b_58.d	10.49318	0.54	0.361	0.018	0.2639	369	24	
DZ-24b_60.d	7.54717	0.4	0.52	0.025	0.14665	347	34	
DZ-24b_61.d	8.230453	0.61	0.487	0.03	0.31935	349	44	
DZ-24b_62.d	10.85776	0.62	0.355	0.024	0.21503	356	27	
Grain	Final 238/206	$2\sigma$	Final 207/206	$2\sigma$	Error Correlation 238/206 vs 207/206	Final 207 Age	$2\sigma$	
DZ-25_2.d	6.451613	0.79	0.475	0.037	-0.4571	387	47	
DZ-25_4.d	14.14427	0.73	0.191	0.016	0.22822	365	23	
DZ-25_9.d	9.633911	0.65	0.339	0.023	-0.52425	385	29	
DZ-25_10.d	4.694836	0.3	0.615	0.03	0.46917	345	63	
DZ-25_11.d	4.405286	0.35	0.607	0.034	0.010462	392	72	
DZ-25_13.d	7.434944	0.47	0.48	0.022	0.068312	357	36	
DZ-25_15.d	5.913661	0.39	0.567	0.033	0.4372	361	57	
DZ-25_16.d	7.751938	0.59	0.456	0.074	-0.097641	424	47	
DZ-25_18.d	4.62963	0.29	0.644	0.028	0.34018	317	57	
DZ-25_19.d	6.756757	0.68	0.486	0.037	-0.41029	374	47	
DZ-25_22.d	13.55014	0.73	0.1783	0.0083	0.3294	387	22	
DZ-25_23.d	9.191176	0.5	0.388	0.022	0.27521	381	33	

DZ-25_24.d	9.871668	0.61	0.382	0.019	0.24001	363	26
DZ-25_26.d	11.58749	0.51	0.272	0.013	0.072059	386	21
DZ-25_27.d	8.779631	0.45	0.414	0.016	-0.034945	373	23
DZ-25_30.d	6.802721	0.55	0.527	0.024	-0.19209	337	36
DZ-25_31.d	10.14199	0.65	0.331	0.026	0.482	402	41
DZ-25_37.d	7.880221	0.48	0.452	0.024	0.25576	386	36
DZ-25_40.d	4.329004	0.38	0.595	0.028	-0.050613	412	59
DZ-25_43.d	11.89061	0.92	0.245	0.028	-0.65916	373	18
DZ-25_45.d	12.57862	0.5	0.222	0.012	0.3484	388	17
DZ-25_47.d	11.97605	0.68	0.229	0.023	-0.17953	393	26